CANADIAN THESES ON MICROFICHE

I.S.B.N.

THESES CANADIENNES SUR MICROFICHE

National Library of Canada
Collections Development Branch

Canadian Theses on
Microfiche Service

Ottawa, Canada
K1A 0N4

Bibliothèque nationale du Canada
Direction du développement des collections

Service des thèses canadiennes
sur microfiche

NOTICE

The quality of this microfiche is heavily dependent upon the quality of the original thesis submitted for microfilming. Every effort has been made to ensure the highest quality of reproduction possible.

If pages are missing, contact the university which granted the degree.

Some pages may have indistinct print especially if the original pages were typed with a poor typewriter ribbon or if the university sent us a poor photocopy.

Previously copyrighted materials (journal articles, published tests, etc.) are not filmed.

Reproduction in full or in part of this film is governed by the Canadian Copyright Act, R.S.C. 1970, c. C-30. Please read the authorization forms which accompany this thesis.

AVIS

La qualité de cette microfiche dépend grandement de la qualité de la thèse soumise au microfilmage. Nous avons tout fait pour assurer une qualité supérieure de reproduction.

S'il manque des pages, veuillez communiquer avec l'université qui a conféré le grade.

La qualité d'impression de certaines pages peut laisser à désirer, surtout si les pages originales ont été dactylographiées à l'aide d'un ruban usé ou si l'université nous a fait parvenir une photocopie de mauvaise qualité.

Les documents qui font déjà l'objet d'un droit d'auteur (articles de revue, examens publiés, etc.) ne sont pas microfilmés.

La reproduction, même partielle, de ce microfilm est soumise à la Loi canadienne sur le droit d'auteur, SRC 1970, c. C-30. Veuillez prendre connaissance des formules d'autorisation qui accompagnent cette thèse.

THIS DISSERTATION
HAS BEEN MICROFILMED
EXACTLY AS RECEIVED

LA THÈSE A ÉTÉ
MICROFILMÉE TELLE QUE
NOUS L'AVONS REÇUE

NL-339 (r. 82/08)

Canada

FLUID FLOW DURING ARGON-STIRRING IN LADLES
AND
HEAT TRANSFER DURING SOLIDIFICATION IN MOLDS

by

Low, Choon-Hong, Stephen

A thesis
presented to the University of Ottawa,
School of Graduate Studies and Research
in partial fulfillment of the
requirements for the degree of
Master of Applied Science
in
Department of Mechanical Engineering

OTTAWA, Ontario, 1982

ACKNOWLEDGEMENTS

The author wishes to express his gratitude to his supervisor, Dr. Martha Salcudean, for her dedicated interest and guidance in the preparation of this thesis. Her constant encouragements and invaluable suggestions are very much appreciated.

Indebtedness is also due to Mr. Al Hurda, Dr. M. Mahfuz and Mr. Ray Wong for fruitful discussions and assistance in computer programming.

The financial support received from the Natural Sciences and Engineering Research Council, the Department of Energy, Mines and Resources, the Ontario Graduate Scholarship and the University of Ottawa are gratefully acknowledged.

Last but not least, the author also wishes to thank his family and friends for their moral support and encouragement.

ABSTRACT

An attempt is made in the present investigation to simulate two processes in the steelmaking operations, namely, the fluid flow during argon-stirring in a ladle and heat transfer during solidification in a mold. Two different mathematical approaches simulating each of the processes are constructed.

A three-dimensional, transient model is developed with the goal of modelling gas-driven flows involving asymmetric injection. A numerical procedure based on the Los Alamos MAC [2], finite difference technique is developed to solve the governing equations for the mass, momentum and energy conservation. Both axisymmetric gas injection and off-centered jet are considered and the resulting computed flow patterns are presented. The obtained results from the model are in good agreement with existing computations. The temperature field in an initially, stagnant, thermally stratified liquid resulting from the local introduction of a gas jet on the bottom surface is also illustrated.

The solidification process involving temperature change with heat flow as a function of time, release of latent heat of fusion during freezing, and varying conditions at the boundaries is described in terms of partial differential equations. The alternating direction implicit (ADI) method

is applied to the solution of the partial differential equations written in finite difference form describing the heat transfer and solidification in the cast and mold. Testings of the model are carried out for both two-dimensional, rectangular and three-dimensional, cylindrical ingots. Results of the computed temperature distributions and profiles in the ingot and mold, the solidification front profiles and solidification time are presented. The nature and trend of the computed results have been found to agree satisfactorily with existing works.

TABLE OF CONTENTS

	Page
ACKNOWLEDGEMENTS	ii
ABSTRACT	iii
TABLE OF CONTENTS	v
LIST OF TABLES	viii
LIST OF FIGURES	ix
NOMENCLATURE	xiii

Chapter		Page
I.	INTRODUCTION	1
	1.1 Mathematical Modelling and Its Practical Importance in Metallurgy	1
	1.1.1 Ladle Metallurgy	2
	1.1.2 Solidification of Castings	4
	1.2 Outline and Objective of Present Investigations	6
II.	LITERATURE SURVEY	8
	2.1 Previous Work on Fluid Flow Modelling and Ladle Metallurgy	8
	2.2 Previous Work on Solidification Modelling	12
III.	INVESTIGATION OF FLUID FLOW AND HEAT TRANSFER DURING ARGON-STIRRING IN LADLES	15
	3.1 Physical Model	15
	3.2 Mathematical Formulation	16
	3.2.1 Governing Differential Equations	17
	3.2.2 General Boundary Conditions	20
	3.2.3 Thermal Boundary and Initial Conditions	21
	3.2.4 Calculating the Effective Viscosity	22
	3.2.5 Calculating the Void Fraction and Density	24

3.3 Numerical Procedure Using Finite Difference Method 26
3.3.1 Grid Network 26
3.3.2 Derivation of Finite Difference Equations 27
3.3.2.1 Continuity Equation 27
3.3.2.2 Momentum Equations 29
3.3.2.3 Energy Equation 37
3.3.3 Application of Boundary Conditions . 39
3.3.4 Computational Procedure 42
3.3.5 Stability and Accuracy Considerations 48
3.4 Results and Discussions 50

IV. INVESTIGATION OF HEAT TRANSFER DURING SOLIDIFICATION IN MOLDS 57

4.1 Physical Model 57
4.2 Mathematical Formulation 58
4.2.1 General Equation of Heat Flow 58
4.2.2 Initial and Boundary Conditions 59
4.2.3 Thermal Properties 64
4.2.4 Latent Heat of Fusion 67
4.3 Numerical Procedure for Solving Heat Flow Equation 69
4.3.1 Grid Design 69
4.3.2 Finite Difference Approximation Using the Energy Balance Method 69
4.3.2.1 Finite Difference Equation for an Internal Node 70
4.3.2.2 Finite Difference Equation for a Side Boundary Node ... 74
4.3.2.3 Finite Difference Equation for an Interface Node 75
4.3.2.4 Finite Difference Equations for Other Nodes 77
4.3.3 Outline of the Alternating Direction Implicit (ADI) Method 77
4.3.4 Summary of the Computer Program 85
4.4 Results and Discussions 86
4.4.1 Application to a Two-Dimensional, Rectangular Solidification Problem . 87
4.4.2 Application to Solidification Problem in Three-Dimensional, Cylindrical System 93

V. CONCLUSION 98

5.1 Summary of Present Investigations 98
5.1.1 Ladle Processing Simulation 98
5.1.2 Solidification Simulation 100
5.2 Concluding Remarks 102

Appendix

A. FINITE DIFFERENCE EXPRESSIONS FOR THE CONVECTIVE AND VISCOUS TERMS IN EQUATIONS (3.20) AND (3.21) 104

B. FINITE DIFFERENCE EQUATIONS FOR NODES USED IN THE SOLIDIFICATION CALCULATIONS 111

BIBLIOGRAPHY 179

LIST OF TABLES

Table		Page
3.1	Parameters used in 2-D computations	51
4.1	Input data for solidification program	89

LIST OF FIGURES

Figure		Page
3.1	Schematic diagram of (a) Central and (b) Off-centered jet	124
3.2	Finite difference grid used in computations	125
3.3	A computational element	126
3.4	Flow chart for multidimensional modelling .	127
3.5	Velocity fields for (a) two-dimensional computations of present code, (b) Deb Roy et al.'s model [29], (c) Szekely et al.'s experimental results [23]	128
3.6	Comparison between Guthrie et al.'s [69] prediction and results from present model .	129
3.7	Computed velocity field for a cylindrical jet with slip	130
3.8	Computed velocity field for a cylindrical jet with zero slip	131
3.9	Computed velocity fields for (a) Cylindrical jet with zero slip, (b) Conical jet with zero slip	132
3.10	Comparison of predicted axial velocity distribution between a cylindrical and a conical jet at different values of z/H	133
3.11	Predicted velocity fields for different values of r_c/R at time = 10.0 sec. after jetting	134
3.12	Predicted velocity fields for different values of r_c/R at time = 40.0 sec. after jetting	135
3.13	Quantitative comparison of the predicted axial velocity distribution at different values of z/H	136

3.14	Vertical and horizontal views of the velocity fields for a jet entering the vessel at 3/4-distance between the center and the wall	137
3.15	Vertical and horizontal views of the velocity fields for a jet entering the vessel near the side wall	138
3.16	Predicted velocity field for off-centered jet by Wong [69]	139
3.17	Non-dimensional temperature distribution at time = 5.0 sec. after jetting	140
3.18	Non-dimensional temperature distribution at time = 12.5 sec. after jetting	141
4.1	Correlations for the thermal conductivity of Low-Carbon Steel [48]	142
4.2	Functional relationships for thermal conductivity of molding sand [48]	143
4.3	Selected data and functional relationships for specific heat of Low Carbon Steel, including the latent heat approximation [48]	144
4.4	Arrangement of grid points	145
4.5	Typical internal node for the two-dimensional situation	146
4.6	Control volume of an internal node in cylindrical coordinates	147
4.7	Control volume for a typical side boundary node	148
4.8	Control volume for an interface node (a) before and (b) after the air-gap formation	149
4.9	Node numbers indicating the type of nodes in the grid arrangement	150
4.10	Illustration of line-by-line iteration used in the ADI scheme	151

4.11	Flow chart for solidification modelling ...	152
4.12	Finite difference grid and boundary conditions	153
4.13	Temperature distribution at time = 20 min..	154
4.14	Advancement of solidification front in a rectangular ingot	155
4.15	Progress of liquidus and solidus isotherms with the square root of time for a rectangular ingot	156
4.16	Isotherms in the rectangular ingot at (a) time = 10.0 min. and (b) time = 40.0 min. after pouring	157
4.17	Isotherms in the rectangular mold at (a) time = 10.0 min. and (b) time = 40.0 min. after pouring	158
4.18	Advancement of solidification front in a cylindrical ingot	159
4.19	Progress of liquidus and solidus isotherms with the square root of time for a cylindrical ingot	160
4.20	Isotherms in the cylindrical ingot at (a) time = 10.0 min. and (b) time = 40.0 min. after pouring	161
4.21	Isotherms in the cylindrical mold at (a) time = 10.0 min. and (b) time = 40.0 min. after pouring	162
4.22	Temperature gradients in the ingot and mold at time = 10.0 min. after pouring	163
4.23	Temperature gradients in the ingot and mold at time = 40.0 min. after pouring	164
4.24	Cooling curves at the center of ingot	165
4.25	Ingot and mold temperature-time variation at 66.7 cm from top of ingot	166
4.26	Variation of effective heat transfer coefficient at side outer surface of mold	167

4.27	Variation of effective heat transfer coefficient at bottom outer surface of mold	168
4.28	Variation of the interface heat transfer coefficient	169
B.1	Control volume for a node located at the bottom of the mold	170
B.2	Control volume for a corner node located at the bottom of the mold	170
B.3	Control volume for a node located at the top boundary	171
B.4	Control volume for a corner node located at the top of the mold	171
B.5	Control volume for a centreline node	172
B.6	Control volume for a centreline node located at the cast/mold interface	172
B.7	Control volume for a centreline node located at the top boundary	173
B.8	Control volume for a centreline node located at the bottom boundary	173
B.9	Control volume for an interface node located at the bottom of the casting	174
B.10	Control volume for a corner node located at the interface (a) before and (b) after gap formation	175
B.11	Control volume for an interface node located at the top boundary (a) before and (b) after gap formation	176
B.12	Control volume for a node on the outer surface of the cast after the air-gap is formed	177
B.13	Control volume for an interface node located at the corner of the cast (after the air-gap is formed)	177
B.14	Control volume for a node on the outer surface of the cast located at the top boundary (after the air-gap is formed)	178

NOMENCLATURE

Symbols	Definition
A	Area
a_n, b_n, c_n, d_n	Coefficients in the tridiagonal system
C, C_p	Specific heat
D	Diameter of vessel
$D_{i,j,k}$	Discrepancy, term
DT	Equivalent temperature defined by equation (4.13)
E	Emissivity
F	Geometric factor
f	Interpolation factor (equation 4.16)
Gr	Grashof number
g	Gravitational acceleration
H	Height of vessel
H_f	Latent heat of fusion
h	Heat transfer coefficient
h_b, h_g, h_s, h_t	Effective heat transfer coefficients at bottom, gap, side and top surface, respectively
i,j,k	Coordinates in the radial, tangential and axial direction respectively
IMAX,JMAX,KMAX	Number of grid mesh in the radial, tangential and axial direction respectively
K	Thermal conductivity
m_j	Mass flow rate of gas at nozzle

n	Coordinate in the normal direction
P	Pressure
Q	Volumetric flow rate
Q_{gen}	Internal energy generated per unit volume per unit time
R	Radius of vessel
Re	Reynolds number
r, ϕ, z	Cylindrical coordinates
r_c	Radius of gas-liquid core
$S_{i,j,k}$	Scalar quantity
T	Temperature
T_L	Liquidus temperature
T_S	Solidus temperature
T_{co}, T_{mo}	Initial metal and mold temperature respectively
u	Radial velocity
v	Tangential velocity
w	Axial velocity
w_{slip}	Slip velocity
x,y,z	Cartesian coordinates

Greek Symbols	Definition
α	Thermal diffusivity $(= \frac{K}{\rho C_p})$
$\bar{\alpha}$	Void fraction
β	Variable defined by equation (3.70)
Δ, δ	Increment

∂	Partial derivative
ϵ	Convergence criteria
ζ	Upwind differencing coefficient
θ	Non-dimensional temperature $(= \frac{T-T_b}{T_t-T_b})$
μ	Dynamic viscosity
ν	Kinematic viscosity
ξ	Variable used to change the finite difference equations from cylindrical to Cartesian system
ρ	Density
σ	Stefan-Boltzmann constant
Ω	Relaxation factor

Subscripts	Definition
a	Ambient
b	Bottom
c	Cast
eff	Effective value
g	Gas
i,j,k	Grid points
int	Interface
j	Value at jet entrance
l	Liquid
m	Mold
t	Top
w	Wall

Superscripts	Definition
-	Average value
n	Values evaluated at nth time-step
$n+\frac{1}{2}$	Values evaluated at $t = t + \Delta t/2$
n+1/3	Values evaluated at $t = t + \Delta t/3$
n+2/3	Values evaluated at $t = t + 2\Delta t/3$
n+1	Values evaluated at (n+1)th time-step i.e. $t = t + \Delta t$

CHAPTER 1

INTRODUCTION

1.1 MATHEMATICAL MODELLING AND ITS PRACTICAL IMPORTANCE IN METALLURGY

The development of the high-speed, large-memory electronic computers has greatly enhanced the use of mathematical models and numerical techniques to simulate many complex fluid flow and heat transfer problems. Furthermore, with our modern and fast-expanding technology, there has been a marked increase in the demand for high quality steel and steel products. It is thus inevitable that certain sectors of the steelmaking industries are seeking to develop new technologies and new processes to improve the present steelmaking operations.

In the steelmaking practice, after the furnace operations have been completed, the molten metal leaving the furnace is tapped into a container called a ladle. The function of the ladle is to serve as a reservoir for the molten steel where it is allowed to settle down and cool to the proper processing temperature. While in the ladle, often, ladle processing is carried out to control the chemical composition. From the ladle, it is poured into molds that have the size and shape of the casts desired, to

solidify. The present work is centered around the ladle and casting processes in the steelmaking operations.

1.1.1 Ladle Metallurgy

The development of ladle metallurgy where argon-gas is injected into the ladle to improve the cast steel quality has attracted many researchers in recent years.

The injection of a gas jet or bubbles rising through the liquid entrains the surrounding fluid and causes flow recirculations in the reactor. This effect has been widely used for many refining processes. Examples include the use of oxygen jets in top- and bottom-blown steelmaking processes, argon-stirring in ladles for steel cleanliness and temperature control, and side-blow jets in copper and nickel converting.

One of the most effective means of improving steel quality is injection of the liquid metal with argon in the ladle [1]. Injection of liquid steel with argon reduces the non-metallic (phosphorus and sulphur) and gas (hydrogen and oxygen) contents in the steel and improves the uniformity of their distribution in the steel. This can result in substantial improvement in the quality of its casting and mechanical properties.

In some cases, where molten steel is left in the ladle, temperature stratification may have occurred over a long

holding period (example, 20 minutes). Gas stirring of the molten bath is used to achieve homogeneous temperature distribution.

In order to control the process and to reach the desired metallurgical results, it is necessary to know the principal characteristics of the fluid dynamics in the ladle during gas agitation. One factor of key importance is the flow pattern induced in the processing vessels. The flow pattern influences various heat and mass transfer phenomena and regulates process kinetics. The kinetics of these processes are usually complex. Moreover, the need for a better quantitative understanding of the fluid flow and heat transfer phenomena in these processes has prompted a number of hydrodynamic studies.

One of the difficulties encountered in a hydrodynamic approach is that liquid steel, being opaque and at high temperature (1600-1700°C), makes direct measurements of the flow almost impossible. Experimental modelling of these processes are often expensive and time-consuming and it is difficult to achieve all the conditions of a real metallurgical process in a laboratory model.

The last decade has seen a great increase in the use of computers to aid in the simulation of engineering problems. One of the most rapidly advancing fields is the use of numerical methods for approximating the solutions to mathematical formulation of problems that are too complex

to be solved analytically. Recent developments in numerical techniques for solving fluid flow equations have made it possible to theoretically investigate the flow characteristics reasonably well. The predictions based on these models have been found to be in reasonable agreement with measurements obtained both in laboratory models and in industrial installations.

1.1.2 Solidification of Castings

The solidification process that takes place in a mold involves many complex phenomena. Temperature changes with heat flow as a function of time, internal heat is generated during the phase change, and varying conditions are found at the boundaries. In order to understand the importance of monitoring the solidification process, one has to understand the mechanism of the freezing of metal.

Molten steel is practically a uniform liquid. The various elements in addition to iron, such as carbon, manganese, silicon, phosphorus, sulphur, chromium, nickel and vanadium, are all in solution in the iron. However, like all other metals, steel crystallizes during freezing and in doing so solidifies selectively. Solidification begins with the formation of crystals rich in the element which has the freezing point above that of the alloy. The liquid left between the crystals is rich in elements that have a

low melting point. If cooling is fast, they are quickly trapped between the original crystals and dendrites are formed. The dendrites are not harmful since they are well distributed and can be broken up readily in hot working. However, if cooling is quite slow, the low-melting elements remain liquid for a sufficiently long time to allow them to gather in certain parts of the casting, particularly the axis, causing segregation. The extent and location of such segregations and hence their influence on the quality of the casting depends on the rate of solidification which in turn depends on the size of the cast, pouring temperature, rate of pouring and the design of the mold. Therefore, the control of the whole solidification process is very important.

The process of solidification can be described in terms of partial differential equations. These equations with the appropriate boundary conditions representing the actual foundry operations can be solved by using numerical techniques. While numerical calculation schemes probably never substitute entirely the experimental investigations, they have already been proven useful for exploring and helping to optimize fairly complicated heat transfer systems in which measurements are difficult, costly, and laborious to obtain.

1.2 OUTLINE AND OBJECTIVE OF PRESENT INVESTIGATIONS

In essence, the present work includes predicting the flow fields and heat transfer associated with asymmetric recirculatory flows in systems of cylindrical geometry, and predicting the heat transfer phenomenon associated with the solidification process in a mold. Numerical solutions were obtained by solving the governing partial differential equations for specific boundary conditions, using finite difference approximations. Two different methods of approach to the numerical solutions were used for the two processes.

The approach to the first process was based on a variant of the Los Alamos Marker-and-Cell (MAC) method [2] and utilized the explicit finite difference method to solve numerically the unsteady, multidimensional fluid flow in a cavity induced by a gaseous jet. An asymptotic time solution of the unsteady flow equations was used to obtain the steady-state solution of the flow. Cases considered include axisymmetric gas injection wherein the gas-liquid plume was either of constant radius, or expanded in a cone-like manner towards the surface. Off-centered gas flows were also considered and the resulting three-dimensional flow patterns computed. Temperature fields resulting from the local introduction of gas on the bottom surface were also illustrated. The mathematical formulation of the finite difference equations, the numerical procedure, and some sample results are presented in Chapter III.

For the solidification problem, the general equation of heat flow was solved based on the Alternating Direction Implicit (ADI) method developed by Peaceman and Rachford [3]. The formation of air-gap, liberation of latent heat of fusion and other specific problems associated with this phenomena are discussed with the mathematical formulations and solutions in Chapter IV. Testings of the model were carried out for two- and three-dimensional situations and temperature distributions and solidification time were computed.

The investigations were done with the objective of providing a better understanding of the various phenomena taking place, and also to provide a model which could be used for testing and obtaining useful information which may be difficult or costly to obtain in the actual operations. This information could be used as operational guidelines to improve the control of these processes and also as the basis for the design of more effective systems.

CHAPTER II

LITERATURE SURVEY

2.1 PREVIOUS WORK ON FLUID FLOW MODELLING AND LADLE METALLURGY

The history of computational fluid dynamics goes all the way back to 1910 when L.F. Richardson presented his work to the Royal Society which was considered as the cornerstone of modern numerical analysis of partial differential equations [4]. The development of electronic computers gave motivation to further development of numerical simulations. Considerable pioneering work in computational fluid dynamics was done at the Los Alamos Scientific Laboratory [2,5-11]. The Marker-and-Cell (MAC) technique which was originally developed for solving viscous, incompressible and two-dimensional transient fluid flow problems, was adopted as basis for the present model. Fluid motions were calculated by solving the Navier-Stokes' equations written in finite difference form with pressure and velocity as the primary dependent variables. This work has led to the publishing of several general codes such as SMAC [6], SOLA-SURF [11] and other works [12-18].

At the same time, the Imperial College group at London has also developed some models for calculating recirculatory [19] and boundary layer flows [20]. Beside many other

recent developments, a number of investigations have been carried out, involving hydrodynamic studies and analyses of secondary refining operations in steelmaking processes. A number of the works in ladle metallurgy have been presented in recent symposia and papers [21,22].

Early experimental studies have mainly been based on aqueous physical models. Szekely, Wang and Kiser [23] attempted a two-dimensional aqueous modelling of an argon-stirred ladle. In their mathematical treatment, the gas jet region or core was modelled as a solid wall moving upwards at constant velocity. Flow fields were predicted using the Spalding's k-w two equations model of turbulence and compared with experimental velocity fields measured using hot film anemometry. Qualitative agreement was found between both results.

Szekely, Dilawari and Metz [24] modelled the effect of the two-phase gas jet region by using a mechanical belt drive system to generate the turbulent recirculatory flow. The agreement between the theoretical predictions and experimental measurements was reasonably good.

More recently, Szekely, Lehner and Chang [25] again employed a vertical moving core assumption to predict flow patterns and eddy diffusivity values using the k-w model of turbulence. Pilot scale measurements were obtained for a 7-tons vessel and plant scale measurements were taken using

40-tons and 60-tons argon-stirred ladles. Experimental measurements describing the dispersion of added tracers were reasonably well predicted by the mathematical model.

El-Kaddah and Szekely [26] developed a mathematical model to represent the desulphurization of steel in ladle metallurgy operations. The velocity field was calculated for 6-tons and 40-tons ladles using Jones and Launder's $k-\varepsilon$ two-equations model [27]. The actual desulphurization kinetics were represented in terms of sulphur transfer in a turbulent recirculating melt. Predictions based on the model were found to agree reasonably well with measurements carried out for both the 6-tons and 40-tons ladles.

Hsiao, Lehner and Bjorn [28] also carried out experimental studies for a 60-tons ladle stirred by argon. Direct measurements of the velocities in the plume and surface layer were carried out in the 60-tons liquid-steel ladle after preliminary measurements were done in a water model and a 6-tons pilot ladle.

A mathematical model, based on a buoyancy driven flow was presented by Deb Roy, Majumdar and Spalding [29,30] and more recently by Szekely, El-Kaddah and Grevet [31]. In both models, the inlet gas mass flow rates were used to estimate the plume, which both modelled as a vertical cylinder. Average plume voids were estimated for both slip and non-slip conditions. For the slip condition, the gas was

assumed to move with a larger velocity than the liquid. The calculations were carried out using Patankar and Spalding's numerical methods. A constant viscosity suggested by Pun and Spalding [32] for confined jets was used in both works. Flow predictions were compared with experimental measurements carried out on a water model of an argon-stirred ladle.

More recently, Sahai and Guthrie [33] have presented an alternative effective viscosity model for submerged gas bubble columns since these, rather than jets, are more typical of ladle metallurgy operations.

So far, the mathematical models dealt mainly with two-dimensional situations, namely the axisymmetrical cylindrical systems. Nonetheless, the majority of the systems are not axisymmetrical. In practice, many operations of industrial interest and application involve three-dimensional flows, wherein the gas source is off-centered with respect to the ladle center. The extension of modelling to the three-dimensional systems would be worthwhile. Similarly, while attendant thermal phenomena also need to be modelled, no work of this nature is available in the literature. None of the models deals with the transient aspect of the process which is important for analyzing the temperature distribution and the chemical kinetics associated with the change in the temperature gradient during the processing.

Thus, the present work to model three-dimensional transient flows and heat transfer in a gas-stirred vessel would be useful in gaining some insight into the details of the process.

2.2 PREVIOUS WORK ON SOLIDIFICATION MODELLING

The last few decades have seen many theoretical analyses using mathematical models to complement experimental investigations of the solidification phenomena.

Analytical solutions have been developed for various heat flow problems. Analytical solutions, however, are highly restrictive and often over-simplified. As such, the results obtained are only indicative. Some of the earlier works were by Lightfoot [34,35] and Adams [36]. More recent studies were done by Garcia and Prates [37,38] to predict the solidification rate and the temperature distribution during the unidirectional solidification of metals in cooled and uncooled molds.

Paschkis [39-41] simulated the solidification process by using analog computers. His early works contributed much to many improvements in the design concepts for castings. The analog computer, however, is limited to simple problems. Numerical techniques using the digital computer permit more realistic simulation of the actual problem without too much simplifications.

In earlier works, Sarjant and Slack [42] and Dusinberre [43] used a technique developed for the numerical integration of the heat flow equations in two dimensions. The main advantage of the Sarjant and Slack method is that, by using an enthalpy term, the latent heat of fusion is taken into account in the calculations. However, the method required very small time-steps to satisfy the stability criterion. Nishida et al [44], Srinivasion [45] and Lazaridis et al [46] used the explicit finite difference scheme for predicting one-dimensional solidification problems with constant thermal properties. The Crank-Nicolson finite difference method was used by Thamban and Panchanathan [47] for simulating unidirectional solidification of aluminum alloys in cast iron molds. The thermal properties of pure aluminum castings were assumed to vary with temperature and the formation of an air-gap was considered.

Marrone, Wilkes and Pehlke [48,49] investigated the solidification of low-carbon steel castings in simple "T" and "L" shaped sand molds. The Saul'yev explicit finite difference algorithm and the alternating direction implicit method were used to solve the heat flow equations. In addition, a technique has been developed for determining material thermal properties. This work was continued by Pehlke et al [50] which involved the comparison of a computer simulation with results of a thermally monitored casting.

Raychandhuri et al [51] simulated two-dimensional solidification by modelling the solidification process in three stages. The different phases of solidification (superheated molten metal in the mold, initial solidification, and air-gap formation) were described with additional boundary conditions to satisfy the conditions at each stage. A number of other studies of solidification using finite difference approximation have also been published [52-58].

While finite difference methods have been the more popular method for numerical modelling of solidification problems, a number of models have been developed using the finite element method [59-63].

The list of references does not exhaust the topics of mathematical modelling of heat flow and solidification. Unfortunately, most of the published works dealt with one- or two-dimensional problems. Furthermore, the lack of reliable information on thermal properties required the use of many simplifying assumptions. The present interest is therefore to develop a model capable of handling three-dimensional situations and the varying properties and conditions encountered in the solidification process.

CHAPTER III

INVESTIGATION OF FLUID FLOW AND HEAT TRANSFER DURING ARGON-STIRRING IN LADLES

3.1 PHYSICAL MODEL

The present chapter describes the prediction of the flow fields and heat transfer phenomena associated with asymmetric recirculatory flows in systems of cylindrical geometry. Numerical solution is obtained by solving a set of partial differential equations governing the transport of mass, momentum and energy. A model was developed using the finite difference technique. The physical process involves the injection of gas into an initially stagnant liquid bath. The rising plume can be considered as being buoyancy driven and resulting from a lower density gas/liquid mixture above the gas injection point in the container. The rising plume entrains the surrounding fluid and causes recirculation in the other parts of the container.

Figure 3.1 shows the schematic diagram of the gas-stirred vessel for a central and off-centered jet. Cases considered include axisymmetric gas injection wherein the gas-liquid mixture is modelled as a plume of constant radius, or one that expands in a cone-like manner towards the surface. For the purposes of numerical solutions to the set of governing differential equations, two cases for

the gas-liquid core were considered:

i) Following the assumption of Deb Roy et al's two dimensional analysis [29], the gas-liquid mixture was modelled as a cylindrical jet of constant core radius, r_c.

ii) In reality, the upwelling gas-liquid mixture is more likely to expand in a conical fashion from an entry region in the bottom. The core radius was, therefore, taken to be a function of its vertical distance, i.e. $r_c = r_c(z)$.

Non-central gas flows are also considered and the resulting three-dimensional flow patterns computed. Temperature fields resulting from the local introduction of gas on the bottom surface is illustrated. Predicted results are compared with existing computations and experimental works.

3.2 MATHEMATICAL FORMULATION

The mathematical formulation of any flow problem is a statement of the governing transport equations describing the physics of the phenomena. The statement is essentially of the same form for all flow problems. The distinguishing features of any problem are the assumptions and boundary conditions. For any particular problem, the assumptions and boundary conditions must be defined. Once this has been

done, the scope of the equations is limited to that particular problem. The differential equations presented in the following sections are developed to deal with recirculating flows in a cylindrical vessel. The recirculatory flows were induced by a gas jet entering the vessel.

3.2.1 Governing Differential Equations

The set of governing equations for the conservation of mass, momentum and energy are written in three-dimensional cylindrical coordinates for unsteady state. The differential equations are written in the form from which the finite difference equations can readily be derived. Defining r, ϕ, and z as the coordinates in the radial, tangential, and axial directions respectively and u, v, w as their respective velocities, the differential equations are written as:

Continuity equation

$$\frac{\partial \rho}{\partial t} + \frac{\partial \rho u}{\partial r} + \frac{1}{r}\frac{\partial \rho v}{\partial \phi} + \frac{\partial \rho w}{\partial z} + \frac{\rho u}{r} = 0 \qquad (3.1)$$

$$\frac{\partial u}{\partial r} + \frac{1}{r}\frac{\partial v}{\partial \phi} + \frac{\partial w}{\partial z} + \frac{u}{r} = 0 \qquad (3.2)$$

Equation (3.1) is written for the flow of a heterogeneous, compressible fluid where the local density changes are related to the fluid transport. Equation (3.2) expresses the volume conservation, which is identical to conservation

of mass for a homogeneous, incompressible fluid.

Momentum equation

$$\frac{\partial \rho u}{\partial t} + \frac{\partial \rho u^2}{\partial r} + \frac{1}{r}\frac{\partial \rho uv}{\partial \phi} + \frac{\partial \rho uw}{\partial z} + \frac{\rho u^2}{r} - \frac{\rho v^2}{r}$$

$$= -\frac{\partial P}{\partial r} + g_r \rho + \mu_{eff}\left[\frac{\partial^2 u}{\partial r^2} + \frac{1}{r^2}\frac{\partial^2 u}{\partial \phi^2} + \frac{\partial^2 u}{\partial z^2} + \frac{1}{r}\frac{\partial u}{\partial r}\right.$$

$$\left. - \frac{2}{r^2}\frac{\partial v}{\partial \phi} - \frac{u}{r^2}\right] \qquad (3.3)$$

$$\frac{\partial \rho v}{\partial t} + \frac{\partial \rho uv}{\partial r} + \frac{1}{r}\frac{\partial \rho v^2}{\partial \phi} + \frac{\partial \rho vw}{\partial z} + \frac{2\rho uv}{r}$$

$$= -\frac{1}{r}\frac{\partial P}{\partial \phi} + g_\phi \rho + \mu_{eff}\left[\frac{\partial^2 v}{\partial r^2} + \frac{1}{r^2}\frac{\partial^2 v}{\partial \phi^2} + \frac{\partial^2 v}{\partial z^2}\right.$$

$$\left. + \frac{1}{r}\frac{\partial v}{\partial r} + \frac{2}{r^2}\frac{\partial u}{\partial \phi} - \frac{v}{r^2}\right] \qquad (3.4)$$

$$\frac{\partial \rho w}{\partial t} + \frac{\partial \rho uw}{\partial r} + \frac{1}{r}\frac{\partial \rho vw}{\partial \phi} + \frac{\partial \rho w^2}{\partial z} + \frac{\rho uw}{r}$$

$$= -\frac{\partial p}{\partial z} + g_z \rho + \mu_{eff}\left[\frac{\partial^2 w}{\partial r^2} + \frac{1}{r^2}\frac{\partial^2 w}{\partial \phi^2} + \frac{\partial^2 w}{\partial z^2} + \frac{1}{r}\frac{\partial w}{\partial r}\right] \qquad (3.5)$$

The form of the momentum equations used takes into account the changes in momentum that result from density variations. The first term on the left-hand side expresses the rate of accumulation of momentum per unit volume. All the remaining terms on the left-hand side describe the

convection of momentum by fluid motion. The first term on the right-hand side expresses the momentum change arising from the pressure forces, whereas the second term describes the momentum production by body forces. The remaining terms within the bracket represent the diffusion of momentum by viscous processes where μ_{eff} is the effective viscosity.

Energy equation

$$\frac{\partial \rho T}{\partial t} + \frac{\partial \rho u T}{\partial r} + \frac{1}{r}\frac{\partial \rho v T}{\partial \phi} + \frac{\partial \rho w T}{\partial z} + \frac{\rho u T}{r}$$

$$= \frac{K}{C_p}\left(\frac{\partial^2 T}{\partial r^2} + \frac{1}{r^2}\frac{\partial^2 T}{\partial \phi^2} + \frac{\partial^2 T}{\partial z^2} + \frac{1}{r}\frac{\partial T}{\partial r}\right)$$

$$+ 2\mu_{eff}\left\{\left(\frac{\partial u}{\partial r}\right)^2 + \left[\frac{1}{r}\left(\frac{\partial v}{\partial \phi} + u\right)\right]^2 + \left(\frac{\partial w}{\partial z}\right)^2\right\}$$

$$+ \mu_{eff}\left\{\left(\frac{\partial v}{\partial z} + \frac{1}{r}\frac{\partial w}{\partial \phi}\right)^2 + \left(\frac{\partial w}{\partial r} + \frac{\partial u}{\partial z}\right)^2\right.$$

$$\left. + \left[\frac{1}{r}\frac{\partial u}{\partial \phi} + r\frac{\partial}{\partial r}\left(\frac{v}{r}\right)\right]^2\right\} \qquad (3.6)$$

For those situations in which fluid flow is accompanied by heat transfer, the energy equation is used in addition to the equations of continuity and motion. Equation (3.6) is the energy equation written in terms of the fluid temperature, T. The thermal conductivity, K, is considered to be constant and C_p is the heat capacity of the fluid at

constant pressure. The viscous dissipation terms in the equation are omitted in the calculation as being negligible for incompressible flow. The final form of the energy equation used calculates the temperature change of a moving fluid element due to heat conduction processes and fluid motion.

3.2.2 General Boundary Conditions

For any particular problem, a set of appropriate initial and boundary conditions for the solution of the governing equations must be specified. The physical configuration of the flow requires several types of boundary conditions. They are the rigid wall with free-slip or no-slip condition, inflow and outflow boundaries and the free-surface boundary. The boundary conditions are imposed by prescribing the appropriate normal and tangential velocities at the boundaries.

For the rigid non-penetrating wall boundaries, all the normal velocity components are set to zero. For a free-slip, rigid wall, the tangential velocity components should have no normal gradient at the boundary. For a no-slip, non-penetrating rigid wall, in addition to the normal velocity conditions, the tangential velocities must also be set to zero.

The inflow boundaries prescribe the conditions of fluid influx through the boundary. The velocity components are

prescribed with the desired input flow. At the outflow boundaries, the external velocities are set equal to the adjacent velocities inside the fluid, which gives a smooth transition of the flow through the boundary.

The free surface is assumed stable and therefore the time-averaged normal velocity component is set to zero. Furthermore, no shear stress is transmitted through the free surface; thus, the tangential velocity components are set to have no normal gradient at the boundaries.

3.2.3 Initial and Thermal Boundary Conditions

A number of thermal boundary conditions can be specified for solving the energy equation depending on the physical situation. As examples of the thermal boundary conditions, one can specify an isothermal boundary where the temperature is a prescribed value, or an adiabatic boundary which corresponds to zero heat flux through the boundary. Heat sources can be added in a variety of ways. Convective motion is initiated by imposing a temperature gradient across the fluid layers. The effect of temperature variation which influences the fluid motion is calculated based on the Boussinesq approximation. However, in analyzing the thermal behaviour of recirculating buoyancy-driven flows in the present use, it is readily shown that the Archimede's number is small ($Gr/Re^2 \approx 10^{-2}$). This demonstrates that the

thermal buoyancy effects can be ignored for the flows of interest in the present investigations.

The initial condition considers a stagnant liquid wherein the gas injection begins at time = 0. The liquid at the beginning of the injection is stationary with a zero velocity field and zero differential pressure.

3.2.4 Calculating the Effective Viscosity

In the modelling of turbulent recirculating flows, the predicted flow fields depend on the turbulence models used. The problem of turbulence can be studied by simulating the turbulence effects on the flow fields through the use of semi-empirical expressions for the effective viscosity derived based on the Prandtl mixing-length theory. In previous works, the k-w or the k-ε two-equations models have been used for predicting the turbulent recirculatory flows in two dimensions.

While these turbulence models do appear to provide satisfactory predictions for a wide range of turbulent recirculating flows, it would be advantageous to have a simpler model which would reduce the computational costs particularly when dealing with three-dimensional and transient flow problems. The effective viscosity used in the present work is calculated from a simple algebraic expression presented by Pun and Spalding [32] which was also adopted by

Deb Roy et al. [29]. They proposed that

$$\mu_{eff} = C_1 (D)^{2/3} (H)^{-1/3} \rho_1^{2/3} (m_j w_j^2)^{1/3} \tag{3.7}$$

where D and H are the diameter and height of the vessel respectively; m_j is the mass flow rate of the gas and w_j is the gas velocity at the jet nozzle. The constant of proportionality C_1, according to Pun and Spalding, has a value of 0.012.

Deb Roy et al. showed that this expression is adequate for representing the turbulent viscosity in gas agitated systems by comparing the flow predictions using Eqn. (3.7) with results obtained from using the k-ε turbulence model. Both results exhibit similarity in most parts of the flow domain except the "near wall" regions. Comparison with the experimental measurements reported by Szekely, Wang and Kiser [23] also showed good agreement.

More recently, Sahai and Guthrie [33] proposed another expression for the effective viscosity for gas bubble/jetting systems in ladles. The effective viscosity is given as,

$$\mu_{eff} = 0.0055\ \rho_l H \left[\frac{(1-\bar{\alpha}) g \dot{Q}_g}{D}\right]^{1/3} \tag{3.8}$$

where $\dot{Q}_g$ represents the volumetric gas flow rate referenced to mid-height and mean liquid temperature. $\bar{\alpha}$ is the void

fraction of the gas within the gas-liquid plume. This expression stresses the importance of the pressure energy as opposed to the kinetic energy of the entering gas jet. This model was tested by Sahai and Guthrie by comparing results from the proposed effective viscosity model with those predicted by the k-ε model. The results agreed well for both models.

3.2.5 Calculating the Void Fraction and Density

The prediction of the hydrodynamics of the recirculating flows caused by gas injection involved the treatment of two-phase flows. The recirculation can be considered as being buoyancy driven and resulting from a lower density gas-liquid mixture in the region above the gas injection point in the vessel. One should note that the buoyancy forces exceed the inertial forces in the penetrating gas by a factor of approximately 2000. The buoyancy force driving the flow was determined from the average void fraction.

For the single-phase region, away from the gas-liquid plume, the void fraction is zero. For the purpose of modelling, in the two-phase region, the average void fraction was obtained from the mass balance on the gas phase [64].

The average void fraction, $\bar{\alpha}$, is thus calculated from the following relation,

$$\bar{\alpha} = \frac{Q_g}{\int_o^A (w+w_{slip})\,dA} \tag{3.9}$$

where Q_g is the volumetric flow rate of the gas and w_{slip} is the relative or slip velocity between the gas and the liquid phase. While the value of w_{slip} varies depending on the bubble and flow pattern, no analytical techniques are available at present for its determination. Davenport et al. [65] determined experimentally the slip velocity for spherical cap bubbles to be 0.4 m/sec. Consequently, arbitrary values of 0.4 - 0.6 m/sec for w_{slip} were considered in the present investigations.

If the gas bubbles move at the same velocity with the fluid, the slip velocity is zero. For no-slip condition, the expression for $\bar{\alpha}$ in Eqn. (3.9) reduces to

$$\bar{\alpha} = \frac{Q_g}{\int_o^A w\,dA} \tag{3.10}$$

which gives a higher void fraction for the same flow.

The density, ρ, appearing in the differential equations in Section 3.2.1 is calculated from the following expressions:

$$\rho = (1-\bar{\alpha})\rho_l + \bar{\alpha}\rho_g \qquad \text{for} \quad r<r_c(z) \tag{3.11}$$

and

$$\rho = \rho_l \quad \text{for } r \geq r_c(z) \tag{3.12}$$

where r_c is the radius of the two-phase gas-liquid column. Equation (3.11) computes the density within the gas-liquid mixture region using the average void fraction. The density outside the gas-liquid core is equal to the density of the liquid as indicated by Eqn. (3.12).

3.3 NUMERICAL PROCEDURE USING FINITE DIFFERENCE METHOD

To solve the set of governing differential equations given in Section 3.2.1, the equations were written in finite difference form using Taylor's Expansion Theorem.

3.3.1 Grid Network

The computation region was divided into a number of cylindrical mesh cells as shown in Fig. 3.2. A layer of fictitious cells surrounding the fluid field has been used to impose the necessary boundary conditions on the system. A typical fluid cell or volume element is shown in Fig. 3.3. The subscripts i, j, k are the indices for the radial, tangential, and axial direction respectively. The density, pressure, viscosity and temperature are referenced to the cell centers and represented by $S_{i,j,k}$, whereas the velocity, the momentum, normal and shear stress, are calculated on the faces of the cell.

A typical grid system comprising fifteen segments in the radial direction, eight in the tangential direction, and seven in the axial direction has been chosen for most of the computations. Unequal mesh sizes in the radial and axial directions are used for regions where the variation of the flow properties are significant.

3.3.2 Derivation of Finite Difference Equations

The finite difference forms of the differential equations are written for unequal mesh size. The quantities needed at positions other than those where they are defined are calculated as simple averages or weighted averages.

3.3.2.1 Continuity Equation

The finite difference approximation representing the continuity equation for a typical cell (i,j,k) for unequal mesh size in the radial and axial direction is:

$$\frac{1}{\Delta r_i}\left[u_{i+\frac{1}{2},j,k}\bar{\rho}_{i+\frac{1}{2},j,k}-u_{i-\frac{1}{2},j,k}\bar{\rho}_{i-\frac{1}{2},j,k}\right]$$

$$+\frac{1}{r_i\Delta\phi}\left[v_{i,j+\frac{1}{2},k}\bar{\rho}_{i,j+\frac{1}{2},k}-v_{i,j-\frac{1}{2},k}\bar{\rho}_{i,j-\frac{1}{2},k}\right]$$

$$+\frac{1}{\Delta z_k}\left[w_{i,j,k+\frac{1}{2}}\bar{\rho}_{i,j,k+\frac{1}{2}}-w_{i,j,k-\frac{1}{2}}\bar{\rho}_{i,j,k-\frac{1}{2}}\right]$$

$$+\frac{1}{2r_i}\left[u_{i+\frac{1}{2},j,k}\bar{\rho}_{i+\frac{1}{2},j,k}+u_{i-\frac{1}{2},j,k}\bar{\rho}_{i-\frac{1}{2},j,k}\right]=0 \qquad (3.13)$$

where $\bar{\rho}$ is the weighted density defined as:

$$\bar{\rho}_{i+\frac{1}{2},j,k} = \frac{\rho_{i,j,k}\Delta r_{i+1} + \rho_{i+1,j,k}\Delta r_i}{(\Delta r_i + \Delta r_{i+1})} \tag{3.14}$$

$$\bar{\rho}_{i,j+\frac{1}{2},k} = \frac{\rho_{i,j+1,k} + \rho_{i,j,k}}{2} \tag{3.15}$$

$$\bar{\rho}_{i,j,k+\frac{1}{2}} = \frac{\rho_{i,j,k}\Delta z_{k+1} + \rho_{i,j,k+1}\Delta z_k}{(\Delta z_k + \Delta z_{k+1})} \tag{3.16}$$

For equal mesh size, Eqns. (3.14) and (3.16) reduce to

$$\bar{\rho}_{i+\frac{1}{2},j,k} = \frac{\rho_{i,j,k}\Delta r + \rho_{i+1,j,k}\Delta r}{(\Delta r + \Delta r)}$$

$$= \frac{\rho_{i,j,k} + \rho_{i+1,j,k}}{2} \tag{3.17}$$

and

$$\bar{\rho}_{i,j,k+\frac{1}{2}} = \frac{\rho_{i,j,k} + \rho_{i,j,k+1}}{2} \tag{3.18}$$

which is the average density of the two adjacent cells at the interface.

3.3.2.2 Momentum Equations

Equations (3.3) to (3.5) of the momentum equations may be expressed in an explicit finite difference form for $(\rho u)^{n+1}_{i+\frac{1}{2},j,k}$, $(\rho v)^{n+1}_{i,j+\frac{1}{2},k}$ and $(\rho w)^{n+1}_{i,j,k+\frac{1}{2}}$ as follows:

$$(\rho u)^{n+1}_{i+\frac{1}{2},j,k} = (\rho u)_{i+\frac{1}{2},j,k} + \delta t\left[\frac{P_{i,j,k}-P_{i+1,j,k}}{(\Delta r_i+\Delta r_{i+1})/2} + \rho_{i,j,k}\, g_r - CUX - CUY - CUZ - CUC1 + CUC2 + \mu_{eff}(VISX1+VISX2+VISX3+VISX4 -VISX5-VISX6)\right] \quad (3.19)$$

$$(\rho v)^{n+1}_{i,j+\frac{1}{2},k} = (\rho v)_{i,j+\frac{1}{2},k} + \delta t\left[\frac{P_{i,j,k}-P_{i,j+1,k}}{r_i \Delta\phi} + \rho_{i,j,k}\, g_\phi - CVX - CVY - CVZ - CVC + \mu_{eff}(VISY1+VISY2+VISY3+VISY4 +VISY5-VISY6)\right] \quad (3.20)$$

$$(\rho w)^{n+1}_{i,j,k+\frac{1}{2}} = (\rho w)_{i,j,k+\frac{1}{2}}$$

$$+ \delta t\left[\frac{P_{i,j,k}-P_{i,j,k+1}}{(\Delta z_k+\Delta z_{k+1})/2} + \rho_{i,j,k}\, g_z\right.$$

$$- CWX - CWY - CWZ - CWC$$

$$\left. + \mu_{eff}(VISZ1+VISZ2+VISZ3+VISZ4)\right] \qquad (3.21)$$

In Eqn. (3.19) through (3.21), quantities with the superscript 'n+1' refer to the (n+1)th time step, whereas, quantities without a superscript are evaluated at the nth time step. In Eqn. (3.19), the terms CUX, CUY, CUZ, CUC1, CUC2 are the convective terms in the radial momentum equation and VISX1, VISX2, VISX3, VISX4, VISX5, VISX6 are the viscous terms in the radial direction. Similar terms in Eqns. (3.20) and (3.21) have similar representation.

For quantities needed at locations other than those where they are defined (see Fig. 3.3), an average is taken. For example, if the radial velocity is needed at the center of the cell, the velocity at the center is written as:

$$\bar{u}_{i,j,k} = \frac{u_{i+\frac{1}{2},j,k}+u_{i-\frac{1}{2},j,k}}{2} \qquad (3.22)$$

where $\bar{u}_{i,j,k}$ is used to represent the velocity at the center of the cell (i,j,k). Similarly, the tangential and axial velocity at the center of the cell (i,j,k) are

$$\bar{v}_{i,j,k} = \frac{v_{i,j+\frac{1}{2},k}+v_{i,j-\frac{1}{2},k}}{2} \tag{3.23}$$

and

$$\bar{w}_{i,j,k} = \frac{w_{i,j,k+\frac{1}{2}}+w_{i,j,k-\frac{1}{2}}}{2} \tag{3.24}$$

For quantities that are needed at the corner of the cell, a weighted average may be derived from the adjacent unequal cells.

$$\bar{u}_{i+\frac{1}{2},j,k+\frac{1}{2}} = \frac{u_{i+\frac{1}{2},j,k}\Delta z_{k+1}+u_{i+\frac{1}{2},j,k+1}\Delta z_{k}}{(\Delta z_{k}+\Delta z_{k+1})} \tag{3.25}$$

$$\bar{u}_{i+\frac{1}{2},j+\frac{1}{2},k} = \frac{u_{i+\frac{1}{2},j,k}+u_{i+\frac{1}{2},j+1,k}}{2} \tag{3.26}$$

$$\bar{v}_{i+\frac{1}{2},j+\frac{1}{2},k} = \frac{v_{i,j+\frac{1}{2},k}\Delta r_{i+1}+v_{i+1,j+\frac{1}{2},k}\Delta r_{i}}{(\Delta r_{i}+\Delta r_{i+1})} \tag{3.27}$$

$$\bar{v}_{i,j+\frac{1}{2},k+\frac{1}{2}} = \frac{v_{i,j+\frac{1}{2},k}\Delta z_{k+1}+v_{i,j+\frac{1}{2},k+1}\Delta z_{k}}{(\Delta z_{k}+\Delta z_{k+1})} \tag{3.28}$$

$$\bar{w}_{i+\frac{1}{2},j,k+\frac{1}{2}} = \frac{w_{i,j,k+\frac{1}{2}}\Delta r_{i+1}+w_{i+1,j,k+\frac{1}{2}}\Delta r_{i}}{(\Delta r_{i}+\Delta r_{i+1})} \tag{3.29}$$

$$\bar{w}_{i,j+\frac{1}{2},k+\frac{1}{2}} = \frac{w_{i,j,k+\frac{1}{2}}+w_{i,j+1,k+\frac{1}{2}}}{2} \tag{3.30}$$

Equations (3.26) and (3.30) are the average velocities of the adjacent cells, because the mesh size in the tangential direction is taken as equal. For equal mesh size in the radial and axial directions, the remaining equations in (3.25) to (3.30) reduce to the similar form. Scalar quantities at these corner points (example density) are derived in the same average form from the surrounding cells. For example,

$$\bar{\rho}_{i+\frac{1}{2},j,k+\frac{1}{2}} = \frac{\bar{\rho}_{i+\frac{1}{2},j,k}\Delta z_{k+1} + \bar{\rho}_{i+\frac{1}{2},j,k+1}\Delta z_{k}}{(\Delta z_{k} + \Delta z_{k+1})} \tag{3.31}$$

or

$$\bar{\rho}_{i+\frac{1}{2},j,k+\frac{1}{2}} = \frac{\bar{\rho}_{i,j,k+\frac{1}{2}}\Delta r_{i+1} + \bar{\rho}_{i+1,j,k+\frac{1}{2}}\Delta r_{i}}{(\Delta r_{i} + \Delta r_{i+1})} \tag{3.32}$$

Equations (3.31) and (3.32) are equivalent. For equal mesh size, the density at the corner point is the average of the four surrounding cells, that is

$$\bar{\rho}_{i+\frac{1}{2},j,k+\frac{1}{2}} = \frac{1}{4}\left(\rho_{i,j,k} + \rho_{i+1,j,k} + \rho_{i,j,k+1} + \rho_{i+1,j,k+1}\right) \tag{3.33}$$

Equations (3.31) and (3.32) can also be derived from Eqns. (3.16) and (3.14) respectively by changing the indices accordingly. Similar equations for other points can be derived from Eqns. (3.14) through (3.16).

Where a product is required, the average is first taken and then the product is formed. The convective and viscous terms in Eqn. (3.19) for the radial direction can then be written as follows:

$$CUX = \frac{\partial \rho u^2}{\partial r}$$

$$= \frac{(\bar{u}_{i+1,j,k})^2 \rho_{i+1,j,k} - (\bar{u}_{i,j,k})^2 \rho_{i,j,k}}{(\Delta r_i + \Delta r_{i+1})/2} \qquad (3.34)$$

$$CUY = \frac{1}{r} \frac{\partial \rho uv}{\partial \phi}$$

$$= \frac{1}{\Delta r_i (r_i + \frac{\Delta r_i}{2}) \Delta \phi} [\bar{u}_{i+\frac{1}{2},j+\frac{1}{2},k} \bar{v}_{i+\frac{1}{2},j+\frac{1}{2},k} \bar{\rho}_{i+\frac{1}{2},j+\frac{1}{2},k}$$

$$- \bar{u}_{i+\frac{1}{2},j-\frac{1}{2},k} \bar{v}_{i+\frac{1}{2},j-\frac{1}{2},k} \bar{\rho}_{i+\frac{1}{2},j-\frac{1}{2},k}] \qquad (3.35)$$

$$CUZ = \frac{\partial \rho uw}{\partial z}$$

$$= \frac{\bar{u}_{i+\frac{1}{2},j,k+\frac{1}{2}} \bar{w}_{i+\frac{1}{2},j,k+\frac{1}{2}} \bar{\rho}_{i+\frac{1}{2},j,k+\frac{1}{2}} - \bar{u}_{i+\frac{1}{2},j,k-\frac{1}{2}} \bar{w}_{i+\frac{1}{2},j,k-\frac{1}{2}} \bar{\rho}_{i+\frac{1}{2},j,k-\frac{1}{2}}}{\Delta z_k} \qquad (3.36)$$

$$CUC1 = \frac{\rho u^2}{r}$$

$$= \frac{\bar{\rho}_{i+\frac{1}{2},j,k}}{\Delta r_i (r_i + \frac{\Delta r_i}{2})} [\frac{(\bar{u}_{i,j,k})^2 \Delta r_{i+1} + (\bar{u}_{i+1,j,k})^2 \Delta r_i}{(\Delta r_i + \Delta r_{i+1})}] \qquad (3.37)$$

$$CUC2 = \frac{\rho v^2}{r}$$

$$= \frac{1}{r_i} (\bar{v}_{i,j,k})^2 \rho_{i,j,k} \tag{3.38}$$

$$VISX1 = \frac{\partial^2 u}{\partial r^2}$$

$$= \frac{u_{i+3/2,j,k}\Delta r_i + u_{i-\frac{1}{2},j,k}\Delta r_{i+1} - u_{i+\frac{1}{2},j,k}(\Delta r_i + \Delta r_{i+1})}{\Delta r_i \Delta r_{i+1} (\Delta r_i + \Delta r_{i+1})/2} \tag{3.39}$$

$$VISX2 = \frac{1}{r} \frac{\partial u}{\partial r}$$

$$= \frac{1}{\Delta r_i / (r_i + \frac{}{2})} \left[\frac{\bar{u}_{i+1,j,k} - \bar{u}_{i-1,j,k}}{(\Delta r_i + \Delta r_{i+1})/2}\right] \tag{3.40}$$

$$VISX3 = \frac{1}{r^2} \frac{\partial^2 u}{\partial \phi^2}$$

$$= \frac{1}{\Delta r_i / (r_i + \frac{}{2})^2} \left[\frac{u_{i+\frac{1}{2},j+1,k} - 2u_{i+\frac{1}{2},j,k} + u_{i+\frac{1}{2},j-1,k}}{\Delta \phi^2}\right] \tag{3.41}$$

$$VISX4 = \frac{\partial^2 u}{\partial z^2}$$

$$= [u_{i+\frac{1}{2},j,k+1}(\Delta z_k + \Delta z_{k-1}) + u_{i+\frac{1}{2},j,k-1}(\Delta z_k + \Delta z_{k+1})$$

$$- u_{i+\frac{1}{2},j,k}(\Delta z_{k+1} + \Delta z_{k-1} + 2\Delta z_k)]$$

$$/ \frac{1}{8} (\Delta z_k + \Delta z_{k+1})(\Delta z_{k-1} + \Delta z_k)(\Delta z_{k+1} + \Delta z_{k-1} + 2\Delta z_k) \tag{3.42}$$

$$\text{VISX5} = \frac{2}{r^2}\frac{\partial v}{\partial \phi}$$

$$= \frac{2(v_{i,j+\frac{1}{2},k} - v_{i,j-\frac{1}{2},k})}{r_i^2 \Delta\phi} \tag{3.43}$$

$$\text{VISX6} = \frac{u}{r^2}$$

$$= \frac{\bar{u}_{i,j,k}}{r_i^2} \tag{3.44}$$

All the quantities in the above convective and viscous terms are evaluated at the nth time step. Solving the finite difference equations written in the centered-difference form is often numerically unstable and generally requires some artificial viscosity for stable solutions. An upwind differencing scheme is included in the convective terms of the momentum equations to achieve stability. Equations (3.34) through (3.38) with the upwind differencing become:

$$\text{CUX} = \frac{(\bar{u}_{i+1,j,k})^2 \rho_{i+1,j,k} - (\bar{u}_{i,j,k})^2 \rho_{i,j,k}}{(\Delta r_i + \Delta r_{i+1})/2}$$

$$+ \frac{\zeta}{2}\left[\frac{|\bar{u}_{i+1,j,k}|(u_{i+\frac{1}{2},j,k} - u_{i+3/2,j,k})\rho_{i+1,j,k}}{\Delta r_{i+1}}\right.$$

$$\left. - \frac{|\bar{u}_{i,j,k}|(u_{i-\frac{1}{2},j,k} - u_{i+\frac{1}{2},j,k})\rho_{i,j,k}}{\Delta r_i}\right] \tag{3.45}$$

$$CUY = \frac{1}{(r_i+\frac{\Delta r_i}{2})\Delta\phi}\,[\bar{u}_{i+\frac{1}{2},j+\frac{1}{2},k}\bar{v}_{i+\frac{1}{2},j+\frac{1}{2},k}\bar{\rho}_{i+\frac{1}{2},j+\frac{1}{2},k}$$

$$-\bar{u}_{i+\frac{1}{2},j-\frac{1}{2},k}\bar{v}_{i+\frac{1}{2},j-\frac{1}{2},k}\bar{\rho}_{i+\frac{1}{2},j-\frac{1}{2},k}]$$

$$+\frac{\zeta}{2(r_i+\frac{\Delta r_i}{2})\Delta\phi}\,[|\bar{v}_{i+\frac{1}{2},j+\frac{1}{2},k}|(u_{i+\frac{1}{2},j,k}-u_{i+\frac{1}{2},j+1,k})$$

$$\bar{\rho}_{i+\frac{1}{2},j+\frac{1}{2},k}$$

$$-|\bar{v}_{i+\frac{1}{2},j-\frac{1}{2},k}|(u_{i+\frac{1}{2},j-1,k}-u_{i+\frac{1}{2},j,k})\bar{\rho}_{i+\frac{1}{2},j-\frac{1}{2},k}] \tag{3.46}$$

$$CUZ = \frac{1}{\Delta z_k}\,[\bar{u}_{i+\frac{1}{2},j,k+\frac{1}{2}}\bar{w}_{i+\frac{1}{2},j,k+\frac{1}{2}}\bar{\rho}_{i+\frac{1}{2},j,k+\frac{1}{2}}$$

$$-\bar{u}_{i+\frac{1}{2},j,k-\frac{1}{2}}\bar{w}_{i+\frac{1}{2},j,k-\frac{1}{2}}\bar{\rho}_{i+\frac{1}{2},j,k-\frac{1}{2}}]$$

$$+\frac{\zeta}{2}\,[\frac{|\bar{w}_{i+\frac{1}{2},j,k+\frac{1}{2}}|(u_{i+\frac{1}{2},j,k}-u_{i+\frac{1}{2},j,k+1})\bar{\rho}_{i+\frac{1}{2},j,k+\frac{1}{2}}}{(\Delta z_k+\Delta z_{k+1})/2}$$

$$-\frac{|\bar{w}_{i+\frac{1}{2},j,k-\frac{1}{2}}|(u_{i+\frac{1}{2},j,k-1}-u_{i+\frac{1}{2},j,k})\bar{\rho}_{i+\frac{1}{2},j,k-\frac{1}{2}}}{(\Delta z_k+\Delta z_{k-1})/2}] \tag{3.47}$$

$$CUC1 = \frac{\bar{\rho}_{i+\frac{1}{2},j,k}}{(r_i+\frac{\Delta r_i}{2})}\,[\frac{(\bar{u}_{i,j,k})^2\Delta r_{i+1}+(\bar{u}_{i+1,j,k})^2\Delta r_i}{(\Delta r_{i+1}+\Delta r_i)}$$

$$+\frac{\zeta\bar{\rho}_{i+\frac{1}{2},j,k}}{2(r_i+\frac{\Delta r_i}{2})}\,[|\bar{u}_{i,j,k}|(u_{i-\frac{1}{2},j,k}-u_{i+\frac{1}{2},j,k})\Delta r_{i+1}$$

$$+|\bar{u}_{i+1,j,k}|(u_{i+\frac{1}{2},j,k}-u_{i+3/2,j,k})\Delta r_i]/(\Delta r_i+\Delta r_{i+1}) \tag{3.48}$$

$$CUC2 = \frac{1}{r_i} (\bar{v}_{i,j,k})^2 \rho_{i,j,k}$$

$$+ \zeta[\frac{|\bar{v}_{i,j,k}| (v_{i,j-\frac{1}{2},k} - v_{i,j+\frac{1}{2},k}) \rho_{i,j,k}}{2r_i}] \quad (3.49)$$

The upwind differencing expressions are multiplied by a coefficient "ζ" which gives the desired amount of upstream or donor cell differencing. "ζ" takes a value between zero and unity. For "ζ" equal to zero, the difference equations reduce to the original equations which are centered-differenced. When "ζ" is equal to unity, the equations reduce to the full upstream or donor cell form. In general, "ζ" is chosen so that the numerical instability is reduced. This is discussed further in latter sections.

Similarly, the convective and viscous terms are written for Eqns. (3.20) and (3.21). This is presented in Appendix A.

3.3.2.3 Energy Equation

Temperatures are associated with the cell centers and the finite difference equation for Eqn. (3.6) can be written neglecting the dissipation terms as follows:

$$T^{n+1}_{i,j,k} = T_{i,j,k} + \delta t\{\frac{u_{i-\frac{1}{2},j,k}\overline{T}_{i-\frac{1}{2},j,k} - u_{i+\frac{1}{2},j,k}\overline{T}_{i+\frac{1}{2},j,k}}{\Delta r_i}$$

$$+ \frac{v_{i,j-\frac{1}{2},k}\overline{T}_{i,j-\frac{1}{2},k} - v_{i,j+\frac{1}{2},k}\overline{T}_{i,j+\frac{1}{2},k}}{r_i \Delta\phi}$$

$$+ \frac{w_{i,j,k-\frac{1}{2}}\overline{T}_{i,j,k-\frac{1}{2}} - w_{i,j,k+\frac{1}{2}}\overline{T}_{i,j,k+\frac{1}{2}}}{\Delta z_k}$$

$$- \frac{\overline{u}_{i,j,k}T_{i,j,k}}{r_i}$$

$$+ \frac{K}{\rho_{i,j,k}C_p}\left[\frac{T_{i+1,j,k}\Delta r_i + T_{i-1,j,k}\Delta r_{i+1} - T_{i,j,k}(\Delta r_i + \Delta r_{i+1})}{\Delta r_i \Delta r_{i+1}(\Delta r_i + \Delta r_{i+1})/2}\right.$$

$$+ \frac{T_{i,j+1,k} + T_{i,j-1,k} - 2T_{i,j,k}}{(r_i \Delta\phi)^2}$$

$$+ \frac{T_{i,j,k+1}\Delta z_k + T_{i,j,k-1}\Delta z_{k+1} - T_{i,j,k}(\Delta z_k + \Delta z_{k+1})}{\Delta z_k \Delta z_{k+1}(\Delta z_k + \Delta z_{k+1})/2}$$

$$\left. + \frac{T_{i+1,j,k} - T_{i-1,j,k}}{r_i\left(\frac{\Delta r_{i-1}}{2} + \Delta r_i + \frac{\Delta r_{i+1}}{2}\right)}\right]\} \qquad (3.50)$$

where the averaged temperatures, $\overline{T}$, are defined as

$$\overline{T}_{i+\frac{1}{2},j,k} = \frac{T_{i,j,k}\Delta r_{i+1} + T_{i+1,j,k}\Delta r_i}{(\Delta r_i + \Delta r_{i+1})} \qquad (3.51)$$

$$\overline{T}_{i,j+\frac{1}{2},k} = \frac{T_{i,j,k} + T_{i,j+1,k}}{2} \qquad (3.52)$$

$$\bar{T}_{i,j,k+\frac{1}{2}} = \frac{T_{i,j,k}\Delta z_{k+1} + T_{i,j,k+1}\Delta z_k}{(\Delta z_k + \Delta z_{k+1})} \tag{3.53}$$

3.3.3 Application of Boundary Conditions

The boundary conditions discussed in Section 3.2.2 can be easily imposed by prescribing the appropriate velocities in the fictitious cells surrounding the fluid region. For the present application, the walls are assumed to coincide with the cell boundaries.

A rigid, non-penetrating wall boundary can be imposed by setting the normal velocity to zero, since it is defined at the cell boundary. The tangential velocities in the surrounding fictitious cells are used to specify the appropriate viscous stresses at the boundary. That is, for a free-slip wall, these external velocities are set equal to the adjacent velocities in the fluid cells. For a no-slip wall, they are set equal to the negative of the adjacent velocities in the fluid. Considering the bottom boundary in Fig. 3.2: to impose the above-mentioned boundary conditions, the following statements may be prescribed. For a rigid, free-slip wall,

$$u_{i,j,1} = u_{i,j,2} \tag{3.54}$$

$$v_{i,j,1} = v_{i,j,2} \tag{3.55}$$

$$w_{i,j,1} = 0 \tag{3.56}$$

This is imposed for i = 1,IMAX and j = 1,JMAX. For a rigid, no-slip wall, Eqns. (3.54) and (3.55) are replaced by

$$u_{i,j,1} = -u_{i,j,2} \tag{3.57}$$

$$v_{i,j,1} = -v_{i,j,2} \tag{3.58}$$

For the cylindrical coordinate system, the grid is axisymmetric at the center. In the two-dimensional, axisymmetric calculations, the free-slip condition is specified at the axis of symmetry. For the three-dimensional asymmetric calculations, the boundary conditions at the central axis require special treatment. The velocities are prescribed so that the flow across the center continues smoothly without any disruptions. The conditions given in Eqns. (3.54) to (3.58) are imposed on the velocities calculated from the momentum equations, and this is done after each sweep through the mesh during the pressure correction iterations.

An inflow across the bottom boundary for example can be generated by inserting in place of Eqn. (3.56) the following:

$$w_{i,j,1} = w_{in} \qquad \text{for all i's and j's} \tag{3.59}$$

For a continuative or outflow boundary at the bottom, the velocities are set as follows:

$$u_{i,j,1} = u_{i,j,2}$$

$$v_{i,j,1} = v_{i,j,2} \qquad \text{for all i's and j's} \qquad (3.60)$$

$$w_{i,j,1} = w_{i,j,2}$$

However, these conditions are only imposed after each calculation of the momentum equations and not for every iteration of the pressure corrections.

In addition to the hydrodynamic boundary conditions, the thermal boundary conditions are imposed similarly as follows.

For an adiabatic bottom wall,

$$T_{i,j,1} = T_{i,j,2} \qquad \text{for all i's and j's} \qquad (3.61)$$

and for an isothermal boundary,

$$T_{i,j,1} = T_w \qquad \text{for all i's and j's} \qquad (3.62)$$

The boundary conditions for other boundaries are thus prescribed in a way similar to that already described for the bottom boundary. A different set of conditions, depending on the physical problem involved, can be imposed to obtain the solution of the governing differential equations.

3.3.4 Computational Procedure

An explicit finite difference scheme has been developed to solve the set of finite difference equations with the pressure and velocity as the primary dependent variables. The numerical technique was based on the Marker-and-Cell (MAC) method [2] which was originally developed at Los Alamos Scientific Laboratory for treating incompressible flow problems involving free surfaces and also for confined flows. The present program is written in explicit, transient mode. This means that a time-dependent solution is obtained by advancing the flow field variables through a sequence of short time steps, δt. The calculations proceed through a sequence of cycles where the computed results of each cycle are used as the initial conditions for the next cycle. This calculation continues for as many cycles as required for the desired results. A flow chart of the computer program is shown in Fig. 3.4.

The program starts by reading the input variables for the particular flow problem; then computing the constants in the problem and storing them for later use. The initial conditions of the velocities, pressures and temperatures are also specified at the beginning of the first cycle. Starting from the initially prescribed conditions, a first approximation of the flow field is obtained by solving the momentum equations. However, the newly computed velocities

may not satisfy the conservation of mass in each cell. This conservation constraint is imposed by adjusting the cell pressures. The newly adjusted pressures are used in the next computational cycle for the velocity calculations.

An iterative process is used for this purpose, in which the cell pressures are adjusted so that the conservation condition is satisfied by making the discrepancy vanish. The discrepancy or divergence in each cell (i,j,k) is defined from the continuity equation as:

$$D_{i,j,k} = \frac{1}{\Delta r_i}\left[u_{i+\frac{1}{2},j,k}\bar{\rho}_{i+\frac{1}{2},j,k} - u_{i-\frac{1}{2},j,k}\bar{\rho}_{i-\frac{1}{2},j,k}\right]$$

$$+ \frac{1}{r_i \Delta\phi}\left[v_{i,j+\frac{1}{2},k}\bar{\rho}_{i,j+\frac{1}{2},k} - v_{i,j-\frac{1}{2},k}\bar{\rho}_{i,j-\frac{1}{2},k}\right]$$

$$+ \frac{1}{\Delta z_k}\left[w_{i,j,k+\frac{1}{2}}\bar{\rho}_{i,j,k+\frac{1}{2}} - w_{i,j,k-\frac{1}{2}}\bar{\rho}_{i,j,k-\frac{1}{2}}\right]$$

$$+ \frac{1}{2r_i}\left[u_{i+\frac{1}{2},j,k}\bar{\rho}_{i+\frac{1}{2},j,k} + u_{i-\frac{1}{2},j,k}\bar{\rho}_{i-\frac{1}{2},j,k}\right] \quad (3.63)$$

If the divergence of a cell is negative corresponding to a net flow of mass into the cell, the excess inflow is eliminated by increasing the cell pressure. Similarly, for a net flow out of the cell, the cell pressure is decreased to reduce the outflow. In this way, the divergence for each cell can be forced to vanish. If the magnitude of the divergence reduces to a specified, small value ε, no pressure

adjustment is necessary for the cell. If $D_{i,j,k}$ is greater than the prescribed ε, the cell pressure and the velocity components on the side of the cell (i,j,k) are adjusted as follows:

$$p_{i,j,k} \to p_{i,j,k} + \delta p$$

$$u_{i+\frac{1}{2},j,k} \to u_{i+\frac{1}{2},j,k} + (\delta t/\Delta r_i)\delta p$$

$$u_{i-\frac{1}{2},j,k} \to u_{i-\frac{1}{2},j,k} - (\delta t/\Delta r_i)\delta p$$

$$v_{i,j+\frac{1}{2},k} \to v_{i,j+\frac{1}{2},k} + (\delta t/r_i\Delta\phi)\delta p$$

$$v_{i,j-\frac{1}{2},k} \to v_{i,j-\frac{1}{2},k} - (\delta t/r_i\Delta\phi)\delta p$$

$$w_{i,j,k+\frac{1}{2}} \to w_{i,j,k+\frac{1}{2}} + (\delta t/\Delta z_k)\delta p$$

$$w_{i,j,k-\frac{1}{2}} \to w_{i,j,k-\frac{1}{2}} - (\delta t/\Delta z_k)\delta p \qquad (3.64)$$

δp denotes the pressure change required to make the divergence vanish. The pressure correction, δp, is derived from the continuity equation and Eqn. (3.64). Substituting the adjusted velocity components from Eqn. (3.64) for the velocities in the continuity equation (Eqn. (3.13)), it results

$$\frac{1}{\Delta r_i}\left[\left(u_{i+\frac{1}{2},j,k}+\frac{\delta t\delta p}{\Delta r_i}\right)\bar{\rho}_{i+\frac{1}{2},j,k}-\left(u_{i-\frac{1}{2},j,k}-\frac{\delta t\delta p}{\Delta r_i}\right)\bar{\rho}_{i-\frac{1}{2},j,k}\right]$$

$$+\frac{1}{r_i\Delta\phi}\left[\left(v_{i,j+\frac{1}{2},k}+\frac{\delta t\delta p}{r_i\Delta\phi}\right)\bar{\rho}_{i,j+\frac{1}{2},k}-\left(v_{i,j-\frac{1}{2},k}-\frac{\delta t\delta p}{r_i\Delta\phi}\right)\bar{\rho}_{i,j-\frac{1}{2},k}\right]$$

$$+\frac{1}{\Delta z_k}\left[\left(w_{i,j,k+\frac{1}{2}}+\frac{\delta t\delta p}{\Delta z_k}\right)\bar{\rho}_{i,j,k+\frac{1}{2}}-\left(w_{i,j,k-\frac{1}{2}}-\frac{\delta t\delta p}{\Delta z_k}\right)\bar{\rho}_{i,j,k-\frac{1}{2}}\right]$$

$$+\frac{1}{2r_i}\left[\left(u_{i+\frac{1}{2},j,k}+\frac{\delta t\delta p}{\Delta r_i}\right)\bar{\rho}_{i+\frac{1}{2},j,k}+\left(u_{i-\frac{1}{2},j,k}-\frac{\delta t\delta p}{\Delta r_i}\right)\bar{\rho}_{i-\frac{1}{2},j,k}\right]$$

$$=0 \qquad (3.65)$$

Rearranging the terms,

$$\left[\frac{1}{\Delta r_i}\left(u_{i+\frac{1}{2},j,k}\bar{\rho}_{i+\frac{1}{2},j,k}-u_{i-\frac{1}{2},j,k}\bar{\rho}_{i-\frac{1}{2},j,k}\right)\right.$$

$$+\frac{1}{r_i\Delta\phi}\left(v_{i,j+\frac{1}{2},k}\bar{\rho}_{i,j+\frac{1}{2},k}-v_{i,j-\frac{1}{2},k}\bar{\rho}_{i,j-\frac{1}{2},k}\right)$$

$$+\frac{1}{\Delta z_k}\left(w_{i,j,k+\frac{1}{2}}\bar{\rho}_{i,j,k+\frac{1}{2}}-w_{i,j,k-\frac{1}{2}}\bar{\rho}_{i,j,k-\frac{1}{2}}\right)$$

$$\left.+\frac{1}{2r_i}\left(u_{i+\frac{1}{2},j,k}\bar{\rho}_{i+\frac{1}{2},j,k}+u_{i-\frac{1}{2},j,k}\bar{\rho}_{i-\frac{1}{2},j,k}\right)\right]$$

$$+\frac{\delta t\delta p}{\Delta r_i^2}\left(\bar{\rho}_{i+\frac{1}{2},j,k}+\bar{\rho}_{i-\frac{1}{2},j,k}\right)+\frac{\delta t\delta p}{r_i^2\Delta\phi^2}\left(\bar{\rho}_{i,j+\frac{1}{2},k}+\bar{\rho}_{i,j-\frac{1}{2},k}\right)$$

$$+\frac{\delta t\delta p}{\Delta z_k^2}\left(\bar{\rho}_{i,j,k+\frac{1}{2}}+\bar{\rho}_{i,j,k-\frac{1}{2}}\right)+\frac{\delta t\delta p}{2r_i\Delta r_i}\left(\bar{\rho}_{i+\frac{1}{2},j,k}-\bar{\rho}_{i-\frac{1}{2},j,k}\right)$$

$$=0 \qquad (3.66)$$

The terms in the square bracket are the divergence $D_{i,j,k}$ as defined in Eqn. (3.63). Rearranging Eqn. (3.66) gives:

$$\delta t \delta p \left(\frac{\bar{\rho}_{i+\frac{1}{2},j,k} + \bar{\rho}_{i-\frac{1}{2},j,k}}{\Delta r_i^2} + \frac{\bar{\rho}_{i,j+\frac{1}{2},k} + \bar{\rho}_{i,j-\frac{1}{2},k}}{r_i^2 \Delta \phi^2} \right.$$

$$\left. + \frac{\bar{\rho}_{i,j,k+\frac{1}{2}} + \bar{\rho}_{i,j,k-\frac{1}{2}}}{\Delta z_k^2} + \frac{\bar{\rho}_{i+\frac{1}{2},j,k} - \bar{\rho}_{i-\frac{1}{2},j,k}}{2 r_i \Delta r_i} \right)$$

$$= - D_{i,j,k} \qquad (3.67)$$

Then,

$$\delta p = - D_{i,j,k} / \delta t \left[\frac{1}{\Delta r_i^2} \left(\bar{\rho}_{i+\frac{1}{2},j,k} + \bar{\rho}_{i-\frac{1}{2},j,k} \right) \right.$$

$$+ \frac{1}{r_i^2 \Delta \phi^2} \left(\bar{\rho}_{i,j+\frac{1}{2},k} + \bar{\rho}_{i,j-\frac{1}{2},k} \right) + \frac{1}{\Delta z_k^2} \left(\bar{\rho}_{i,j,k+\frac{1}{2}} \right.$$

$$\left. \left. + \bar{\rho}_{i,j,k-\frac{1}{2}} \right) + \frac{1}{2 r_i \Delta r_i} \left(\bar{\rho}_{i+\frac{1}{2},j,k} - \bar{\rho}_{i-\frac{1}{2},j,k} \right) \right] \qquad (3.68)$$

or

$$\delta p = - \beta D_{i,j,k} \qquad (3.69)$$

where β is given by

$$\beta = \Omega / \delta t \left[\frac{1}{\Delta r_i^2} \left(\bar{\rho}_{i+\frac{1}{2},j,k} + \bar{\rho}_{i-\frac{1}{2},j,k} \right) \right.$$

$$\left. + \frac{1}{r_i^2 \Delta \phi^2} \left(\bar{\rho}_{i,j+\frac{1}{2},k} + \bar{\rho}_{i,j-\frac{1}{2},k} \right) \right.$$

$$+ \frac{1}{\Delta z_k^2} \left(\bar{\rho}_{i,j,k+\frac{1}{2}} + \bar{\rho}_{i,j,k-\frac{1}{2}}\right)$$

$$+ \frac{1}{2r_i \Delta r_i} \left(\bar{\rho}_{i+\frac{1}{2},j,k} - \bar{\rho}_{i-\frac{1}{2},j,k}\right)] \qquad (3.70)$$

The variable Ω is a relaxation factor. For values greater than unity, Ω is an overrelaxation factor which is used to accelerate the convergence of the iteration. For iteration stability, Ω must not be larger than 2.0. An optimum value for Ω of 1.7 is commonly used; but with large gradients in the flow, this value is too large. For the program, the value of Ω varies between 1.0 and 2.0 to obtain optimum convergence of the iteration.

The pressure change δp is computed for every cell and adjustments to the cell pressure and velocity are carried out according to Eqn. (3.64). However, an adjustment in one cell affects its neighbouring cells, so the process has to be done iteratively. The iteration is done by sweeping through the mesh with proper application of the boundary conditions and provided the flow does not change too rapidly from one cycle to the next and the chosen value of Ω is not excessively small, convergence is reached after a few iterations.

Once convergence has been achieved, all the flow variables (velocity, pressure) are at the advanced time level

and are used as starting values for the next cycle. The process is then repeated for time = 2δt, 3δt, ..., etc. until steady-state conditions have been established.

3.3.5 Stability and Accuracy Considerations

The solution of the governing differential equations by finite difference approximation often encounters numerical instability in the calculations. When the calculated results exhibit significant variations over the space or time steps, the accuracy and reliability of the results are questionable.

The explicit technique has the advantage that all the flow variables are known at the time the calculations are made, since the calculated variables from the preceding time step are used to compute the new values. However, a maximum time step exists which, if exceeded, causes the solution to become numerically unstable. The space and time increments selected must satisfy certain stability criteria.

The choice of the time increment necessary for stability is governed by two restrictions. The first requirement is similar to the Courant conditions which require that the time increment must be chosen such that no fluid moves through more than one computational cell in one time step or

$$\delta t < \min\left\{\frac{\Delta r}{|u|}\ ,\ \frac{r\Delta\phi}{|v|}\ ,\ \frac{\Delta z}{|w|}\right\} \tag{3.71}$$

where the minimum is taken with respect to all the cells in the grid network.

The second stability condition is related to the effect of the viscosity which can be written as

$$\delta t < \frac{1}{2\nu} \left(\frac{1}{\Delta r^2} + \frac{1}{(r\Delta\phi)^2} + \frac{1}{\Delta z^2}\right) \tag{3.72}$$

Both criteria must be satisfied and thus δt is chosen to satisfy the more restrictive condition of the two inequalities.

With the time step chosen small enough to prevent instability, refining the space grid improves the accuracy of the solution. The cell's grid should be small enough so that there are no significant variations of the flow variables across any cell. Finer mesh grids are used for regions where flow variables are changing quite significantly. Regions near the inlet or outlet, or near an obstruction, are examples of such areas. For most part of the flow, where changes are less significant across any cell, a coarser mesh grid may be used. This distinction supports the use of an unequal mesh grid in the derivation of the finite difference equations.

From Eqn. (3.71), a finer mesh grid would mean a smaller time step. If the time step is small enough to prevent instability, the solution obtained may be quite accurate.

A small time step, however, would demand excessive computations to generate the solution.

With the time increment chosen to satisfy both the stability criteria, the coefficient "ζ", used in the upwind differencing scheme (discussed in Section 3.3.2.2), must be chosen so that no unnecessary truncation errors are introduced to stabilize the calculations. The requirement for "ζ" is

$$1 \geq \zeta > \frac{3}{2} \max \left\{ \left|\frac{u\delta t}{\Delta r}\right|, \left|\frac{v\delta t}{r\Delta\phi}\right|, \left|\frac{w\delta t}{\Delta z}\right| \right\} \qquad (3.73)$$

If the value chosen for "ζ" is too large, unnecessary trunction errors may be introduced. Truncation errors are unavoidable in finite difference approximations, but unnecessary truncation influences the accuracy of the calculations.

3.4 RESULTS AND DISCUSSIONS

The program was written for three-dimensional flows and was tested for different flow conditions. Some of the selected results are presented and discussed in this section.

In order to test the reliability of the present code, a two-dimensional computation was performed and results compared with existing axisymmetric computations. The set of experimental conditions as those studied by Deb Roy et al. [29] were adopted, so that the numerical predictions for

the two-dimensional situations could be compared directly with previous computational results. The set of conditions for the air-water model is listed in Table 3.1.

Table 3.1. Parameters used in 2-D computations.

Diameter of vessel	0.6 m
Height of water	0.6 m
Velocity of air through orifice	1.62 m/sec
Orifice diameter	0.0127 m

The initial condition considers a stagnant liquid with zero velocity field and zero differential pressure. The liquid at the beginning is thermally stratified where a linear temperature gradient from the bottom of the vessel to the liquid surface is imposed. This will be similar to a situation where the liquid metal is allowed to settle in a ladle for some time. The gas injection begins at time t = 0, and the fluid density in the first computational cell where the gas is introduced, is taken as

$$\rho = (1-\bar{\alpha})\rho_l \tag{3.74}$$

To avoid the difficulty of $\bar{\alpha}\to\infty$ at time t = 0, for zero slip condition (see Eqn. (3.10)), an arbitrary non-zero value was assumed ($w_{t=0} = 0.0001 w_j$).

Flow patterns were predicted for central and off-centered bubble columns for different sets of flow conditions

and the energy equation was solved for analyzing the heat flow characteristics [66,67].

Figure 3.5(a) illustrates the computed velocity fields of the two-dimensional code which is to be compared with the two-dimensional axisymmetric solutions of Deb Roy et al. (Figure 3.5(b)). Both sets of computations were carried out for the same physical conditions (Table 3.1) used by Szekely, Wang, and Kiser [23]. The experimental results of Szekely et al. are illustrated in Fig. 3.5(c) for comparison. Reasonable agreement between the results produced by the two computational schemes is evident.

Figure 3.6 provides a comparison between the prediction of the velocity field by Guthrie et al. [68] using the two-dimensional k-ε model of turbulence, and the present model. A reasonable agreement is achieved between the two methods.

Figure 3.7 presents the computed velocity fields using the three-dimensional code for cylindrical jetting with slip. Velocities up to 0.35 m/sec are observed near the central vertical axis of the cylinder. The plume boundary is shown with dashed lines in all the figures. Considerable fluid entrainment outside the vertical plume is predicted with velocities ranging between 0.05 and 0.10 m/sec. The velocities are also larger in the downward flow region close to the wall. Somewhat lower velocities ranging between 0.02

and 0.04 m/sec are observed in the upper part of the vessel close to the container walls.

Figure 3.8 illustrates the case of a cylindrical central jet with zero slip. The predicted flow field is similar to that with slip. However, as would be anticipated, central velocities close to the vertical axis are higher, on account of a higher average void fraction for zero slip condition.

Figure 3.9 gives the comparison of the velocity fields produced by a cylindrical jet and a conical jet. In Fig. 3.9(b), the flow pattern is for a central jetting system where the rising plume is conical. A variable mesh grid was used for the computation. Comparison of the cylindrical and conical plumes shows that larger velocities occurred at the center of a conical plume. Figure 3.10 is a quantitative comparison of the predicted axial velocity distributions between the conical and cylindrical jetting. This is illustrated at three different heights (z/H = 0.05, 0.50, 0.95). One should note that the velocity profiles for the cylindrical plume are generally flatter than those for the conical plume. Close to the jet entrance, the axial plume velocities are relatively low, increasing at mid-height and then becoming lower close to the liquid surface.

Figure 3.11 illustrates the developing velocity fields for three different values of r_c/R ratio (r_c/R = 0.16, 0.19, 0.24) at time equal 10.0 seconds after jetting. The flow

outside the plume has not been fully developed in the whole domain. Figure 3.12 illustrates the same flow conditions but at 40.0 seconds after jetting. One can see that the flow is more developed at this stage. This comparison is useful for studying the effect of the size of the two-phase gas-liquid mixture. The quantitative comparison of the three different results is illustrated in Fig. 3.13 for $z/H = 0.29$, 0.62 and 0.86. It is seen that the flow profile varies quite significantly in the region close to the axis of the container. For smaller ratio of r_c/R, the velocity is higher. However, the variation of r_c/R does not affect the velocity field in most areas of the flow region away from the axis.

Figure 3.14 presents the predicted velocity pattern in a vertical plane passing through the off-centered orifice. The jetting occurred at three-quarter the distance between the center axis and the side wall. It also shows the velocity pattern within horizontal planes corresponding to levels, a-a (at $z/H = 0.95$) and b-b (at $z/H = 0.05$). One observes velocities of 0.2-0.3 m/sec within the gas bubble plume. The fluid moves away from the rising plume towards the opposite wall at the top level ($z/H = 0.95$) and the flow moves back from the opposite walls towards the jet at $z/H = 0.05$. Figure 3.15 predicts the effect of a plume rising close to the side wall. Again, both the vertical and horizontal planes are shown.

Figure 3.16 is the flow pattern for an off-centered jet predicted by Wong [69]. Wong used a steady-state, turbulent, three-dimensional model developed based on the Imperial College Control Volume Technique and the "SIMPLE" procedure. A comparison of the result with the present model shows good agreement between the two methods.

Finally, Figures 3.17 and 3.18 illustrate the temperature distribution within a thermally stratified liquid following 5.0 and 12.5 seconds of bubbling, respectively. It was assumed that heat losses had occurred through the bottom of the vessel but none through the top and side walls of the vessel (i.e. insulated), so that a vertical temperature gradient had been established at time = 0. As seen in Fig. 3.18, after 12.5 seconds, cold liquid at the bottom has moved towards the top of the vessel. Liquid in the lower outer regions still exhibits considerable temperature stratification. Uniform temperature distribution within the vessel is achieved when steady-state is reached.

The model developed here has demonstrated the important role that modelling can play in ladle metallurgy processes. The present model points to quantitative predictions and simulations of the fluid flow and heat transfer phenomena of the process. The agreement between the predicted results and existing measurements and predictions indicates that the

present model is a promising approach for the study of recirculating flows in the steel processing operations. The method can be extended to several chemical and metallurgical processing operations involving gas-injection operations.

CHAPTER IV

INVESTIGATION OF HEAT TRANSFER DURING SOLIDIFICATION IN MOLDS

4.1 PHYSICAL MODEL

The solidification process is basically a problem of unsteady-state heat flow in three dimensions. The modelling of the solidification process, however, is one of considerable mathematical complexity. As solidification takes place, heat transfer occurs in three ways - conduction, convection, and radiation. These are defined by the Fourier, Newton, and Stefan-Boltzmann laws, respectively. Numerical solutions of the differential equations derived from these laws can be obtained by finite-difference approximations. In most casting and ingot-making processes, the solidification of the metal involves a phase change which results in the release of latent heat of fusion. The problem becomes even more complex when the thermal properties of the mold and metal are temperature-dependent, or when solidification of alloys or metals with crystals of complex geometries are considered. Some of these problems are considered and discussed in this chapter. There are, however, certain simplifying assumptions which are made to investigate a number of cases which are of interest.

The purpose is to develop a model to simulate the solidification of an ingot in a mold and to determine the temperature distribution in the ingot and mold, the solidification front profile, and the solidification time. Computations will be carried out for both rectangular and circular molds which may require two- or three-dimensional treatments. The mold is assumed to be filled instantaneously with molten metal at the start of the computations, and is allowed to cool and solidify under normal ambient conditions. Formation of air-gap, liberation of latent heat of fusion during cooling and variation of the thermal properties will be dealt with in the model.

4.2 MATHEMATICAL FORMULATION

4.2.1 General Equation of Heat Flow

The unsteady-state heat flow equation is derived by considering the energy balance on a differential element of volume of the material subject to a conduction process. The sum of the total heat absorbed by the element per unit time due to heat flow and the internal heat generated in the element per unit time is equal to the net increase of internal energy of the element per unit time. The general equation of heat conduction, written in three-dimensional cartesian coordinates is,

$$\frac{\partial}{\partial x}\left(K\frac{\partial T}{\partial x}\right)+\frac{\partial}{\partial y}\left(K\frac{\partial T}{\partial y}\right)+\frac{\partial}{\partial z}\left(K\frac{\partial T}{\partial z}\right)+Q_{gen}=\rho C_p\frac{\partial T}{\partial t} \tag{4.1}$$

The first three terms on the left-hand side represent the net energy gain by conduction per unit time across the element surfaces. Q_{gen} is the energy generated in the element per unit time and the term on the right-hand side is the change of energy stored in the element per unit time. Often, practical problems in solidification processes involve cylindrical geometries. Hence the general equation written in cylindrical coordinates is

$$\frac{1}{r}\frac{\partial}{\partial r}\left(rK\frac{\partial T}{\partial r}\right)+\frac{1}{r^2}\frac{\partial}{\partial \phi}\left(K\frac{\partial T}{\partial \phi}\right)+\frac{\partial}{\partial z}\left(K\frac{\partial T}{\partial z}\right)+Q_{gen}=\rho C_p\frac{\partial T}{\partial t} \tag{4.2}$$

Both Eqns. (4.1) and (4.2) are written for variable conductivity, K.

4.2.2 Initial and Boundary Conditions

The prediction of the temperature field in a solidifying cast is essentially based on the solution of the unsteady-state heat flow equation given in Eqns. (4.1) or (4.2). In order to solve this equation, the boundary conditions which are characteristic of the process must be considered.

Since the problem is one of unsteady-state heat transfer, an initial condition must also be specified.

At the surface boundary, two cases of boundary conditions are considered:

i) Dirichlet boundary conditions for which the boundary surface temperature is known or given in the problem specifications.

ii) Neumann derivative boundary condition in which case the boundary surface temperature is not known and the boundary specification is in the form of knowledge about the outward normal gradient of temperature $\frac{\partial T}{\partial n}$. This may be convective, and the outward normal temperature gradient is written as

$$\frac{\partial T}{\partial n} = - \frac{h}{K} (T_w - T_a) \tag{4.3}$$

where h is the surface heat transfer coefficient. T_w is the boundary temperature and T_a is the ambient temperature. The normal temperature gradient may take the form

$$\frac{\partial T}{\partial n} = - \frac{FE\sigma}{K} (T_w^4 - T_a^4) \tag{4.4}$$

for radiative boundary, where F is a geometry factor, E is the emissivity, and σ is the Stefan-Boltzmann constant. If a particular boundary

is known to be adiabatic, the outward normal temperature gradient is set to zero, so that

$$\frac{\partial T}{\partial n} = 0 \tag{4.5}$$

Where heat transfer at the boundary is by both radiation and convection, the normal temperature gradient is expressed as

$$\frac{\partial T}{\partial n} = -\frac{h}{K}(T_w - T_a) - \frac{FE\sigma}{K}(T_w^4 - T_a^4) \tag{4.6}$$

Equation (4.6) may be written as

$$\frac{\partial T}{\partial n} = -\frac{h_{eff}}{K}(T_w - T_a) \tag{4.7}$$

where h_{eff} is the effective heat transfer coefficient of the surface which is calculated as follows:

$$h_{eff} = h + FE\sigma(T_w^2 + T_a^2)(T_w + T_a) \tag{4.8}$$

Initially, the mold is assumed to be at a uniform temperature T_{mo}, and is assumed to be filled instantaneously with liquid metal at the pouring temperature T_{co}. This assumption is valid only if the filling time is a small fraction of the total solidification time of the casting, in which case, this assumption would not introduce any significant errors. For processes, however, where rapid solidification occurs or where a large temperature variation

occurs during the filling, this assumption would not be valid. Hydrodynamic modelling of ladle tapping has been studied by several authors [70-72], and could be included in a more complex model of the pouring and solidification process. For the present investigation, the pouring time is neglected, and computations begin at time = 0.

Once the mold is filled, it is further assumed that the liquid metal remains stagnant, with no convective transport in the liquid phase. Because of the complexity of the interaction between the thermally induced natural convective flow field and the moving solidification front, the convective transport is not included in the present studies. For future development of the model, the transient effects of solidification accompanied by convective transport may be included for more detailed studies.

Initially, heat is transferred from the liquid metal across the metal/mold interface, through the mold and to the surroundings. Neglecting any thermal contact resistance at the interface, the initial metal/mold interfacial temperature can be shown to be [49],

$$T_{int} = T_{mo} + \frac{T_{co} - T_{mo}}{1 + \frac{K_m}{K_c}\sqrt{\frac{\alpha_c}{\alpha_m}}} \qquad (4.9)$$

where α_c is the thermal diffusivity of the metal and α_m that of the mold.

At the metal/mold interface, the metal and the mold are initially in good thermal contact and heat transfer is by conduction. As the metal solidifies, it contracts and breaks away from the mold. Eventually, an air-gap is formed between the solidified shell and the mold. The time of formation of the air-gap is one of the important controlling factors determining the quality of the casting. For the purpose of modelling, an air-gap formation time is assumed, depending on the casting size, shape and composition, type of mold, and initial temperature of the system. The gap is assumed to form all over the interface at the same instant.

The air-gap constitutes a major resistance to the heat flow. The temperature distribution across the metal/mold interface indicates an apparent temperature discontinuity. When there is perfect contact, the continuity of heat flow should be maintained. Therefore,

$$- K_c \frac{\partial T_c}{\partial n} = - K_m \frac{\partial T_m}{\partial n} \qquad (4.10)$$

But, usually a discontinuity exists in the temperature gradient, since $K_c \neq K_m$ in general.

Across the air-gap, heat transfer is mainly by radiation. Due allowance may be made for convection and there may also be some spot contacts between the casting and the mold. Some form of artificial heat transfer coefficient may be necessary to account for these additional two modes of

heat transfer mechanism, though in most cases, these may be neglected. However, there is no practical physical model of gap formation and heat transfer characteristics across narrow gaps, at operating metallurgical temperatures. Hence, an effective heat transfer coefficient for the air-gap was calculated based on the temperatures of the casting and mold across the air-gap. This is expressed as

$$h_g = h^* + FE\sigma(T_c^2+T_m^2)(T_c+T_m) \qquad (4.11)$$

where T_c and T_m are the temperatures of the casting and mold across the air-gap. h^* is the equivalent heat transfer coefficient accounting for the conduction heat flow at the contact spots. Since no measured values are available, h^* is arbitrarily assigned a value equal to 0.05 of the heat flux by conduction.

4.2.3 Thermal Properties

In modelling the solidification process, thermal properties play an important role in achieving good simulation results. The simulated results are only as good as the data input. There are currently many publications and reference sources with available thermal data. However, even with these sources, still no suitable data exists for the thermal properties especially for metals near their melting points or for liquid metals. Data at these temperatures are scarce and often conflicting. This constraint

is a limiting factor in the accuracy of the simulation.

Early analytical works [34-38] assumed constant thermal properties to obtain their solutions. Thermal properties like thermal conductivity, heat capacity, and density all vary with temperature to some degree in their magnitudes. For a typical casting process, the temperature may change over a wide range. Thus, the analytical solutions obtained by oversimplifying this assumption are not realistic and hence not of much practical use. To develop a model which promises to be useful, the thermal properties of the materials should be allowed to vary with temperature as they do in the actual situation.

Thermal conductivities are very temperature-dependent. Sometimes they vary widely over the temperature range typically found in the casting process. Although values of the thermal conductivities for typical engineering materials are available in literature, the variation of the thermal conductivities with temperature is not so readily available. Experimental determinations of the thermal conductivities have been carried out for many engineering materials, most of them are for pure materials. For alloys, little has been done. Until more of such data are available, it may be necessary to represent the variation of thermal conductivity by some correlations which follow the general trend as the available data for the materials involved.

An example is illustrated in Fig. 4.1. The thermal conductivity of low-carbon steel is represented by four linear segments over the temperature range. Figure 4.2 illustrates another example for molding sand used by Marrone et al. [48]. Faced with a wide spectrum of available thermal conductivity data, a polynomial regression was performed to choose the best quadratic curve fit based on the least squares method. These curves appear to give reasonable results.

The density variation with temperature within a given phase (liquid or solid) being very small, can be considered constant. A representation of the specific heat is more complicated, because of the release of the latent heat of fusion when the molten metal solidifies which will be dealt with in the next section. An illustration of the functional relationships for specific heat of low-carbon steel is shown in Fig. 4.3. The latent heat of fusion is accounted for, over the temperature range from the liquidus to the solidus. The area under the triangle is numerically equal to the latent heat of fusion.

Thus, any heat transfer analysis requires a pre-determined knowledge of the thermal properties of the materials involved. The required properties may be obtained by resorting to curve-fitting techniques with existing experimental data.

4.2.4 Latent Heat of Fusion

One feature which distinguishes the solidification problem from many other heat transfer problems is the release of latent heat of fusion during the phase change. For a steel casting, this is caused by the change in the free energy associated with the transformation of austenite to ferrite, resulting in the liberation of energy. Most engineering alloys solidify over a range of temperatures rather than at a discrete melting point. Thus, the latent heat of fusion is released over the range of temperatures from the liquidus to the solidus.

For the present modelling purposes, two methods are used to account for the latent heat of fusion. The first method has already been discussed briefly in the preceding section. In this method, the specific heat within the liquidus-solidus temperature range is artificially increased to simulate the evolution of latent heat. The latent heat of fusion is converted into the appropriate units for specific heat and added to the specific heat term over the liquidus-solidus temperature range, so that

$$C_p^* = C_p + \frac{H_f}{T_L - T_S} \qquad (4.12)$$

This is done so that the increased area under the specific heat versus temperature curve is equal to the latent heat of fusion as illustrated in Fig. 4.3. This method, known

as the modified specific heat method, is suitable for alloys which solidify over a relatively wide temperature range. It is essential that the calculated temperature of the region undergoing solidification should, at some time, fall within the liquidus-solidus range. In a situation where the temperatures are dropping quite rapidly, the choice of too big a time-step may cause the temperature to drop from above the liquidus to below the solidus over one time-step and prevent any release of latent heat. This method is not suited for pure metals, since the probability of the dropping of the temperature from above the melting point to below the melting point over one time-step is too large.

The second method used to account for the release of latent heat is the post-iterative method in which the temperatures are adjusted after each time-step. The latent heat of fusion is converted into an equivalent number of degrees by dividing the latent heat of fusion by the specific heat, i.e.,

$$DT = \frac{\text{Latent heat of fusion}}{\text{Specific heat}} \qquad (4.13)$$

After each time-step, whenever a calculated node temperature falls below the melting point, the difference between the predicted temperature and the melting temperature is noted.

If this difference is less than DT, the node temperature is reset to the melting temperature. This adjustment procedure is continued until the total accumulated difference for that particular node is equal to or greater than DT. At that time, the node temperature is allowed to fall in the normal manner. This procedure is particularly suitable for materials with one melting point.

4.3 NUMERICAL PROCEDURE FOR SOLVING HEAT FLOW EQUATION

4.3.1 Grid Design

The numerical solution consists of subdividing the structure into a series of small discrete elements. At the center of each element exists a node with the temperature representative for all points within that particular element. A typical grid network for a rectangular plane with symmetry at the centerline is shown in Fig. 4.4. Observe that certain grid lines are assumed to coincide with the centerline, metal and mold boundaries.

4.3.2 Finite Difference Approximation Using the Energy Balance Method

The finite difference equation describing the temperature of any particular node can be obtained by performing the heat balance over the element. The net gain or loss of heat between one element and all the surrounding elements goes into raising or lowering the temperature of the element

under consideration. The finite difference equations must be derived for each element of the entire set of nodal points, which in general consists of internal nodes, boundary nodes, and interface nodes.

4.3.2.1 Finite Difference Equation for an Internal Node

The finite difference equation for an internal point can be derived by considering a control volume around the node and applying the energy balance principle to this volume. A portion of a two-dimensional grid in the cartesian coordinate system is shown in Fig. 4.5 for a typical internal node (i,k). The control volume around node (i,k) is shown by dashed lines, and is equal to $(\Delta x_i . \Delta z_k)$. Its thickness in the third direction is assumed to be unity. The heat flux at the control volume face between (i-1,k) and (i,k) is obtained over the entire face area of $(\Delta z_k . 1)$. Heat flow through the other faces is obtained in a similar fashion. The net heat flow from the surrounding nodes during a small time interval Δt, causes a change in the temperature of the element. Thus, the finite difference equation for the two-dimensional system of Eqn. (4.1) is written as,

$$K_{i-1,i} \cdot \Delta z_k \frac{(T_{i-1,k}-T_{i,k})}{(\Delta x_{i-1}+\Delta x_i)/2} + K_{i,i+1} \cdot \Delta z_k \frac{(T_{i+1,k}-T_{i,k})}{(\Delta x_i+\Delta x_{i+1})/2}$$

$$+ K_{k-1,k} \cdot \Delta x_i \frac{(T_{i,k-1}-T_{i,k})}{(\Delta z_{k-1}+\Delta z_k)/2} + K_{k,k+1} \cdot \Delta x_i \frac{(T_{i,k+1}-T_{i,k})}{(\Delta z_k+\Delta z_{k+1})/2}$$

$$= \rho_{i,k} c_{i,k} \cdot \Delta x_i \Delta z_k \frac{(T^{n+1}_{i,k} - T^{n}_{i,k})}{\Delta t} \qquad (4.14)$$

where $\rho_{i,k}$ and $c_{i,k}$ are the density and specific heat of the element. Equation (4.14) can also be used for an unequal mesh grid, where Δx_i and Δz_k represent the size of the control volume as shown in Fig. 4.5. $K_{i-1,i}$ represents the value of the thermal conductivity pertaining to the control volume face between the adjacent nodes (i-1,k) and (i,k). The need for evaluating the interface conductivity arises from the fact that the thermal conductivity is temperature dependent and this can lead to a variation in the conductivity in response to the temperature distribution. The control volume surrounding the node (i,k) is considered to be filled with a material of uniform conductivity K_i evaluated at $T_{i,k}$, and the one surrounding node (i-1,k) with a conductivity K_{i-1} evaluated at $T_{i-1,k}$. $K_{i-1,i}$ is taken as the harmonic mean of K_i and K_{i-1}, i.e.

$$K_{i-1,i} = \left[\frac{1-f^{x}_{i-1,i}}{K_i} + \frac{f^{x}_{i-1,i}}{K_{i-1}}\right]^{-1} \qquad (4.15)$$

where $f^{x}_{i-1,i}$ is the interpolation factor which is a ratio defined in terms of the distances as shown,

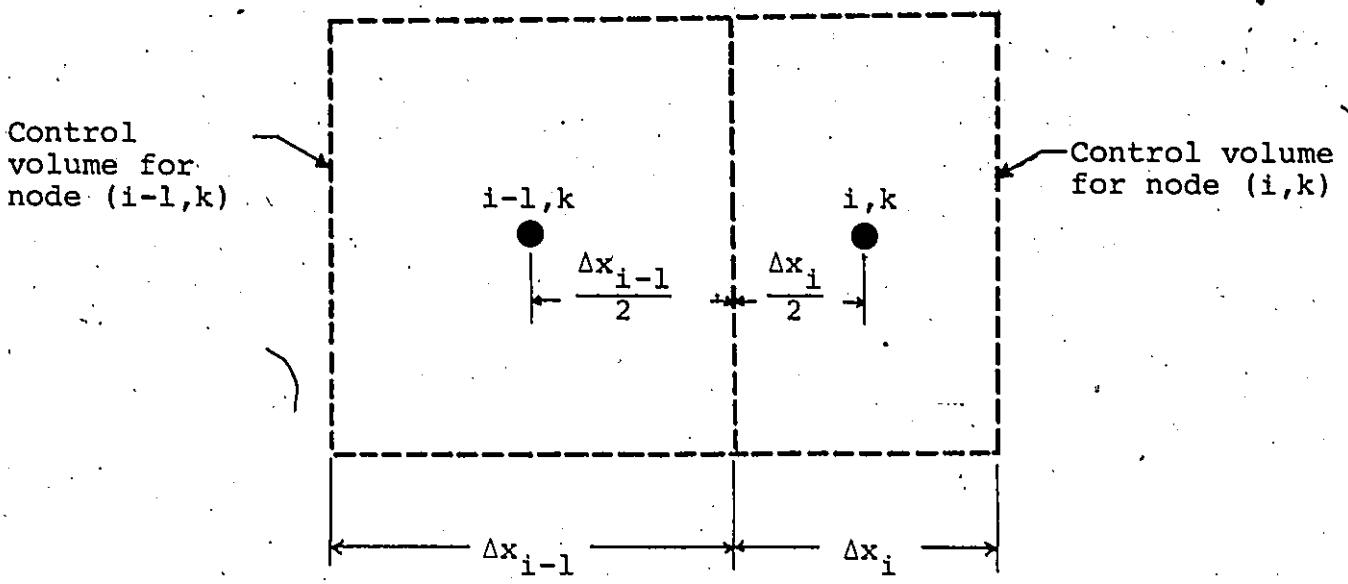

$$f^x_{i-1,i} \equiv \frac{\frac{\Delta x_i}{2}}{\left(\frac{\Delta x_{i-1}}{2} + \frac{\Delta x_i}{2}\right)} \tag{4.16}$$

Equation (4.14) is used for all internal points in the metal and the mold with their respective thermal properties.

The method being developed is not limited to cartesian grids but can be used for a grid in cylindrical coordinate system as given by Eqn. (4.2). To illustrate the derivation of the finite difference equation in the cylindrical system, consider a three-dimensional situation with coordinates r, ϕ, and z.

Using Fig. 4.6 for reference, and applying the energy balance for node (i,j,k), the expression for the finite difference approximation is written as:

$$K_{i-1,i}[(r_i-\xi\frac{\Delta r_i}{2})\Delta\phi_j\Delta z_k]\frac{(T_{i-1,j,k}-T_{i,j,k})}{(\Delta r_{i-1}+\Delta r_i)/2}$$

$$+ K_{i,i+1}[(r_i+\xi\frac{\Delta r_i}{2})\Delta\phi_j\Delta z_k]\frac{(T_{i+1,j,k}-T_{i,j,k})}{(\Delta r_i+\Delta r_{i+1})/2}$$

$$+ K_{j-1,j}[\Delta r_i\Delta z_k]\frac{(T_{i,j-1,k}-T_{i,j,k})}{r_i(\Delta\phi_{j-1}+\Delta\phi_j)/2}$$

$$+ K_{j,j+1}[\Delta r_i\Delta z_k]\frac{(T_{i,j+1,k}-T_{i,j,k})}{r_i(\Delta\phi_j+\Delta\phi_{j+1})/2}$$

$$+ K_{k-1,k}[r_i\Delta\phi_j\Delta r_i]\frac{(T_{i,j,k-1}-T_{i,j,k})}{(\Delta z_{k-1}+\Delta z_k)/2}$$

$$+ K_{k,k+1}[r_i\Delta\phi_j\Delta r_i]\frac{(T_{i,j,k+1}-T_{i,j,k})}{(\Delta z_k+\Delta z_{k+1})/2}$$

$$= \rho_{i,j,k}C_{i,j,k}[r_i\Delta\phi_j\Delta r_i\Delta z_k]\frac{(T^{n+1}_{i,j,k}-T^{n}_{i,j,k})}{\Delta t} \qquad (4.17)$$

Equation (4.17) can be conveniently converted to cartesian coordinate system by setting ξ and r_i equal to zero and unity respectively. Thus, the following derivations of the finite difference equations for the other nodes will be written in three-dimensional cylindrical coordinate system.

4.3.2.2 Finite Difference Equation for a Side Boundary Node

A sketch of the control volume surrounding a typical boundary node (i,j,k) at the side of the mold is depicted in Fig. 4.7. The control volume for node (i,j,k) is equal to $(\frac{\Delta r_i}{2} r_i \Delta\phi_j \Delta z_k)$. Provision is made for both convective and radiative heat flow from the boundary to the ambience at temperature, T_a. Applying an energy balance to the boundary node (i,j,k)

$$K_{i-1,i}[(r_i-\xi\frac{\Delta r_i}{2})\Delta\phi_j\Delta z_k]\frac{(T_{i-1,j,k}-T_{i,j,k})}{(\Delta r_{i-1}+\Delta r_i)/2}$$

$$+ h_s[r_i\Delta\phi_j\Delta z_k](T_a-T_{i,j,k})$$

$$+ K_{j-1,j}[\frac{\Delta r_i}{2}\Delta z_k]\frac{(T_{i,j-1,k}-T_{i,j,k})}{r_i(\Delta\phi_{j-1}+\Delta\phi_j)/2}$$

$$+ K_{j,j+1}[\frac{\Delta r_i}{2}\Delta z_k]\frac{(T_{i,j+1,k}-T_{i,j,k})}{r_i(\Delta\phi_j+\Delta\phi_{j+1})/2}$$

$$+ K_{k-1,k}[r_i\Delta\phi_j\frac{\Delta r_i}{2}]\frac{(T_{i,j,k-1}-T_{i,j,k})}{(\Delta z_{k-1}+\Delta z_k)/2}$$

$$+ K_{k,k+1}[r_i\Delta\phi_j\frac{\Delta r_i}{2}]\frac{(T_{i,j,k+1}-T_{i,j,k})}{(\Delta z_k+\Delta z_{k+1})/2}$$

$$= \rho_{i,j,k}C_{i,j,k}[\frac{\Delta r_i}{2}r_i\Delta\phi_j\Delta z_k]\frac{(T^{n+1}_{i,j,k}-T^n_{i,j,k})}{\Delta t} \qquad (4.18)$$

where h_s is the effective heat transfer coefficient accounting for both convective and radiative heat flow as defined in Eqn. (4.8). The finite difference equations for the top and bottom boundaries are derived similarly.

4.3.2.3 Finite Difference Equation for an Interface Node

Figure 4.8(a) shows a sketch of the region surrounding the interface node (i,j,k) between the metal and the mold, assuming perfect contact (before the formation of the air-gap). Performing an energy balance for node (i,j,k),

$$K^c_{i-1,i}\left[\left(r_i-\xi\frac{\Delta r_i}{2}\right)\Delta\phi_j\Delta z_k\right]\frac{(T_{i-1,j,k}-T_{i,j,k})}{(\Delta r_{i-1}+\Delta r_i)/2}$$

$$+ K^m_{i,i+1}\left[\left(r_i+\xi\frac{\Delta r_i}{2}\right)\Delta\phi_j\Delta z_k\right]\frac{(T_{i+1,j,k}-T_{i,j,k})}{(\Delta r_i+\Delta r_{i+1})/2}$$

$$+ [K^c_{j-1,j}+K^m_{j-1,j}]\left[\frac{\Delta r_i}{2}\Delta z_k\right]\frac{(T_{i,j-1,k}-T_{i,j,k})}{r_i(\Delta\phi_{j-1}+\Delta\phi_j)/2}$$

$$+ [K^c_{i,j+1}+K^m_{j,j+1}]\left[\frac{\Delta r_i}{2}\Delta z_k\right]\frac{(T_{i,j+1,k}-T_{i,j,k})}{r_i(\Delta\phi_j+\Delta\phi_{j+1})/2}$$

$$+ [K^c_{k-1,k}+K^m_{k-1,k}]\left[\frac{\Delta r_i}{2}\ r_i\Delta\phi_j\right]\frac{(T_{i,j,k-1}-T_{i,j,k})}{(\Delta z_{k-1}+\Delta z_k)/2}$$

$$+ [K^c_{k,k+1}+K^m_{k,k+1}]\left[\frac{\Delta r_i}{2}\ r_i\Delta\phi_j\right]\frac{(T_{i,j,k+1}-T_{i,j,k})}{(\Delta z_k+\Delta z_{k+1})/2}$$

$$= [\rho^c_{i,j,k}C^c_{i,j,k}+\rho^m_{i,j,k}C^m_{i,j,k}]\left[\frac{\Delta r_i}{2}r_i\Delta\phi_j\Delta z_k\right]\frac{(T^{n+1}_{i,j,k}-T^n_{i,j,k})}{\Delta t} \qquad (4.19)$$

The superscripts c and m indicate that the thermal properties are evaluated for the metal and the mold respectively. Note that the control volume is comprised of the metal and the mold. The right-hand side of Eqn. (4.19) is evaluated by considering separate contributions from each material.

After the formation of the air-gap, the metal and mold are no longer in perfect contact. The node (i,j,k) becomes a node on the inner surface of the mold as shown in Fig. 4.8(b). The derivation of the finite difference equation is handled in the same way as for the boundary points. Heat transfer is mainly by radiation across the air-gap as discussed in Section 4.2.2. The finite difference equation for node (i,j,k) becomes,

$$h_g[r_i\Delta\phi_j\Delta z_k](T_{i-1,j,k}-T_{i,j,k})$$

$$+ K^m_{i,i+1}[(r_i+\xi\frac{\Delta r_i}{2})\Delta\phi_j\Delta z_k]\frac{(T_{i+1,j,k}-T_{i,j,k})}{(\Delta r_i+\Delta r_{i+1})/2}$$

$$+ K^m_{j-1,j}[\frac{\Delta r_i}{2}\Delta z_k]\frac{(T_{i,j-1,k}-T_{i,j,k})}{r_i(\Delta\phi_{j-1}+\Delta\phi_j)/2}$$

$$+ K^m_{j,j+1}[\frac{\Delta r_i}{2}\Delta z_k]\frac{(T_{i,j+1,k}-T_{i,j,k})}{r_i(\Delta\phi_j+\Delta\phi_{j+1})/2}$$

$$+ K^m_{k-1,k}[\frac{\Delta r_i}{2}r_i\Delta\phi_j]\frac{(T_{i,j,k-1}-T_{i,j,k})}{(\Delta z_{k-1}+\Delta z_k)/2}$$

$$+ K^{m}_{k,k+1}\left[\frac{\Delta r_i}{2} r_i \Delta\phi_j\right]\frac{(T_{i,j,k+1}-T_{i,j,k})}{(\Delta z_k+\Delta z_{k+1})/2}$$

$$= \rho^{m}_{i,j,k} C^{m}_{i,j,k}\left[\frac{\Delta r_i}{2} r_i \Delta\phi_j \Delta z_k\right]\frac{(T^{n+1}_{i,j,k}-T^{n}_{i,j,k})}{\Delta t} \qquad (4.20)$$

where h_g is the effective heat transfer coefficient for the air-gap calculated as defined in Eqn. (4.11).

4.3.2.4 Finite Difference Equations for Other Nodes

The general procedure for deriving the finite difference equations for the other typical nodes is similar to the general treatment already discussed in the preceding sections. The details are listed in Appendix B.

Figure 4.9 illustrates the node numbers of typical nodes in the grid network ranging from 1-17. The node numbers identify the type of node and the finite difference equation to use. As an example, the node number "1" indicates an internal point and the heat balance is taken as in Eqn. (4.14) with the thermal properties evaluated for the material involved. The node numbers facilitate the channelling of subsequent calls to the appropriate finite difference equation for each nodal point to be used in the computer program.

4.3.3 Outline of the Alternating Direction Implicit (ADI) Method

By means of successive application of the energy balance at all nodes in the metal and mold, a series of

algebraic equations has been derived which can be solved explicitly or implicitly to obtain the temperature distribution in the system at subsequent time elapses.

The explicit finite difference method is formulated in terms of the known values and the solution is relatively straight forward. However, the explicit technique is restricted by the time-step and mesh size to generate a stable solution as observed in the previous chapter. Accuracy and convergence of the method increases as the time-step and size of the element is decreased. For solidification in a sand mold, for example, the process may take hours, and an accurate solution may be very expensive in computer time.

The implicit method for the solution of the finite difference equations may overcome the time-step restriction for stability. The equations are expressed in terms of the temperatures that are yet to be computed. The application of the finite difference equations to all nodes in the system can generate a series of simultaneous equations which is solved to obtain the new temperature field. Unfortunately, the implicit scheme requires a solution of a system of simultaneous equations which can also be very expensive in terms of computer costs.

To overcome these problems, Peaceman and Rachford [3] developed the alternating direction implicit (ADI) method

which is stable for all time-steps and requires merely the solution of several sets of tridiagonal equations for each time-step advancement. For a typical two-dimensional problem with a rectangular region, it involved many times less computational work than the explicit or implicit technique. In the ADI scheme, the operation is done in two successive half time-steps, each of duration $\Delta t/2$.

Over the first half time-step, the finite difference equations are expressed implicitly in the x-direction and explicitly in the z-direction. In the successive second half time-step, the procedure is reversed, that is, the equations are made explicit in the x-direction and implicit in the z-direction. Over the two successive half time-steps, the approximations by the ADI method to Eqn. (4.14) are:

$$\rho_{i,k}C_{i,k}\Delta x_i \Delta z_k \frac{(T^{n+\frac{1}{2}}_{i,k}-T^{n}_{i,k})}{\Delta t/2}$$

$$= K_{i-1,i}\Delta z_k \frac{(T^{n+\frac{1}{2}}_{i-1,k}-T^{n+\frac{1}{2}}_{i,k})}{(\Delta x_{i-1}+\Delta x_i)/2}$$

$$+ K_{i,i+1}\Delta z_k \frac{(T^{n+\frac{1}{2}}_{i+1,k}-T^{n+\frac{1}{2}}_{i,k})}{(\Delta x_i+\Delta x_{i+1})/2}$$

$$+ K_{k-1,k}\Delta x_i \frac{(T^{n}_{i,k-1}-T^{n}_{i,k})}{(\Delta z_{k-1}+\Delta z_k)/2}$$

$$+ K_{k,k+1}\Delta x_i \frac{(T^{n}_{i,k+1}-T^{n}_{i,k})}{(\Delta z_k+\Delta z_{k+1})/2} \qquad (4.21)$$

and

$$\rho_{i,k}C_{i,k}\Delta x_i \Delta z_k \frac{(T^{n+1}_{i,k}-T^{n+\frac{1}{2}}_{i,k})}{\Delta t/2}$$

$$= K_{i-1,i}\Delta z_k \frac{(T^{n+\frac{1}{2}}_{i-1,k}-T^{n+\frac{1}{2}}_{i,k})}{(\Delta x_{i-1}+\Delta x_i)/2}$$

$$+ K_{i,i+1}\Delta z_k \frac{(T^{n+\frac{1}{2}}_{i+1,k}-T^{n+\frac{1}{2}}_{i,k})}{(\Delta x_i+\Delta x_{i+1})/2}$$

$$+ K_{k-1,k}\Delta x_i \frac{(T^{n+1}_{i,k-1}-T^{n+1}_{i,k})}{(\Delta z_{k-1}+\Delta z_k)/2}$$

$$+ K_{k,k+1}\Delta x_i \frac{(T^{n+1}_{i,k+1}-T^{n+1}_{i,k})}{(\Delta z_k+\Delta z_{k+1})/2} \qquad (4.22)$$

In Eqn. (4.21), over the first half time-step, the $T^{n+\frac{1}{2}}$ are unknown and T^n are known from the previous time-step or initial conditions. Over the second half time-step, the $T^{n+\frac{1}{2}}$ in Eqn. (4.22) are now known and the T^{n+1} are unknown. Hence, the successive applications of Eqn. (4.21) followed by Eqn. (4.22) give the new temperature field after an elapse of time Δt. This alternation of directions to represent explicitly or implicitly is necessary in order to ensure stability of the computations. Unilateral repetition results in an unstable solution.

Equations (4.21) and (4.22) both contain only three unknowns each. Essentially, by considering a whole row or

column of points at once, a system of simultaneous equations for the whole row or column of unknown temperatures is generated. Each equation contains exactly three unknowns except the first and the last equation which contain two unknowns, since the boundary conditions are known or specified as discussed in Section 4.2.2. This results in a set of equations with tridiagonal coefficients as follows:

$$\begin{aligned}
d_1T_1 + a_1T_2 &= C_1 \\
b_2T_1 + d_2T_2 + a_2T_3 &= C_2 \\
b_3T_2 + d_3T_3 + a_3T_4 &= C_3 \\
b_4T_3 + d_4T_4 + a_4T_5 &= C_4 \\
&\vdots \\
b_mT_{m-1} + d_mT_m &= C_m
\end{aligned} \qquad (4.23)$$

This system of tridiagonal equations can be solved quite readily by the TriDiagonal Matrix Algorithm (TDMA) [73].

The ADI method for a two-dimensional situation can be visualized with reference to Fig. 4.10. The equations for the grid points along the chosen row contain the unknown temperatures of the chosen row and the temperatures of the two neighbouring rows which are known from the previous time-step. Thus, the equations for the chosen line are

simply tridiagonal equations which are solved by the TDMA. This procedure is repeated for all rows and followed by a similar treatment for the columns for each time-step.

This technique can also be applied to problems of three-dimensional nature. As in the two-dimensional situation, one dimension is expressed implicitly while leaving the other dimensions explicit. Thus, the whole operation is carried out in three successive time-steps of duration $\Delta t/3$. Writing Eqn. (4.17) for the successive time-steps:

$$\rho_{i,j,k}C_{i,j,k}[r_i\Delta\phi_j\Delta r_i\Delta z_k]\frac{(T^{n+1/3}_{i,j,k}-T^{n}_{i,j,k})}{\Delta t/3}$$

$$= K_{i-1,i}[(r_i-\xi\frac{\Delta r_i}{2})\Delta\phi_j\Delta z_k]\frac{(T^{n+1/3}_{i-1,j,k}-T^{n+1/3}_{i,j,k})}{(\Delta r_{i-1}+\Delta r_i)/2}$$

$$+ K_{i,i+1}[(r_i+\xi\frac{\Delta r_i}{2})\Delta\phi_j\Delta z_k]\frac{(T^{n+1/3}_{i+1,j,k}-T^{n+1/3}_{i,j,k})}{(\Delta r_i+\Delta r_{i+1})/2}$$

$$+ K_{j-1,j}[\Delta r_i\Delta z_k]\frac{(T^{n}_{i,j-1,k}-T^{n}_{i,j,k})}{r_i(\Delta\phi_{j-1}+\Delta\phi_j)/2}$$

$$+ K_{j,j+1}[\Delta r_i\Delta z_k]\frac{(T^{n}_{i,j+1,k}-T^{n}_{i,j,k})}{r_i(\Delta\phi_j+\Delta\phi_{j+1})/2}$$

$$+ K_{k-1,k}[r_i\Delta\phi_j\Delta r_i]\frac{(T^{n}_{i,j,k-1}-T^{n}_{i,j,k})}{(\Delta z_{k-1}+\Delta z_k)/2}$$

$$+ K_{k,k+1}[r_i\Delta\phi_j\Delta r_i]\frac{(T^{n}_{i,j,k+1}-T^{n}_{i,j,k})}{(\Delta z_k+\Delta z_{k+1})/2} \qquad (4.24)$$

$$\rho_{i,j,k}C_{i,j,k}[r_i\Delta\phi_j\Delta r_i\Delta z_k]\frac{(T^{n+2/3}_{i,j,k}-T^{n+1/3}_{i,j,k})}{\Delta t/3}$$

$$= K_{i-1,i}[(r_i-\xi\frac{\Delta r_i}{2})\Delta\phi_j\Delta z_k]\frac{(T^{n+1/3}_{i-1,j,k}-T^{n+1/3}_{i,j,k})}{(\Delta r_{i-1}+\Delta r_i)/2}$$

$$+ K_{i,i+1}[(r_i+\xi\frac{\Delta r_i}{2})\Delta\phi_j\Delta z_k]\frac{(T^{n+1/3}_{i+1,j,k}-T^{n+1/3}_{i,j,k})}{(\Delta r_i+\Delta r_{i+1})/2}$$

$$+ K_{j-1,j}[\Delta r_i\Delta z_k]\frac{(T^{n+2/3}_{i,j-1,k}-T^{n+2/3}_{i,j,k})}{r_i(\Delta\phi_{j-1}+\Delta\phi_j)/2}$$

$$+ K_{j,j+1}[\Delta r_i\Delta z_k]\frac{(T^{n+2/3}_{i,j+1,k}-T^{n+2/3}_{i,j,k})}{r_i(\Delta\phi_j+\Delta\phi_{j+1})/2}$$

$$+ K_{k-1,k}[r_i\Delta\phi_j\Delta r_i]\frac{(T^{n+1/3}_{i,j,k-1}-T^{n+1/3}_{i,j,k})}{(\Delta z_{k-1}+\Delta z_k)/2}$$

$$+ K_{k,k+1}[r_i\Delta\phi_j\Delta r_i]\frac{(T^{n+1/3}_{i,j,k+1}-T^{n+1/3}_{i,j,k})}{(\Delta z_k+\Delta z_{k+1})/2} \qquad (4.25)$$

and

$$\rho_{i,j,k}C_{i,j,k}[r_i\Delta\phi_j\Delta r_i\Delta z_k]\frac{(T^{n+1}_{i,j,k}-T^{n+2/3}_{i,j,k})}{\Delta t/3}$$

$$= K_{i-1,i}[(r_i-\xi\frac{\Delta r_i}{2})\Delta\phi_j\Delta z_k]\frac{(T^{n+2/3}_{i-1,j,k}-T^{n+2/3}_{i,j,k})}{(\Delta r_{i-1}+\Delta r_i)/2}$$

$$+ K_{i,i+1}[(r_i+\xi\frac{\Delta r_i}{2})\Delta\phi_j\Delta z_k]\frac{(T^{n+2/3}_{i+1,j,k}-T^{n+2/3}_{i,j,k})}{(\Delta r_i+\Delta r_{i+1})/2}$$

$$+ K_{j-1,j}[\Delta r_i\Delta z_k]\frac{(T^{n+2/3}_{i,j-1,k}-T^{n+2/3}_{i,j,k})}{r_i(\Delta\phi_{j-1}+\Delta\phi_j)/2}$$

$$+ K_{j,j+1}[\Delta r_i \Delta z_k]\frac{(T^{n+2/3}_{i,j+1,k} - T^{n+2/3}_{i,j,k})}{r_i(\Delta\phi_j + \Delta\phi_{j+1})/2}$$

$$+ K_{k-1,k}[r_i \Delta\phi_j \Delta r_i]\frac{(T^{n+1}_{i,j,k-1} - T^{n+1}_{i,j,k})}{(\Delta z_{k-1} + \Delta z_k)/2}$$

$$+ K_{k,k+1}[r_i \Delta\phi_j \Delta r_i]\frac{(T^{n+1}_{i,j,k+1} - T^{n+1}_{i,j,k})}{(\Delta z_k + \Delta z_{k+1})/2} \qquad (4.26)$$

Each of the equations from (4.24) to (4.26) generates a tridiagonal system in one space dimension which is solved quite readily with the TDMA as in the two-dimensional situation. This is done for the whole system and the intermediate values $T^{n+1/3}$ and $T^{n+2/3}$ are used to compute the temperatures in the next dimension. Successive applications and solution of Eqn. (4.24) followed by Eqn. (4.25) and (4.26) will give the new temperature distribution after a time-step, Δt.

For two-dimensional, rectangular problems, the ADI scheme is unconditionally stable and allows the use of time-steps of any size without requiring a large amount of computer time to attain the solution. Under more general conditions and for three-dimensional situations, this scheme may not possess the same degree of superiority over alternative methods as it does with the two-dimensional problems. For the present model, the ADI method was adopted both for a two-dimensional, rectangular problem and a three-dimensional, cylindrical problem.

4.3.4 Summary of the Computer Program

A computer program was developed to deal with two- or three-dimensional solidification problems in cartesian or cylindrical coordinates using the alternating direction implicit (ADI) numerical technique.

An overall flow chart of the three-dimensional program is shown in Fig. 4.11. The program starts by reading the input data and computing some preliminary variables. The initial conditions of the temperature for the metal and mold are also specified at this stage. A call is then made on the subroutine NODAL, which identifies the type of node for each one of the grid points as shown in Fig. 4.9. This facilitates the channelling of the appropriate finite difference equations to the corresponding grid points.

The rest of the program is concerned with implementing the ADI method over successive time-steps. Over the first third time-step, the line iterations are performed for the radial direction. Subroutine LINEX determines the set of tridiagonal coefficients for each node along the chosen row, identified earlier by subroutine NODAL. The thermal properties are determined by using functions RO, SH, and COND to calculate the values of the density, specific heat, and conductivity corresponding to the temperature and material at the different grid points. Latent heat of fusion is accounted for in the specific heat correlations

or by the post-iterative method discussed in earlier sections. Subroutine TRID is then called to solve the tridiagonal system of simultaneous equations using TDMA. This process is repeated until all the rows in the system have been completed.

Over the next third of the time-step, subroutine LINEY is called to solve the tridiagonal system in the tangential direction using the newly computed temperatures from LINEX. Finally, to complete a whole time-step, subroutine LINEZ is called to solve the tridiagonal system in the axial direction with the new temperatures from LINEY. Subroutine UPDATE is called to update the temperature field in the system and the time is advanced by Δt. At suitable intervals, subroutines PRINT and PLOT are called to print and plot the computed results. The same procedure is repeated over successive time-steps until the time exceeds a pre-assigned upper limit TSTOP, at which point, computations are discontinued.

The program developed for three-dimensional, cylindrical problems can be readily modified to accommodate two-dimensional or cartesian systems.

4.4 RESULTS AND DISCUSSIONS

During the development of the program, several sample problems were devised for testing. The program was initially used for the solution of a simple two-dimensional

solidification problem defined by the cartesian coordinate system. It was then extended to calculate heat transfer during solidification in a cylindrical mold using the three-dimensional program. The reliability of the model is demonstrated by comparing the computed results with literatures.

4.4.1 Application to a Two-Dimensional, Rectangular Solidification Problem

The mold is assumed infinitely wide and the vertical faces at the side of the mold are exposed to similar heat flow conditions. Thus the problem is two-dimensional with symmetry about its center. An illustration of the two-dimensional vertical plane is shown in Fig. 4.12 with the finite difference grid and the boundary conditions.

It was assumed that initially, at time = 0, the entire mold was filled with liquid metal at pouring temperature 1563°C, and no convective transport in the liquid phase was considered. The mold temperature was taken to be uniform at 121°C before computation. Perfect contact was assumed between the ingot and the mold before the formation of the air-gap. The air-gap of finite thickness formed instantaneously after a time elapse of 2 minutes. The ingot was assumed to be resting its weight on the mold. The bottom interface between the ingot and mold was thus assumed to remain in perfect contact during the whole process. Heat

transfer across the gap was mainly by radiation and conduction due to some contact points. An equivalent heat transfer coefficient was calculated as discussed in Section 4.2.2. Heat was lost to the ambience at 23.8°C through the side and bottom outer surface of the mold. Heat losses at these surfaces were mainly by radiation and convection. The effective heat transfer coefficients for the boundaries were computed, based on the boundary temperatures as discussed. An adiabatic condition was assumed for the top boundary.

Linear correlations such as those illustrated in Figs. 4.1 and 4.3 were used for the thermal conductivity and specific heat of the ingot and mold. The quantitative expressions used to describe the material properties in this simulation are summarized in Table 4.1. Densities vary only with different materials or different phases of the material and were assumed to be constant over the temperature range. The release of latent heat of fusion was accounted for by the specific heat curve.

The shape of the ingot and mold suggests that a rectangular mesh is to be used. Unequal mesh size was used for regions near the air-gap and interface. A total of 960 grid points were used, with 20 nodes in the x-direction and 48 nodes in the z-direction.

The finite difference equations and numerical scheme presented in the preceding sections were used to compute the

Table 4.1. Input data for solidification program.

Thermal properties of low carbon steel

Density: liquid = 7200.0 kg/m^3
solid = 7480.6 kg/m^3

Liquidus temperature: 1498.8 °C (2730.0°F)

Solidus temperature: 1448.8 °C (2640.0°F)

Latent heat of fusion: 272.1 kJ/kg

Thermal conductivity (from Fig. 4.1)

0° to 1640°F,	K = 28.58-0.00722.(T - 100.0)
1640° to 2640°F,	K = 17.3 + 0.0012 (T - 1640.0)
2640° to 2730°F,	K = 18.5 - 0.0389 (T - 2640.0)
>2730°F,	K is constant at 15.0

(T is in °F and K in BTU/hr - ft - °F)

To convert K to S.I. units, multiply by 1.7307.

Specific heat (from Fig. 4.3)

0° to 800°F,	C_p = 0.118 + 0.00005 (T - 200.0)
800° to 1300°F,	C_p = 0.148 + 0.000148 (T - 800.0)
1300° to 1800°F,	C_p = 0.222 - 0.000108 (T - 1300.0)
1800° to 2640°F,	C_p = 0.168 + 0.0000381 (T - 1800.0)
2640° to 2685°F,	C_p = 0.20 + 0.0579 (T - 2640.0)
2685° to 2730°F,	C_p = 2.805 - 0.0576 (T - 2685.0)
>2730°F,	C_p is constant at 0.21

(T is in °F and C_p in BTU/lb-°F).

To convert C_p to S.I. units, multiply by 4186.9.

Pouring temperature: 1563.0°C (2845°F)

Mold temperature: 121°C (250°F)

Ambient temperature: 23.8°C (75°F)

Dimensions of ingot and mold: see Fig. 4.12

temperature distributions in the ingot and mold during the process. A time-step of 10 seconds was used in the computation. The program was allowed to run for 130 minutes of simulated time. The temperature for each grid point was printed at different time intervals. A sample output from the program is shown in Fig. 4.13. From these results, the temperature and solidification front profiles were plotted and analyzed.

The nature of the solidification pattern is illustrated in Fig. 4.14. The location of the solidification front is depicted for different time intervals. Solidification starts from the metal/mold interface and proceeds towards the center of the ingot. The nature of the curves is similar to that obtained by Raychaudhuri [51]. Initially, in the absence of interface resistance before the formation of the air-gap, the solidification rate is quite rapid and decreases as the mold becomes heated.

Figure 4.15 gives the result of a plot of the progress of the liquidus and solidus isotherms with the square root of time. Both the liquidus and solidus isotherms move linearly with the square root of the time. The velocity of the isotherms begins to increase as they approach the center of the ingot. Similar kinds of results were obtained by Campagna [74] for unidirectional solidification of an Al-4.5% Cu alloy. The vertical distance between the liquidus

and solidus curves represents the width of the "mushy" zone in the ingot at a given time during solidification. The "mushy" zone is the region in the ingot over which the solid and liquid phase of the metal coexist. Casting characteristics are strongly influenced by the width of this zone. The horizontal distance between the two curves gives the time taken for the temperature of a point in the ingot to drop from the liquidus temperature to the solidus temperature. The total time taken for the whole ingot to solidify is about 125 minutes. The solidification rate and thus the solidification time were also found to be dependent on the initial metal and mold temperature.

Flemings [75] gave an expression obtained by investigators from experimental results for steel solidification against cast-iron mold walls, which is of the form:

$$x = a\sqrt{t} - b \qquad (4.27)$$

where the constant a is approximately unity and the constant b is 0.5 when the units are in inches and minutes respectively. The dashed line in Fig. 4.15 shows the plot of this expression. There is reasonable agreement between the two results except that the experimental curve is displaced slightly on the time axis.

In Fig. 4.16, the temperature profiles in the ingot are illustrated for (a) time = 10 minutes and (b) time = 40 minutes after pouring. Heat losses from the ingot to

the mold are quite uniform in the transverse direction. A comparison of the two temperature distributions shows that initially, most parts of the ingot around the center core are not very much affected by the heat losses to the mold. Most of these regions are still in its molten form and the temperature distributions are only slightly below the pouring temperature. The solidified parts of the ingot loses heat quickly to the relatively cold mold as indicated by the crowding of the isotherms. As time progresses, more metal in the ingot solidifies and the mold gained more heat from the ingot, the isotherms are spread more evenly.

Figure 4.17 shows the temperature profiles in the mold for the same time intervals as Fig. 4.16. The isotherms at time = 10 minutes are generally at a lower temperature. The mold appears to be gaining more heat from the ingot than losing heat to the ambience. At time = 40 minutes, the isotherms are at a higher temperature range since the mold at this time is heated up from the heat gained from the ingot. Information on the temperature distribution in the mold would be useful for designing molds and also for optimizing the cooling time for the mold before it is used again.

4.4.2 Application to Solidification Problem in Three-Dimensional, Cylindrical System

Similar computations were performed for the solidification of an ingot in a cylindrical mold. This is not a three-dimensional problem but the three-dimensional program was used in order to test the model. The thermal properties and boundary conditions were similar to those for the rectangular mold (Table 4.1). A cylindrical mesh was used with 20 nodes in the radial direction and 48 nodes in the axial direction and 8 nodes in the tangential direction. Using the finite difference equations described in Section 4.3.2 and Appendix B, the temperature distributions in the ingot and mold were computed as before. Some selected results are presented and discussed.

Heat transfer during the solidification is axisymmetrical about its central axis. The advancement of the solidification front in the ingot for one of the vertical plane is shown in Fig. 4.18. The nature of the solidification pattern is similar to Fig. 4.14 for a rectangular ingot. A plot of the liquidus and solidus isotherms with the square root of time is presented in Fig. 4.19. The results for a two-dimensional computation of the cylindrical mold are also plotted in Fig. 4.19. Both the two- and three-dimensional computations agree very well.

The solidification time for the cylindrical ingot was found to be about 65 minutes. Since the geometry of the

heat flow into a concave mold wall will be divergent, the heat flow will be slightly more rapid than into a plane mold wall. Thus, a shorter solidification time is expected for the cylindrical ingot than for a rectangular ingot of the same size. This can also be explained from Chvorinov's rule which states that the total solidification time is proportional to the square of the volume-to-area ratio of the castings or,

$$t_s = C\left(\frac{\text{Volume}}{\text{Area}}\right)^2 \qquad (4.28)$$

where C is a constant for a given metal-mold material and mold temperature. The area in Eqn. (4.28) is the area of the metal/mold interface. This equation is used for comparing solidification times of simple-shaped castings.

The temperature distributions in the cylindrical ingot and mold at time = 10 minutes and time = 40 minutes after pouring are displayed in Figs. 4.20 and 4.21. Figure 4.22 presents the temperature gradients in the ingot and mold at different heights for time = 10 minutes. A study of this figure and the preceding two figures confirmed the observation of high heat flow in the solidified region as indicated by the steep temperature gradient. Note the temperature discontinuity at the ingot/mold interface because of the air-gap. At a lower plane, in the mold, there is no discontinuity. Figure 4.23 illustrates similar results for

time = 40 minutes. In the mold, the temperatures increased while that in the ingot decreased as observed earlier. Because of this, the temperature drop across the interface decreased.

The cooling curves at the center of the ingot are shown in Fig. 4.24. The temperature at the center core is plotted against time at different heights of the ingot. Since the top boundary is adiabatic, heat losses for regions near the top are very slow. The temperature near the bottom of the ingot dropped quite significantly over the first 10 minutes and then levelled off. Analyzing this figure with Fig. 4.18, one notices that the drop in the temperature is more significant after the metal surrounding the node point has solidified.

It is interesting also to look at the temperature-time variation in the ingot and mold at a height 66.7 cm from the top. This is presented in Fig. 4.25. Lines "1" and "2" show the typical cooling curves in the ingot similar to those discussed in Fig. 4.24. The temperature variation at the outer surface of the ingot is represented by line "3". The effect of the air-gap is quite clear in the figure. Before the formation of the gap, the temperature dropped rapidly from its pouring temperature since perfect contact was assumed. At time = 2 minutes, as observed by Raychaudhuri [51], the temperature rises again because of considerable

resistance to the heat flow caused by the gap. As time progresses, more heat is lost from the ingot and the temperature falls again. The temperature variation at the inner surface of the mold is also interesting. This node, before the gap formation is the interface mode, and the temperature at time = 0 computed from Eqn. (4.9) is initially 826°C. The temperature rises slightly and drops after the gap is formed. It rises slightly again when heat gained by the mold is greater than heat lost to the ambience before it begins to drop. Lines "5" and "6" show the temperature variation at the middle and outer surface of the mold. Initially, there is a slight drop at the outer surface because heat is lost to the ambience. But heat gained from the ingot is much greater and the temperature rises up to a maximum before it starts to cool down.

The effective heat transfer coefficients for the boundaries are computed based on the temperature at the boundary nodes. Figures 4.26 and 4.27 illustrate the computed heat transfer coefficients for the side and bottom boundaries. Both figures display similar patterns. The effective heat transfer coefficient increases with time to a maximum as the temperature of the surface node rises (see line "6" in Fig. 4.25). The nodes with higher temperature appear to have a higher heat transfer coefficient.

The heat flow during solidification is controlled to quite an extent by the resistance at the metal/mold interface. The effect of the metal/mold interface can be seen by the temperature drop across the interface or air-gap in Figs. 4.22 and 4.23. An effective heat transfer coefficient is calculated based on the temperature across the gap to account for this resistance. The interface heat transfer coefficient is strongly dependent on the temperature. A plot of the variation of the interface or gap heat transfer coefficient is presented in Fig. 4.28.

The modelling of the solidification process using the present approach has proved to be quite promising. The obtained results and observed trends are in good agreement with results from the literature. By varying the mold thickness, size or initial temperature, or varying the size and shape of the cast, or by using different materials with different thermal properties, this model can be used to analyze and obtain information which may be difficult or not possible to obtain in the actual process. Information from these results can be used to improve the qualitative understanding of the influence of the various parameters in the solidification process and which, in turn, can be used for process control and design.

CHAPTER V

CONCLUSION

5.1 SUMMARY OF PRESENT INVESTIGATIONS

The simulation of a process is a mathematical representation in terms of the pertinent variables of that process. The preceding two chapters have demonstrated two different mathematical models for simulating the ladle and casting process in steelmaking operations. Based on the results and observations described in Chapters III and IV, the following summaries and recommendations are made.

5.1.1 Ladle Processing Simulation

The MAC technique is devised to handle the calculation of the recirculatory flows caused by the local introduction of a gas jet. The predicted flow patterns compare reliably with existing axisymmetric computations. The use of equation (3.7) for estimating the effective viscosity in the system provides a relatively simpler model to predict the flow fields with reasonable agreement with other models.

Quantitative comparisons have been made between the predicted velocity fields for the conical and cylindrical jet. The conical jet model predicts relatively higher velocities in the gas-liquid mixture near the axis of the vessel. As the size of the two-phase gas-liquid plume is

varied, considerable variation of the predicted flow field is observed in the region close to the axis of the vessel ($r_c/R < 0.3$). In most parts of the flow domain ($r_c/R > 0.3$), the variation of the velocity field is less significant.

The three-dimensional flow fields are also illustrated for off-centered jets at various positions in the vessel. The results are in agreement with the predicted flow patterns by Wong [69] using the k-ε model.

Finally, the stirring of an initially, stagnant, thermally stratified liquid exhibits the destruction of the temperature stratification and uniform temperature distribution is achieved at steady-state.

Through all these, the program encountered considerable stability problems which seem to be inherent in transient flow computations. The time and space steps have to satisfy the stability criteria. However, considerable improvements are obtained in the present model by using variable relaxation factor and optimizing the upwind differencing coefficient during the computations. Unfortunately, the time step required is relatively small, thus, the number of calculations required to reach a particular time and the computational costs are relatively high. The model has the advantage of having the ability to simulate the transient stages of the whole process but with higher computation costs. This is especially so when dealing with three-

dimensional problems. Any future development for the present model should consider improving on this area.

The model developed here has shown clearly the important role that fluid flow phenomena plays in ladle processing. Further efforts can be directed at applying the model to specific industrial situations with the goal of integrating the understanding of the fluid flow phenomena with the process kinetics associated with it.

5.1.2 Solidification Simulation

The present model is developed to handle solidification of ingots with simple geometry and varying thermal properties, including the release of latent heat and the formation of the air-gap. Using the ADI method, the solution of the finite difference equations is obtained quite readily. On the basis of some simplifying assumptions, the program is initially tested for two-dimensional solidification in a rectangular mold.

Predicted results indicate that significant amount of heat is lost from the ingot during the early stages before the air-gap is formed. As the solidification progresses, the solidification front advances towards the center. Progresses of the liquidus and solidus isotherms with time and temperature distributions in the ingot and mold at different time intervals are illustrated. There is reasonable agreement with results from existing works.

A run of the three-dimensional program is performed for a cylindrical ingot in order to test the three-dimensional code. Results show similar solidification patterns. The cylindrical ingot has a shorter solidification time due to its geometry. The cooling curves at different points in the ingot and mold are presented and analyzed. The heat gained by the mold from the ingot appears to be greater than the heat lost to the ambience during the solidification. The variation of the effective heat transfer coefficients has been found to be strongly dependent on the temperature. This is a promising approach to approximate the heat transfer coefficients which are difficult to measure in the actual solidification process.

The present code using the ADI method is quite efficient for the simple geometries considered. This method allows the use of time-steps of any size without any instability as encountered in the explicit finite difference technique. However, it is not correct to say that there is no restriction on the size of the time-step. The present treatment of the release of latent heat during freezing requires some special attention. If the specific heat of a region undergoing solidification is to be increased at the appropriate time, the calculated temperature of that region should, at some time, fall within the liquidus-solidus temperature range. If the time-step is too big, the

temperature may drop from above the liquidus to below the solidus over one time-step. Hence, the release of latent heat is not accounted for. To overcome this difficulty, an arbitrary restriction has to be imposed upon the size of the time-step. However, once the ingot is completely solidified, a larger time-step can be used for further computations.

The development and testing of the code is still continuing. For a more complete model, the present code should be tested for three-dimensional solidification. The model assumes straight walls for the ingot and mold with simple geometries. Tapered walls and molds with more complex shapes can be incorporated with some modifications. Another area where further work could be done is the simulation of the stripping of the ingot from the mold and the cooling of the mold. Further testings and comparison with experimental works at EMR will be carried out.

5.2 CONCLUDING REMARKS

No model is ever a perfect fit to reality and numerical simulation can never replace physical experimentation or theoretical analysis completely. However, numerical simulation has the advantage of having complete control over the choice of parameters and properties involved in the process. The sensitivity of the phenomena can be tested by varying these parameters to obtain informations relevant

for understanding the process. This is illustrated by the two models that are presented. Each of the models at its present stage generates its own specific requirements and method of solution to simulate each specific process. With some modifications, the models can be extended to simulate other related problems with gratifying results.

APPENDIX A

FINITE DIFFERENCE EXPRESSIONS FOR THE CONVECTIVE AND VISCOUS TERMS IN EQUATIONS (3.20) AND (3.21)

Using the approach discussed in Section 3.3.2, the convective and viscous terms in the tangential and axial momentum equations are derived with the same notations. From equation (3.20)

$$CVX = \frac{\partial \rho uv}{\partial r}$$

$$= \frac{1}{\Delta r_i} [\bar{U}_{i+\frac{1}{2},j+\frac{1}{2},k} \bar{V}_{i+\frac{1}{2},j+\frac{1}{2},k} \bar{\rho}_{i+\frac{1}{2},j+\frac{1}{2},k}$$

$$- \bar{U}_{i-\frac{1}{2},j+\frac{1}{2},k} \bar{V}_{i-\frac{1}{2},j+\frac{1}{2},k} \bar{\rho}_{i-\frac{1}{2},j+\frac{1}{2},k}] \qquad (A.1)$$

$$CVY = \frac{1}{r} \frac{\partial \rho v^2}{\partial \phi}$$

$$= \frac{(\bar{V}_{i,j+1,k})^2 \rho_{i,j+1,k} - (\bar{V}_{i,j,k})^2 \rho_{i,j,k}}{r_i \Delta \phi} \qquad (A.2)$$

$$CVZ = \frac{\partial \rho vw}{\partial z}$$

$$= \frac{1}{\Delta z_k} [\bar{V}_{i,j+\frac{1}{2},k+\frac{1}{2}} \bar{W}_{i,j+\frac{1}{2},k+\frac{1}{2}} \bar{\rho}_{i,j+\frac{1}{2},k+\frac{1}{2}}$$

$$- \bar{V}_{i,j+\frac{1}{2},k-\frac{1}{2}} \bar{W}_{i,j+\frac{1}{2},k-\frac{1}{2}} \bar{\rho}_{i,j+\frac{1}{2},k-\frac{1}{2}}] \qquad (A.3)$$

$$CVC = 2\,\frac{\rho v u}{r}$$

$$= \frac{2\overline{\rho}_{i,j+\frac{1}{2},k}}{r_i}\left[\frac{\overline{U}_{i+\frac{1}{2},j+\frac{1}{2},k}\overline{V}_{i+\frac{1}{2},j+\frac{1}{2},k}+\overline{U}_{i-\frac{1}{2},j+\frac{1}{2},k}\overline{V}_{i-\frac{1}{2},j+\frac{1}{2},k}}{2}\right] \tag{A.4}$$

$$VISY1 = \frac{\partial^2 v}{\partial r^2}$$

$$= [V_{i+1,j+\frac{1}{2},k}(\Delta r_{i-1}+\Delta r_i)+V_{i-1,j+\frac{1}{2},k}(\Delta r_i+\Delta r_{i+1})$$

$$-V_{i,j+\frac{1}{2},k}(\Delta r_{i+1}+\Delta r_{i-1}+2\Delta r_i)]$$

$$/\frac{1}{8}\,(\Delta r_i+\Delta r_{i+1})(\Delta r_{i-1}+\Delta r_i)(\Delta r_{i+1}+\Delta r_{i-1}+2\Delta r_i) \tag{A.5}$$

$$VISY2 = \frac{1}{r}\,\frac{\partial v}{\partial r}$$

$$= \frac{V_{i+1,j+\frac{1}{2},k}-V_{i-1,j+\frac{1}{2},k}}{r_i\left(\frac{\Delta r_{i-1}}{2}+\Delta r_i+\frac{\Delta r_{i+1}}{2}\right)} \tag{A.6}$$

$$VISY3 = \frac{1}{r^2}\,\frac{\partial^2 v}{\partial \phi^2}$$

$$= \frac{V_{i,j+3/2,k}+V_{i,j-\frac{1}{2},k}-2V_{i,j+\frac{1}{2},k}}{(r_i\Delta\phi)^2} \tag{A.7}$$

$$VISY4 = \frac{\partial^2 v}{\partial z^2}$$

$$= [V_{i,j+\frac{1}{2},k+1}(\Delta z_k+\Delta z_{k-1})+V_{i,j+\frac{1}{2},k-1}(\Delta z_k+\Delta z_{k+1})$$

$$-V_{i,j+\frac{1}{2},k}(\Delta z_{k+1}+\Delta z_{k-1}+2\Delta z_k)]$$

$$/\frac{1}{8}\,(\Delta z_k+\Delta z_{k+1})(\Delta z_k+\Delta z_{k-1})(\Delta z_{k+1}+\Delta z_{k-1}+2\Delta z_k) \tag{A.8}$$

$$VISY5 = \frac{2}{r^2}\frac{\partial u}{\partial \phi}$$

$$= \frac{2(U_{i+\frac{1}{2},j+\frac{1}{2},k} - U_{i+\frac{1}{2},j,k})}{r_i^2 \Delta\phi} \qquad (A.9)$$

$$VISY6 = \frac{v}{r^2}$$

$$= \frac{V_{i,j+\frac{1}{2},k}}{r_i^2} \qquad (A.10)$$

With the upwind differencing, equations (A.1) through (A.4) becomes:

$$CVX = \frac{1}{\Delta r_i}\left[\bar{U}_{i+\frac{1}{2},j+\frac{1}{2},k}\bar{V}_{i+\frac{1}{2},j+\frac{1}{2},k}\bar{\rho}_{i+\frac{1}{2},j+\frac{1}{2},k}\right.$$

$$\left. - \bar{U}_{i-\frac{1}{2},j+\frac{1}{2},k}\bar{V}_{i-\frac{1}{2},j+\frac{1}{2},k}\bar{\rho}_{i-\frac{1}{2},j+\frac{1}{2},k}\right]$$

$$+ \frac{\zeta}{2}\left[\frac{|\bar{U}_{i+\frac{1}{2},j+\frac{1}{2},k}|(V_{i,j+\frac{1}{2},k} - V_{i+1,j+\frac{1}{2},k})\bar{\rho}_{i+\frac{1}{2},j+\frac{1}{2},k}}{(\Delta r_i + \Delta r_{i+1})/2}\right.$$

$$\left. - \frac{|\bar{U}_{i-\frac{1}{2},j+\frac{1}{2},k}|(V_{i-1,j+\frac{1}{2},k} - V_{i,j+\frac{1}{2},k})\bar{\rho}_{i-\frac{1}{2},j+\frac{1}{2},k}}{(\Delta r_i + \Delta r_{i-1})/2}\right] \qquad (A.11)$$

$$CVY = \frac{(\bar{V}_{i,j+1,k})^2 \rho_{i,j+1,k} - (\bar{V}_{i,j,k})^2 \rho_{i,j,k}}{r_i \Delta\phi}$$

$$+ \frac{\zeta}{2r_i\Delta\phi}\left[|\bar{V}_{i,j+1,k}|(V_{i,j+\frac{1}{2},k} - V_{i,j+3/2,k})\rho_{i,j+1,k}\right.$$

$$\left. - |\bar{V}_{i,j,k}|(V_{i,j-\frac{1}{2},k} - V_{i,j+\frac{1}{2},k})\rho_{i,j,k}\right] \qquad (A.12)$$

$$CVZ = \frac{1}{\Delta z_k}\left[\overline{V}_{i,j+\frac{1}{2},k+\frac{1}{2}}\overline{W}_{i,j+\frac{1}{2},k+\frac{1}{2}}\overline{\rho}_{i,j+\frac{1}{2},k+\frac{1}{2}}\right.$$

$$\left.-\overline{V}_{i,j+\frac{1}{2},k-\frac{1}{2}}\overline{W}_{i,j+\frac{1}{2},k-\frac{1}{2}}\overline{\rho}_{i,j+\frac{1}{2},k-\frac{1}{2}}\right]$$

$$+\frac{\zeta}{2}\left[\frac{|\overline{W}_{i,j+\frac{1}{2},k+\frac{1}{2}}|(V_{i,j+\frac{1}{2},k}-V_{i,j+\frac{1}{2},k+1})\overline{\rho}_{i,j+\frac{1}{2},k+\frac{1}{2}}}{(\Delta z_k+\Delta z_{k+1})/2}\right.$$

$$\left.-\frac{|\overline{W}_{i,j+\frac{1}{2},k-\frac{1}{2}}|(V_{i,j+\frac{1}{2},k-1}-V_{i,j+\frac{1}{2},k})\overline{\rho}_{i,j+\frac{1}{2},k-\frac{1}{2}}}{(\Delta z_k+\Delta z_{k-1})/2}\right] \qquad (A.13)$$

$$CVC = \frac{2}{r_i}\left[\frac{\overline{U}_{i+\frac{1}{2},j+\frac{1}{2},k}\overline{V}_{i+\frac{1}{2},j+\frac{1}{2},k}+\overline{U}_{i-\frac{1}{2},j+\frac{1}{2},k}\overline{V}_{i-\frac{1}{2},j+\frac{1}{2},k}}{2}\right]\overline{\rho}_{i,j+\frac{1}{2},k}$$

$$+\frac{\zeta}{2r_i}\left[|\overline{U}_{i+\frac{1}{2},j+\frac{1}{2},k}|(V_{i,j+\frac{1}{2},k}-V_{i+1,j+\frac{1}{2},k})\overline{\rho}_{i+\frac{1}{2},j+\frac{1}{2},k}\right.$$

$$\left.+|\overline{U}_{i-\frac{1}{2},j+\frac{1}{2},k}|(V_{i-1,j+\frac{1}{2},k}-V_{i,j+\frac{1}{2},k})\overline{\rho}_{i-\frac{1}{2},j+\frac{1}{2},k}\right] \qquad (A.14)$$

From equation (3.21), the convective and viscous terms are written as:

$$CWX = \frac{\partial \rho uw}{\partial r}$$

$$= \frac{1}{\Delta r_i}\left[\overline{U}_{i+\frac{1}{2},j,k+\frac{1}{2}}\overline{W}_{i+\frac{1}{2},j,k+\frac{1}{2}}\overline{\rho}_{i+\frac{1}{2},j,k+\frac{1}{2}}\right.$$

$$\left.-\overline{U}_{i-\frac{1}{2},j,k+\frac{1}{2}}\overline{W}_{i-\frac{1}{2},j,k+\frac{1}{2}}\overline{\rho}_{i-\frac{1}{2},j,k+\frac{1}{2}}\right] \qquad (A.15)$$

$$CWY = \frac{1}{r}\frac{\partial \rho vw}{\partial \phi}$$

$$= \frac{1}{r_i \Delta\phi}\left[\bar{V}_{i,j+\frac{1}{2},k+\frac{1}{2}}\bar{W}_{i,j+\frac{1}{2},k+\frac{1}{2}}\bar{\rho}_{i,j+\frac{1}{2},k+\frac{1}{2}}\right.$$

$$\left.-\bar{V}_{i,j-\frac{1}{2},k+\frac{1}{2}}\bar{W}_{i,j-\frac{1}{2},k+\frac{1}{2}}\bar{\rho}_{i,j-\frac{1}{2},k+\frac{1}{2}}\right] \qquad (A.16)$$

$$CWZ = \frac{\partial \rho w^2}{\partial z}$$

$$= \left[\frac{(\bar{W}_{i,j,k+1})^2\rho_{i,j,k+1}-(\bar{W}_{i,j,k})^2\rho_{i,j,k}}{(\Delta z_k+\Delta z_{k+1})/2}\right] \qquad (A.17)$$

$$CWC = \frac{\rho uw}{r}$$

$$= \frac{\bar{\rho}_{i,j,k+\frac{1}{2}}}{r_i}\left[\frac{\bar{U}_{i+\frac{1}{2},j,k+\frac{1}{2}}\bar{W}_{i+\frac{1}{2},j,k+\frac{1}{2}}+\bar{U}_{i-\frac{1}{2},j,k+\frac{1}{2}}\bar{W}_{i-\frac{1}{2},j,k+\frac{1}{2}}}{2}\right] \qquad (A.18)$$

$$VISZ1 = \frac{\partial^2 w}{\partial r^2}$$

$$= \left[W_{i+1,j,k+\frac{1}{2}}(\Delta r_i+\Delta r_{i-1})+W_{i-1,j,k+\frac{1}{2}}(\Delta r_i+\Delta r_{i+1})\right.$$

$$\left.-W_{i,j,k+\frac{1}{2}}(\Delta r_{i+1}+\Delta r_{i-1}+2\Delta r_i)\right]$$

$$/\frac{1}{8}(\Delta r_i+\Delta r_{i+1})(\Delta r_i+\Delta r_{i-1})(\Delta r_{i+1}+\Delta r_{i-1}+2\Delta r_i) \qquad (A.19)$$

$$VISZ2 = \frac{1}{r}\frac{\partial w}{\partial r}$$

$$= \frac{W_{i+1,j,k+\frac{1}{2}}-W_{i-1,j,k+\frac{1}{2}}}{r_i\left(\frac{\Delta r_{i-1}}{2}+\Delta r_i+\frac{\Delta r_{i+1}}{2}\right)} \qquad (A.20)$$

$$VISZ3 = \frac{1}{r^2}\frac{\partial^2 w}{\partial \phi^2}$$

$$= \frac{W_{i,j+1,k+\frac{1}{2}} + W_{i,j-1,k+\frac{1}{2}} - 2W_{i,j,k+\frac{1}{2}}}{(r_i \Delta\phi)^2} \qquad (A.21)$$

$$VISZ4 = \frac{\partial^2 w}{\partial z^2}$$

$$= \frac{W_{i,j,k+3/2}\Delta z_k + W_{i,j,k-\frac{1}{2}}\Delta z_{k+1} - W_{i,j,k+\frac{1}{2}}(\Delta z_k + \Delta z_{k+1})}{\Delta z_k \Delta z_{k+1}(\Delta z_k + \Delta z_{k+1})/2} \qquad (A.22)$$

Including the upwind differencing, equations (A.15) to (A.18) give:

$$CWX = \frac{1}{\Delta r_i}\left[\overline{U}_{i+\frac{1}{2},j,k+\frac{1}{2}}\overline{W}_{i+\frac{1}{2},j,k+\frac{1}{2}}\overline{\rho}_{i+\frac{1}{2},j,k+\frac{1}{2}} - \overline{U}_{i-\frac{1}{2},j,k+\frac{1}{2}}\overline{W}_{i-\frac{1}{2},j,k+\frac{1}{2}}\overline{\rho}_{i-\frac{1}{2},j,k+\frac{1}{2}}\right]$$

$$+ \frac{\zeta}{2}\left[\frac{|\overline{U}_{i+\frac{1}{2},j,k+\frac{1}{2}}|(W_{i,j,k+\frac{1}{2}} - W_{i+1,j,k+\frac{1}{2}})\overline{\rho}_{i+\frac{1}{2},j,k+\frac{1}{2}}}{(\Delta r_i + \Delta r_{i+1})/2} - \frac{|\overline{U}_{i-\frac{1}{2},j,k+\frac{1}{2}}|(W_{i-1,j,k+\frac{1}{2}} - W_{i,j,k+\frac{1}{2}})\overline{\rho}_{i-\frac{1}{2},j,k+\frac{1}{2}}}{(\Delta r_{i-1} + \Delta r_i)/2}\right] \qquad (A.23)$$

$$CWY = \frac{1}{r_i \Delta\phi}\left[\overline{V}_{i,j+\frac{1}{2},k+\frac{1}{2}}\overline{W}_{i,j+\frac{1}{2},k+\frac{1}{2}}\overline{\rho}_{i,j+\frac{1}{2},k+\frac{1}{2}} - \overline{V}_{i,j-\frac{1}{2},k+\frac{1}{2}}\overline{W}_{i,j-\frac{1}{2},k+\frac{1}{2}}\overline{\rho}_{i,j-\frac{1}{2},k+\frac{1}{2}}\right]$$

$$+ \frac{\zeta}{2r_i \Delta\phi}\left[|\overline{V}_{i,j+\frac{1}{2},k+\frac{1}{2}}|(W_{i,j,k+\frac{1}{2}} - W_{i,j+1,k+\frac{1}{2}})\overline{\rho}_{i,j+\frac{1}{2},k+\frac{1}{2}} - |\overline{V}_{i,j-\frac{1}{2},k+\frac{1}{2}}|(W_{i,j-1,k+\frac{1}{2}} - W_{i,j,k+\frac{1}{2}})\overline{\rho}_{i,j-\frac{1}{2},k+\frac{1}{2}}\right] \qquad (A.24)$$

$$CWZ = \left[\frac{(\bar{W}_{i,j,k+1})^2 \rho_{i,j,k+1} - (\bar{W}_{i,j,k})^2 \rho_{i,j,k}}{(\Delta z_k + \Delta z_{k+1})/2}\right]$$

$$+ \frac{\zeta}{2}\left[\frac{|\bar{W}_{i,j,k+1}|(W_{i,j,k+\frac{1}{2}} - W_{i,j,k+3/2})\rho_{i,j,k+1}}{\Delta z_{k+1}}\right.$$

$$\left. - \frac{|\bar{W}_{i,j,k}|(W_{i,j,k-\frac{1}{2}} - W_{i,j,k+\frac{1}{2}})\rho_{i,j,k}}{\Delta z_k}\right] \qquad (A.25)$$

$$CWC = \frac{\bar{\rho}_{i,j,k+\frac{1}{2}}}{2r_i}\left[\bar{U}_{i+\frac{1}{2},j,k+\frac{1}{2}}\bar{W}_{i+\frac{1}{2},j,k+\frac{1}{2}} + \bar{U}_{i-\frac{1}{2},j,k+\frac{1}{2}}\bar{W}_{i-\frac{1}{2},j,k+\frac{1}{2}}\right]$$

$$+ \frac{\zeta}{4r_i}\left[|\bar{U}_{i+\frac{1}{2},j,k+\frac{1}{2}}|(W_{i,j,k+\frac{1}{2}} - W_{i+1,j,k+\frac{1}{2}})\bar{\rho}_{i+\frac{1}{2},j,k+\frac{1}{2}}\right.$$

$$\left. + |\bar{U}_{i-\frac{1}{2},j,k+\frac{1}{2}}|(W_{i-1,j,k+\frac{1}{2}} - W_{i,j,k+\frac{1}{2}})\bar{\rho}_{i-\frac{1}{2},j,k+\frac{1}{2}}\right] \qquad (A.26)$$

APPENDIX B

FINITE DIFFERENCE EQUATIONS FOR NODES USED IN THE SOLIDIFICATION CALCULATIONS

The finite difference equations have been derived in Section 4.3.2 for the internal node, node on the outside surface of the mold and the interface node, before and after the air-gap formation. These nodes are indicated as node #1, 2, and 11 respectively in Figure 4.9. Using the same approach, this appendix presents the derivation of the finite difference equations for other nodes in the grid. The equations are written in cylindrical coordinate system.

Outside Mold Boundary (Bottom)

This is the node at the bottom of the mold or node #3 as indicated in Fig. 4.9. The outside surface is exposed to the ambience. Performing a heat balance on the element shown in Fig. B.1,

$$K_{i-1,i}\left[\left(r_i - \xi\,\frac{\Delta r_i}{2}\right)\Delta\phi_j\,\frac{\Delta z_k}{2}\right]\frac{(T_{i-1,j,k}-T_{i,j,k})}{(\Delta r_{i-1}+\Delta r_i)/2}$$

$$+ K_{i,i+1}\left[\left(r_i + \xi\,\frac{\Delta r_i}{2}\right)\Delta\phi_j\,\frac{\Delta z_k}{2}\right]\frac{(T_{i+1,j,k}-T_{i,j,k})}{(\Delta r_i+\Delta r_{i+1})/2}$$

$$+ K_{j-1,j}\left[\Delta r_i\,\frac{\Delta z_k}{2}\right]\frac{(T_{i,j-1,k}-T_{i,j,k})}{r_i(\Delta\phi_{j-1}+\Delta\phi_j)/2}$$

$$+ K_{j,j+1}\left[\Delta r_i\,\frac{\Delta z_k}{2}\right]\frac{(T_{i,j+1,k}-T_{i,j,k})}{r_i(\Delta\phi_j+\Delta\phi_{j+1})/2}$$

$$+ K_{k-1,k}[\Delta r_i r_i \Delta\phi_j]\frac{(T_{i,j,k-1}-T_{i,j,k})}{(\Delta z_{k-1}+\Delta z_k)/2}$$

$$+ h_b[\Delta r_i r_i \Delta\phi_j](T_a-T_{i,j,k})$$

$$= \rho_{i,j,k}C_{i,j,k}[\Delta r_i r_i \Delta\phi_j \frac{\Delta z_k}{2}]\frac{(T^{n+1}_{i,j,k}-T^{n}_{i,j,k})}{\Delta t} \qquad (B.1)$$

Outside Mold Corner (Bottom)

This node is found at the outside corner of the mold (note #4) and heat losses to the ambience through the bottom and side surface are calculated using the effective heat transfer coefficients h_b and h_s respectively. From Fig. B.2, the finite difference equation is written as

$$K_{i-1,i}[(r_i-\xi\frac{\Delta r_i}{2})\Delta\phi_j\frac{\Delta z_k}{2}]\frac{(T_{i-1,j,k}-T_{i,j,k})}{(\Delta r_{i-1}+\Delta r_i)/2}$$

$$+ h_s[r_i\Delta\phi_j\frac{\Delta z_k}{2}](T_a-T_{i,j,k})$$

$$+ K_{j-1,j}[\frac{\Delta r_i}{2}\ \frac{\Delta z_k}{2}]\frac{(T_{i,j-1,k}-T_{i,j,k})}{r_i(\Delta\phi_{j-1}+\Delta\phi_j)/2}$$

$$+ K_{j,j+1}[\frac{\Delta r_i}{2}\ \frac{\Delta z_k}{2}]\frac{(T_{i,j+1,k}-T_{i,j,k})}{r_i(\Delta\phi_j+\Delta\phi_{j+1})/2}$$

$$+ K_{k-1,k}[r_i\Delta\phi_j\frac{\Delta r_i}{2}]\frac{(T_{i,j,k-1}-T_{i,j,k})}{(\Delta z_{k-1}+\Delta z_k)/2}$$

$$+ h_b[r_i\Delta\phi_j\frac{\Delta r_i}{2}](T_a-T_{i,j,k})$$

$$= \rho_{i,j,k}C_{i,j,k}[\frac{\Delta r_i}{2}\ r_i\Delta\phi_j\frac{\Delta z_k}{2}]\frac{(T^{n+1}_{i,j,k}-T^{n}_{i,j,k})}{\Delta t} \qquad (B.2)$$

Top Boundary (Node #5)

Heat losses to the ambience are calculated with h_t. This equation applies to both the top boundary of the cast and mold with the appropriate properties used. From Fig. B.3,

$$K_{i-1,i}\left[\left(r_i-\xi\frac{\Delta r_i}{2}\right)\Delta\phi_j\frac{\Delta z_k}{2}\right]\frac{(T_{i-1,j,k}-T_{i,j,k})}{(\Delta r_{i-1}+\Delta r_i)/2}$$

$$+ K_{i,i+1}\left[\left(r_i+\xi\frac{\Delta r_i}{2}\right)\Delta\phi_j\frac{\Delta z_k}{2}\right]\frac{(T_{i+1,j,k}-T_{i,j,k})}{(\Delta r_i+\Delta r_{i+1})/2}$$

$$+ K_{j-1,j}\left[\Delta r_i\frac{\Delta z_k}{2}\right]\frac{(T_{i,j-1,k}-T_{i,j,k})}{r_i(\Delta\phi_{j-1}+\Delta\phi_j)/2}$$

$$+ K_{j,j+1}\left[\Delta r_i\frac{\Delta z_k}{2}\right]\frac{(T_{i,j+1,k}-T_{i,j,k})}{r_i(\Delta\phi_j+\Delta\phi_{j+1})/2}$$

$$+ h_t[\Delta r_i r_i\Delta\phi_j](T_a-T_{i,j,k})$$

$$+ K_{k,k+1}[\Delta r_i r_i\Delta\phi_j]\frac{(T_{i,j,k+1}-T_{i,j,k})}{(\Delta z_k+\Delta z_{k+1})/2}$$

$$= \rho_{i,j,k}C_{i,j,k}[\Delta r_i r_i\Delta\phi_j\frac{\Delta z_k}{2}]\frac{(T^{n+1}_{i,j,k}-T^{n}_{i,j,k})}{\Delta t} \qquad \text{(B.3)}$$

Top Mold Corner (Node #6)

Similar to the bottom mold corner, the finite difference equation for the element shown in Fig. B.4 is

$$K_{i-1,i}\left[\left(r_i-\xi\frac{\Delta r_i}{2}\right)\Delta\phi_j\frac{\Delta z_k}{2}\right]\frac{(T_{i-1,j,k}-T_{i,j,k})}{(\Delta r_{i-1}+\Delta r_i)/2}$$

$$+ h_s\left[r_i\Delta\phi_j\frac{\Delta z_k}{2}\right](T_a-T_{i,j,k})$$

$$+ K_{j-1,j}\left[\frac{\Delta r_i}{2}\,\frac{\Delta z_k}{2}\right]\frac{(T_{i,j-1,k}-T_{i,j,k})}{r_i(\Delta\phi_{j-1}+\Delta\phi_j)/2}$$

$$+ K_{j,j+1}\left[\frac{\Delta r_i}{2}\,\frac{\Delta z_k}{2}\right]\frac{(T_{i,j+1,k}-T_{i,j,k})}{r_i(\Delta\phi_j+\Delta\phi_{j+1})/2}$$

$$+ h_t\left[r_i\Delta\phi_j\frac{\Delta r_i}{2}\right](T_a-T_{i,j,k})$$

$$+ K_{k,k+1}\left[r_i\Delta\phi_j\frac{\Delta r_i}{2}\right]\frac{(T_{i,j,k+1}-T_{i,j,k})}{(\Delta z_k+\Delta z_{k+1})/2}$$

$$= \rho_{i,j,k}C_{i,j,k}\left[\frac{\Delta r_i}{2}\; r_i\Delta\phi_j\frac{\Delta z_k}{2}\right]\frac{(T^{n+1}_{i,j,k}-T^{n}_{i,j,k})}{\Delta t} \qquad (B.4)$$

Centreline Node (Node #7)

At the point located on the axis of symmetry, difficulties were encountered in solving the differential equations as $r\to 0$. Thus, the centreline node is chosen as shown in Fig. B.5. Performing the heat balance, there is no heat flow from the centreline because of zero surface area; thus

$$0 + K_{i,i+1}\left[(r_i+\xi\frac{\Delta r_i}{2})\Delta\phi_j\Delta z_k\right]\frac{(T_{i+1,j,k}-T_{i,j,k})}{(\Delta r_i+\Delta r_{i+1})/2}$$

$$+ K_{j-1,j}\left[\Delta r_i\Delta z_k\right]\frac{(T_{i,j-1,k}-T_{i,j,k})}{r_i(\Delta\phi_{j-1}+\Delta\phi_j)/2}$$

$$+ K_{j,j+1}\left[\Delta r_i\Delta z_k\right]\frac{(T_{i,j+1,k}-T_{i,j,k})}{r_i(\Delta\phi_j+\Delta\phi_{j+1})/2}$$

$$+ K_{k-1,k}\left[\Delta r_i r_i\Delta\phi_j\right]\frac{(T_{i,j,k-1}-T_{i,j,k})}{(\Delta z_{k-1}+\Delta z_k)/2}$$

$$+ K_{k,k+1}\left[\Delta r_i r_i\Delta\phi_j\right]\frac{(T_{i,j,k+1}-T_{i,j,k})}{(\Delta z_k+\Delta z_{k+1})/2}$$

$$= \rho_{i,j,k} C_{i,j,k} [\Delta r_i r_i \Delta\phi_j \Delta z_k] \frac{(T^{n+1}_{i,j,k} - T^{n}_{i,j,k})}{\Delta t} \qquad (B.5)$$

Centreline Node at the Cast/Mold Interface

In a similar way, the interface node (node #8) at the centreline (Fig. B.6) can be written as

$$0 + [K^{c}_{i,i+1} + K^{m}_{i,i+1}] [(r_i + \xi \frac{\Delta r_i}{2}) \Delta\phi_j \frac{\Delta z_k}{2}] \frac{(T_{i+1,j,k} - T_{i,j,k})}{(\Delta r_i + \Delta r_{i+1})/2}$$

$$+ [K^{c}_{j-1,j} + K^{m}_{j-1,j}] [\Delta r_i \frac{\Delta z_k}{2}] \frac{(T_{i,j-1,k} - T_{i,j,k})}{r_i (\Delta\phi_{j-1} + \Delta\phi_j)/2}$$

$$+ [K^{c}_{j,j+1} + K^{m}_{j,j+1}] [\Delta r_i \frac{\Delta z_k}{2}] \frac{(T_{i,j+1,k} - T_{i,j,k})}{r_i (\Delta\phi_j + \Delta\phi_{j+1})/2}$$

$$+ K^{c}_{k-1,k} [r_i \Delta\phi_j \Delta r_i] \frac{(T_{i,j,k-1} - T_{i,j,k})}{(\Delta z_{k-1} + \Delta z_k)/2}$$

$$+ K^{m}_{k,k+1} [r_i \Delta\phi_j \Delta r_i] \frac{(T_{i,j,k+1} - T_{i,j,k})}{(\Delta z_k + \Delta z_{k+1})/2}$$

$$= [\rho^{c}_{i,j,k} C^{c}_{i,j,k} + \rho^{m}_{i,j,k} C^{m}_{i,j,k}] [\Delta r_i r_i \Delta\phi_j \frac{\Delta z_k}{2}] \frac{(T^{n+1}_{i,j,k} - T^{n}_{i,j,k})}{\Delta t} \qquad (B.6)$$

Centreline Node at the Top and the Bottom Boundary

From the heat balance, the finite difference equations for the top (node #9) and bottom (node #10) centreline nodes are written respectively as:

From Fig. B.7,

$$0 + K_{i,i+1}\left[\left(r_i+\xi\frac{\Delta r_i}{2}\right)\Delta\phi_j\frac{\Delta z_k}{2}\right]\frac{(T_{i+1,j,k}-T_{i,j,k})}{(\Delta r_i+\Delta r_{i+1})/2}$$

$$+ K_{j-1,j}\left[\Delta r_i\frac{\Delta z_k}{2}\right]\frac{(T_{i,j-1,k}-T_{i,j,k})}{r_i(\Delta\phi_{j-1}+\Delta\phi_j)/2}$$

$$+ K_{j,j+1}\left[\Delta r_i\frac{\Delta z_k}{2}\right]\frac{(T_{i,j+1,k}-T_{i,j,k})}{r_i(\Delta\phi_j+\Delta\phi_{j+1})/2}$$

$$+ h_t[r_i\Delta\phi_j\Delta r_i](T_a-T_{i,j,k})$$

$$+ K_{k,k+1}[r_i\Delta\phi_j\Delta r_i]\frac{(T_{i,j,k+1}-T_{i,j,k})}{(\Delta z_k+\Delta z_{k+1})/2}$$

$$= \rho_{i,j,k}C_{i,j,k}\left[\Delta r_i r_i\Delta\phi_j\frac{\Delta z_k}{2}\right]\frac{(T^{n+1}_{i,j,k}-T^{n}_{i,j,k})}{\Delta t} \qquad \text{(B.7)}$$

From Fig. B.8,

$$0 + K_{i,i+1}\left[\left(r_i+\xi\frac{\Delta r_i}{2}\right)\Delta\phi_j\frac{\Delta z_k}{2}\right]\frac{(T_{i+1,j,k}-T_{i,j,k})}{(\Delta r_i+\Delta r_{i+1})/2}$$

$$+ K_{j-1,j}\left[\Delta r_i\frac{\Delta z_k}{2}\right]\frac{(T_{i,j-1,k}-T_{i,j,k})}{r_i(\Delta\phi_{j-1}+\Delta\phi_j)/2}$$

$$+ K_{j,j+1}\left[\Delta r_i\frac{\Delta z_k}{2}\right]\frac{(T_{i,j+1,k}-T_{i,j,k})}{r_i(\Delta\phi_j+\Delta\phi_{j+1})/2}$$

$$+ K_{k-1,k}[\Delta r_i r_i\Delta\phi_j]\frac{(T_{i,j,k-1}-T_{i,j,k})}{(\Delta z_{k-1}+\Delta z_k)/2}$$

$$+ h_b[\Delta r_i r_i\Delta\phi_j](T_a-T_{i,j,k})$$

$$= \rho_{i,j,k}C_{i,j,k}\left[\Delta r_i r_i\Delta\phi_j\frac{\Delta z_k}{2}\right]\frac{(T^{n+1}_{i,j,k}-T^{n}_{i,j,k})}{\Delta t} \qquad \text{(B.8)}$$

Cast/Mold Interface Node (Bottom)

This is the interface node at the bottom of the casting indicated by node #12. In the model, the casting is assumed to be resting its weight on the mold on this surface. No contact resistance is considered. From Fig. B.9,

$$[K^c_{i-1,i}+K^m_{i-1,i}]\left[\left(r_i-\xi\frac{\Delta r_i}{2}\right)\Delta\phi_j\frac{\Delta z_k}{2}\right]\frac{(T_{i-1,j,k}-T_{i,j,k})}{(\Delta r_{i-1}+\Delta r_i)/2}$$

$$+\ [K^c_{i,i+1}+K^m_{i,i+1}]\left[\left(r_i+\xi\frac{\Delta r_i}{2}\right)\Delta\phi_j\frac{\Delta z_k}{2}\right]\frac{(T_{i+1,j,k}-T_{i,j,k})}{(\Delta r_i+\Delta r_{i+1})/2}$$

$$+\ [K^c_{j-1,j}+K^m_{j-1,j}]\left[\Delta r_i\frac{\Delta z_k}{2}\right]\frac{(T_{i,j-1,k}-T_{i,j,k})}{r_i(\Delta\phi_{j-1}+\Delta\phi_j)/2}$$

$$+\ [K^c_{j,j+1}+K^m_{j,j+1}]\left[\Delta r_i\frac{\Delta z_k}{2}\right]\frac{(T_{i,j+1,k}-T_{i,j,k})}{r_i(\Delta\phi_j+\Delta\phi_{j+1})/2}$$

$$+\ K^c_{k-1,k}[r_i\Delta\phi_j\Delta r_i]\frac{(T_{i,j,k-1}-T_{i,j,k})}{(\Delta z_{k-1}+\Delta z_k)/2}$$

$$+\ K^m_{k,k+1}[r_i\Delta\phi_j\Delta r_i]\frac{(T_{i,j,k+1}-T_{i,j,k})}{(\Delta z_k+\Delta z_{k+1})/2}$$

$$=\ [\rho^c_{i,j,k}C^c_{i,j,k}+\rho^m_{i,j,k}C^m_{i,j,k}]\left[\Delta r_i r_i\Delta\phi_j\frac{\Delta z_k}{2}\right]\frac{(T^{n+1}_{i,j,k}-T^n_{i,j,k})}{\Delta t} \qquad (B.9)$$

Cast/Mold Interface Node (Corner)

This is the corner node indicated by node #16. Before the formation of the air-gap, the element is shown in Fig. B10a and the heat balance gives

$$[K^c_{i-1,i}+K^m_{i-1,i}][(r_i-\xi\frac{\Delta r_i}{2})\Delta\phi_j\frac{\Delta z_k}{2}]\frac{(T_{i-1,j,k}-T_{i,j,k})}{(\Delta r_{i-1}+\Delta r_i)/2}$$

$$+ K^m_{i,i+1}[(r_i+\xi\frac{\Delta r_i}{2})\Delta\phi_j\Delta z_k]\frac{(T_{i+1,j,k}-T_{i,j,k})}{(\Delta r_i+\Delta r_{i+1})/2}$$

$$+ [\frac{1}{4}K^c_{j-1,j}+\frac{3}{4}K^m_{j-1,j}][\Delta r_i\Delta z_k]\frac{(T_{i,j-1,k}-T_{i,j,k})}{r_i(\Delta\phi_{j-1}+\Delta\phi_j)/2}$$

$$+ [\frac{1}{4}K^c_{j,j+1}+\frac{3}{4}K^m_{j,j+1}][\Delta r_i\Delta z_k]\frac{(T_{i,j+1,k}-T_{i,j,k})}{r_i(\Delta\phi_j+\Delta\phi_{j+1})/2}$$

$$+ [K^c_{k-1,k}+K^m_{k-1,k}][r_i\Delta\phi_j\frac{\Delta r_i}{2}]\frac{(T_{i,j,k-1}-T_{i,j,k})}{(\Delta z_{k-1}+\Delta z_k)/2}$$

$$+ K^m_{k,k+1}[r_i\Delta\phi_j\Delta r_i]\frac{(T_{i,j,k+1}-T_{i,j,k})}{(\Delta z_k+\Delta z_{k+1})/2}$$

$$= [\frac{1}{4}\rho^c_{i,j,k}C^c_{i,j,k}+\frac{3}{4}\rho^m_{i,j,k}C^m_{i,j,k}][\Delta r_i r_i\Delta\phi_j\Delta z_k]\frac{(T^{n+1}_{i,j,k}-T^n_{i,j,k})}{\Delta t} \qquad (B.10)$$

After the formation of the air-gap, the corner node is shown in Fig. B.10b. The heat balance gives

$$h_g[r_i\Delta\phi_j\frac{\Delta z_k}{2}](T_{i-1,j,k}-T_{i,j,k})$$

$$+ K^m_{i-1,i}[(r_i-\xi\frac{\Delta r_i}{2})\Delta\phi_j\frac{\Delta z_k}{2}]\frac{(T_{i-1,j,k}-T_{i,j,k})}{(\Delta r_{i-1}+\Delta r_i)/2}$$

$$+ K^m_{i,i+1}[(r_i+\xi\frac{\Delta r_i}{2})\Delta\phi_j\Delta z_k]\frac{(T_{i+1,j,k}-T_{i,j,k})}{(\Delta r_i+\Delta r_{i+1})/2}$$

$$+ K^m_{j-1,j}[\frac{3}{4}\Delta r_i\Delta z_k]\frac{(T_{i,j-1,k}-T_{i,j,k})}{r_i(\Delta\phi_{j-1}+\Delta\phi_j)/2}$$

$$+ K^m_{j,j+1}\left[\frac{3}{4}\Delta r_i \Delta z_k\right]\frac{(T_{i,j+1,k}-T_{i,j,k})}{r_i(\Delta\phi_j+\Delta\phi_{j+1})/2}$$

$$+ h_g\left[r_i\Delta\phi_j\frac{\Delta r_i}{2}\right](T_{i,j,k+1}-T_{i,j,k})$$

$$+ K^m_{k-1,k}\left[r_i\Delta\phi_j\frac{\Delta r_i}{2}\right]\frac{(T_{i,j,k-1}-T_{i,j,k})}{(\Delta z_{k-1}+\Delta z_k)/2}$$

$$+ K^m_{k,k+1}\left[r_i\Delta\phi_j\Delta r_i\right]\frac{(T_{i,j,k+1}-T_{i,j,k})}{(\Delta z_k+\Delta z_{k+1})/2}$$

$$= \rho^m_{i,j,k}C^m_{i,j,k}\left[\frac{3}{4}\Delta r_i r_i\Delta\phi_j\Delta z_k\right]\frac{(T^{n+1}_{i,j,k}-T^n_{i,j,k})}{\Delta t} \qquad \text{(B.11)}$$

Cast/Mold Interface Node (Top Boundary)

A similar approach is used for the interface node at the top boundary (node #14). Before the air-gap formation, from Fig. B.11a, the finite difference equation is

$$K^c_{i-1,i}\left[(r_i-\xi\frac{\Delta r_i}{2})\Delta\phi_j\frac{\Delta z_k}{2}\right]\frac{(T_{i-1,j,k}-T_{i,j,k})}{(\Delta r_{i-1}+\Delta r_i)/2}$$

$$+ K^m_{i,i+1}\left[(r_i+\xi\frac{\Delta r_i}{2})\Delta\phi_j\frac{\Delta z_k}{2}\right]\frac{(T_{i+1,j,k}-T_{i,j,k})}{(\Delta r_i+\Delta r_{i+1})/2}$$

$$+ [K^c_{j-1,j}+K^m_{j-1,j}]\left[\frac{\Delta r_i}{2}\frac{\Delta z_k}{2}\right]\frac{(T_{i,j-1,k}-T_{i,j,k})}{r_i(\Delta\phi_{j-1}+\Delta\phi_j)/2}$$

$$+ [K^c_{j,j+1}+K^m_{j,j+1}]\left[\frac{\Delta r_i}{2}\frac{\Delta z_k}{2}\right]\frac{(T_{i,j+1,k}-T_{i,j,k})}{r_i(\Delta\phi_j+\Delta\phi_{j+1})/2}$$

$$+ (h^c_t+h^m_t)\left[r_i\Delta\phi_j\frac{\Delta r_i}{2}\right](T_a-T_{i,j,k})$$

$$+ [K^{c}_{k,k+1}+K^{m}_{k,\ k+1}][r_i\Delta\phi_j\frac{\Delta r_i}{2}]\frac{(T_{i,j,k+1}-T_{i,j,k})}{(\Delta z_k+\Delta z_{k+1})/2}$$

$$= [\rho^{c}_{i,j,k}C^{c}_{i,j,k}+\rho^{m}_{i,j,k}C^{m}_{i,j,k}][\frac{\Delta r_i}{2}\ r_i\Delta\phi_j\ \frac{\Delta z_k}{2}]\frac{(T^{n+1}_{i,j,k}-T^{n}_{i,j,k})}{\Delta t} \qquad (B.12)$$

After the formation of the air-gap, the interface node becomes as shown in Fig. B.11b and the heat balance is

$$h_g[r_i\Delta\phi_j\frac{\Delta z_k}{2}](T_{i-1,j,k}-T_{i,j,k})$$

$$+ K^{m}_{i,i+1}[(r_i+\xi\frac{\Delta r_i}{2})\Delta\phi_j\frac{\Delta z_k}{2}]\frac{(T_{i+1,j,k}-T_{i,j,k})}{(\Delta r_i+\Delta r_{i+1})/2}$$

$$+ K^{m}_{j-1,j}[\frac{\Delta r_i}{2}\ \frac{\Delta z_k}{2}]\frac{(T_{i,j-1,k}-T_{i,j,k})}{r_i(\Delta\phi_{j-1}+\Delta\phi_j)/2}$$

$$+ K^{m}_{j,j+1}[\frac{\Delta r_i}{2}\ \frac{\Delta z_k}{2}]\frac{(T_{i,j+1,k}-T_{i,j,k})}{r_i(\Delta\phi_j+\Delta\phi_{j+1})/2}$$

$$+ h^{m}_{t}[r_i\Delta\phi_j\frac{\Delta r_i}{2}](T_a-T_{i,j,k})$$

$$+ K^{m}_{k,k+1}[r_i\Delta\phi_j\frac{\Delta r_i}{2}]\frac{(T_{i,j,k+1}-T_{i,j,k})}{(\Delta z_k+\Delta z_{k+1})/2}$$

$$= \rho^{m}_{i,j,k}C^{m}_{i,j,k}[\frac{\Delta r_i}{2}\ r_i\Delta\phi_j\frac{\Delta z_k}{2}]\frac{(T^{n+1}_{i,j,k}-T^{n}_{i,j,k})}{\Delta t} \qquad (B.13)$$

Node at Outer Surface of Cast (Node #15)

Before the air-gap formation, this node is just an internal node in the metal. After the formation of the gap, this node becomes a node on the outer surface of the cast

losing heat across the air-gap to the mold. The heat balance on Fig. B.12 gives

$$K^c_{i-1,i}\left[\left(r_i-\xi\frac{\Delta r_i}{2}\right)\Delta\phi_j\Delta z_k\right]\frac{(T_{i-1,j,k}-T_{i,j,k})}{(\Delta r_{i-1}+\Delta r_i)/2} -$$

$$+ h_g[r_i\Delta\phi_j\Delta z_k](T_{i+1,j,k}-T_{i,j,k})$$

$$+ K^c_{j-1,j}\left[\frac{\Delta r_i}{2}\,\Delta z_k\right]\frac{(T_{i,j-1,k}-T_{i,j,k})}{r_i(\Delta\phi_{j-1}+\Delta\phi_j)/2}$$

$$+ K^c_{j,j+1}\left[\frac{\Delta r_i}{2}\,\Delta z_k\right]\frac{(T_{i,j+1,k}-T_{i,j,k})}{r_i(\Delta\phi_j+\Delta\phi_{j+1})/2}$$

$$+ K^c_{k-1,k}\left[\frac{\Delta r_i}{2}\,r_i\Delta\phi_j\right]\frac{(T_{i,j,k-1}-T_{i,j,k})}{(\Delta z_{k-1}+\Delta z_k)/2}$$

$$+ K^c_{k,k+1}\left[\frac{\Delta r_i}{2}\,r_i\Delta\phi_j\right]\frac{(T_{i,j,k+1}-T_{i,j,k})}{(\Delta z_k+\Delta z_{k+1})/2}$$

$$= \rho^c_{i,j,k}C^c_{i,j,k}\left[\frac{\Delta r_i}{2}\,r_i\Delta\phi_j\Delta z_k\right]\frac{(T^{n+1}_{i,j,k}-T^n_{i,j,k})}{\Delta t} \qquad \text{(B.14)}$$

Outer Surface of Cast (at Bottom Interface)

This node is the node next to the inside corner node of the mold after the formation of the air-gap. This is indicated by node #16 in the grid arrangement. Before the gap formation, the finite difference equation is similar to the bottom interface node (#12). The finite difference equation for the node (Fig. B.13) after the gap is formed is

$$[K^c_{i-1,i}+K^m_{i-1,i}]\left[\left(r_i-\xi\frac{\Delta r_i}{2}\right)\Delta\phi_j\frac{\Delta z_k}{2}\right]\frac{(T_{i-1,j,k}-T_{i,j,k})}{(\Delta r_{i-1}+\Delta r_i)/2} -$$

$$+ h_g[r_i\Delta\phi_j\frac{\Delta z_k}{2}](T_{i+1,j,k}-T_{i,j,k})$$

$$+ K^m_{i,i+1}[(r_i+\xi\frac{\Delta r_i}{2})\Delta\phi_j\frac{\Delta z_k}{2}]\frac{(T_{i+1,j,k}-T_{i,j,k})}{(\Delta r_i+\Delta r_{i+1})/2}$$

$$+ [\tfrac{1}{2}K^c_{j-1,j}+\tfrac{1}{2}K^m_{j-1,j}][\Delta r_i\Delta z_k]\frac{(T_{i,j-1,k}-T_{i,j,k})}{r_i(\Delta\phi_{j-1}+\Delta\phi_j)/2}$$

$$+ [\tfrac{1}{2}K^c_{j,j+1}+\tfrac{1}{2}K^m_{j,j+1}][\Delta r_i\Delta z_k]\frac{(T_{i,j+1,k}-T_{i,j,k})}{r_i(\Delta\phi_j+\Delta\phi_{j+1})/2}$$

$$+ K^c_{k-1,k}[r_i\Delta\phi_j\frac{\Delta r_i}{2}]\frac{(T_{i,j,k-1}-T_{i,j,k})}{(\Delta z_{k-1}+\Delta z_k)/2}$$

$$+ h_g[r_i\Delta\phi_j\frac{\Delta r_i}{2}](T_{i,j,k-1}-T_{i,j,k})$$

$$+ K^m_{k,k+1}[r_i\Delta\phi_j\Delta r_i]\frac{(T_{i,j,k+1}-T_{i,j,k})}{(\Delta z_k+\Delta z_{k+1})/2}$$

$$= [\tfrac{1}{2}\rho^c_{i,j,k}C^c_{i,j,k}+\tfrac{1}{2}\rho^m_{i,j,k}C^m_{i,j,k}][\Delta r_i r_i\Delta\phi_j\Delta z_k]\frac{(T^{n+1}_{i,j,k}-T^n_{i,j,k})}{\Delta t} \qquad (B.15)$$

Outer Surface of the Cast (at Top Boundary)

This node (#17) is the same node as node #5 before the air-gap is formed. The finite difference equation after the formation of the gap for the element shown in Fig. B.14 is

$$K^c_{i-1,i}[(r_i-\xi\frac{\Delta r_i}{2})\Delta\phi_j\frac{\Delta z_k}{2}]\frac{(T_{i-1,j,k}-T_{i,j,k})}{(\Delta r_{i-1}+\Delta r_i)/2}$$

$$+ h_g[r_i\Delta\phi_j\frac{\Delta z_k}{2}](T_{i+1,j,k}-T_{i,j,k})$$

$$+ K^c_{j-1,j}\left[\frac{\Delta r_i}{2}\,\frac{\Delta z_k}{2}\right]\frac{(T_{i,j-1,k}-T_{i,j,k})}{r_i(\Delta\phi_{j-1}+\Delta\phi_j)/2}$$

$$+ K^c_{j,j+1}\left[\frac{\Delta r_i}{2}\,\frac{\Delta z_k}{2}\right]\frac{(T_{i,j+1,k}-T_{i,j,k})}{r_i(\Delta\phi_j+\Delta\phi_{j+1})/2}$$

$$+ h^c_t\left[r_i\Delta\phi_j\frac{\Delta r_i}{2}\right](T_a-T_{i,j,k})$$

$$+ K^c_{k,k+1}\left[r_i\Delta\phi_j\frac{\Delta r_i}{2}\right]\frac{(T_{i,j,k+1}-T_{i,j,k})}{(\Delta z_k+\Delta z_{k+1})/2}$$

$$= \rho^c_{i,j,k}C^c_{i,j,k}\left[\frac{\Delta r_i}{2}\,r_i\Delta\phi_j\frac{\Delta z_k}{2}\right]\frac{(T^{n+1}_{i,j,k}-T^n_{i,j,k})}{\Delta t} \qquad \text{(B.16)}$$

The finite difference equations for any other special nodes other than those already discussed can be readily derived in the same way. However, the above equations are sufficient for the present modelling purposes.

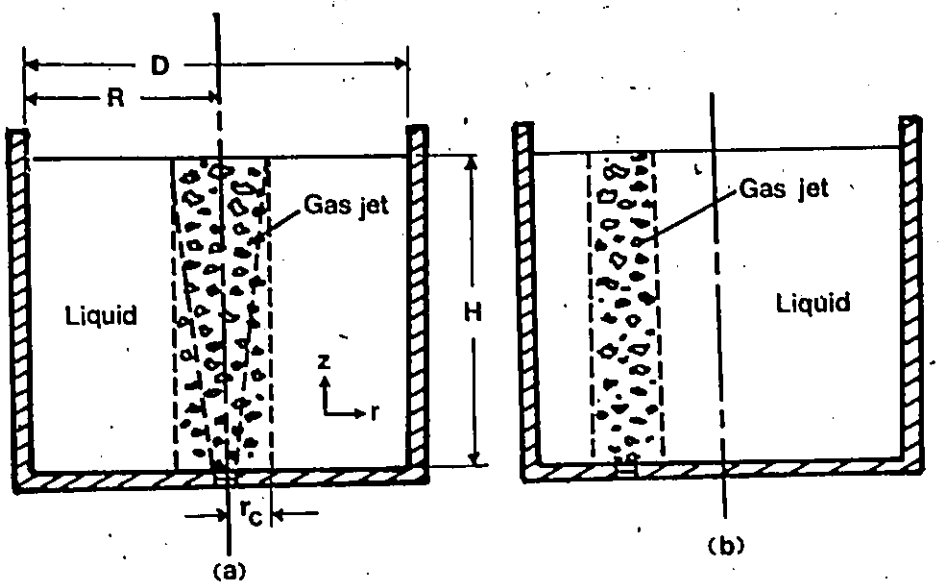

Fig. 3.1. Schematic diagram of (a) Central and (b) Off-centered jet.

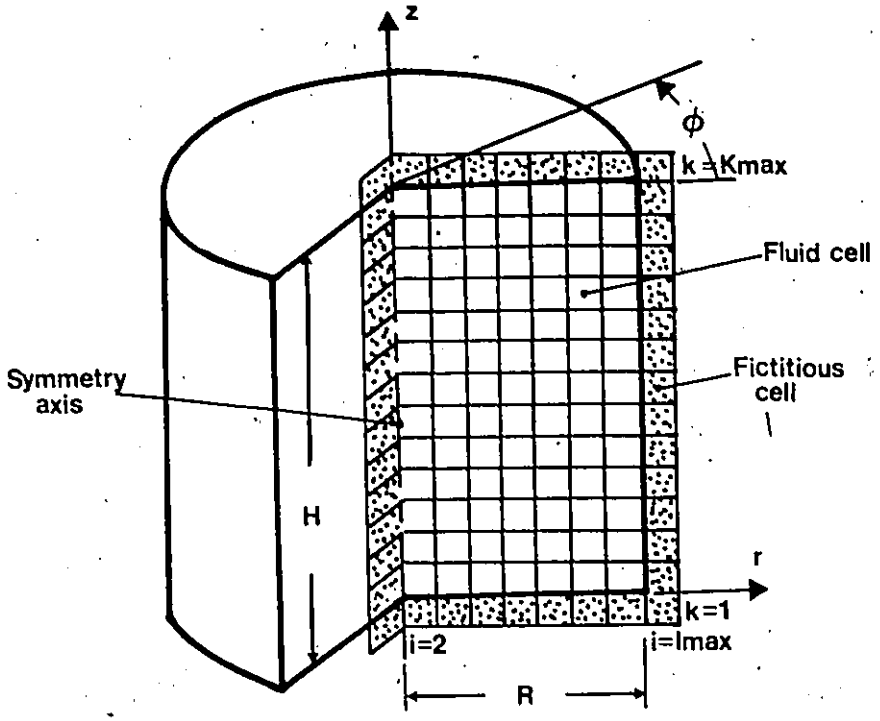

Fig. 3.2. Finite difference grid used in computations.

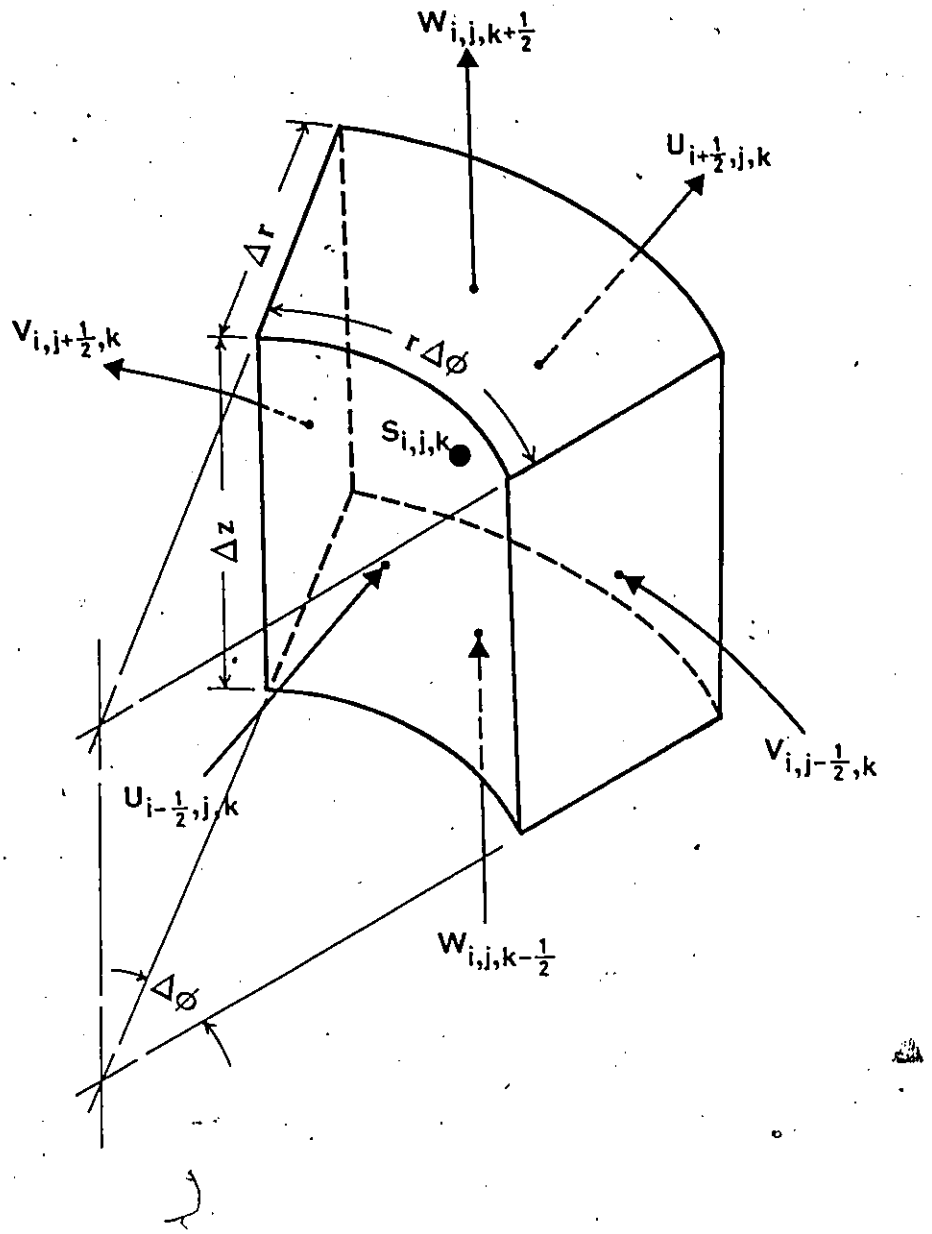

Fig. 3.3. A computational element.

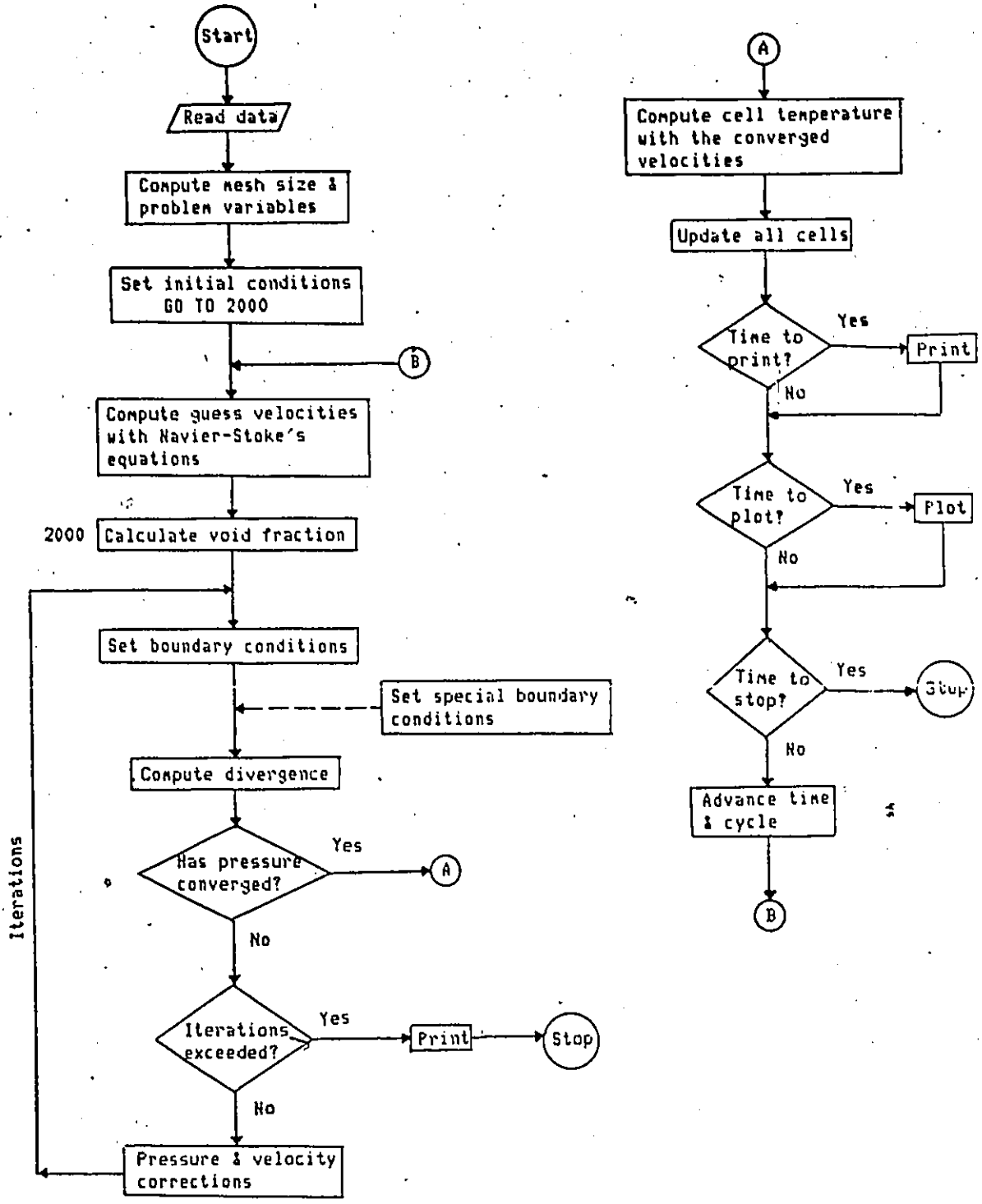

Fig. 3.4. Flow chart for multidimensional modelling.

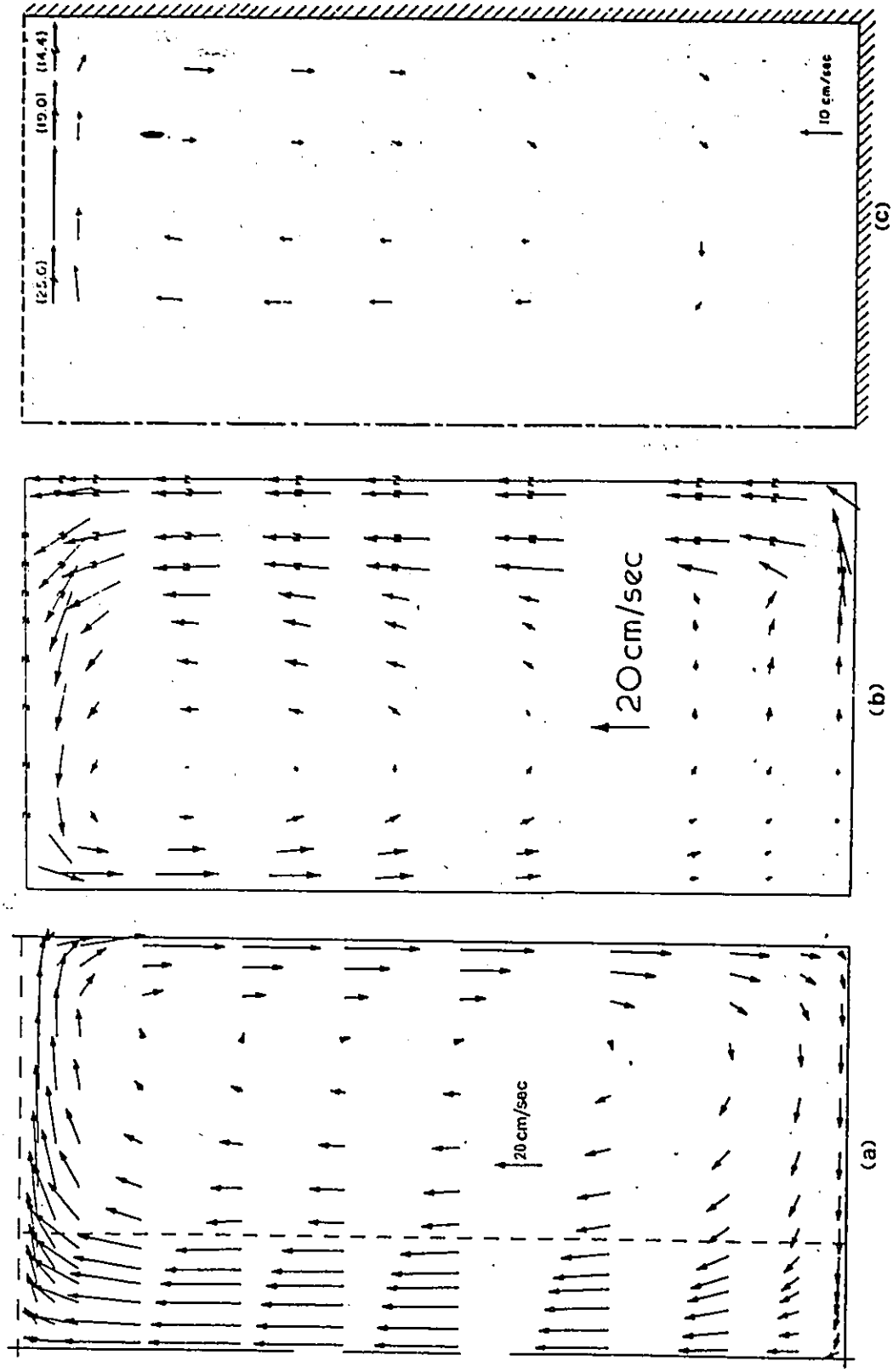

Fig. 3.5. Velocity fields for (a) two-dimensional computations of present code, (b) Deb Roy et al.'s model [29], (c) Szekely et al.'s experimental results [23].

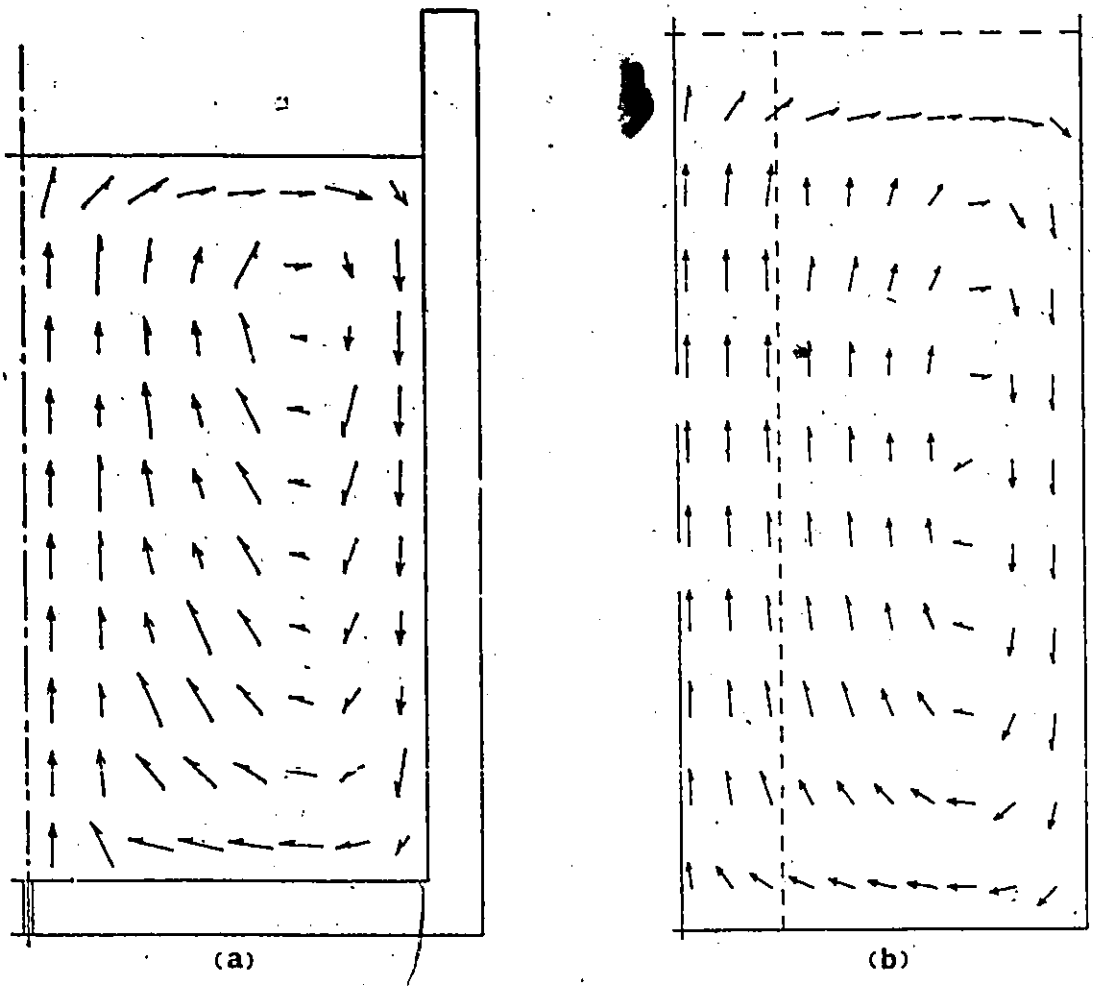

Fig. 3.6. Comparison between Guthrie et al.'s [69] prediction and results from present model.

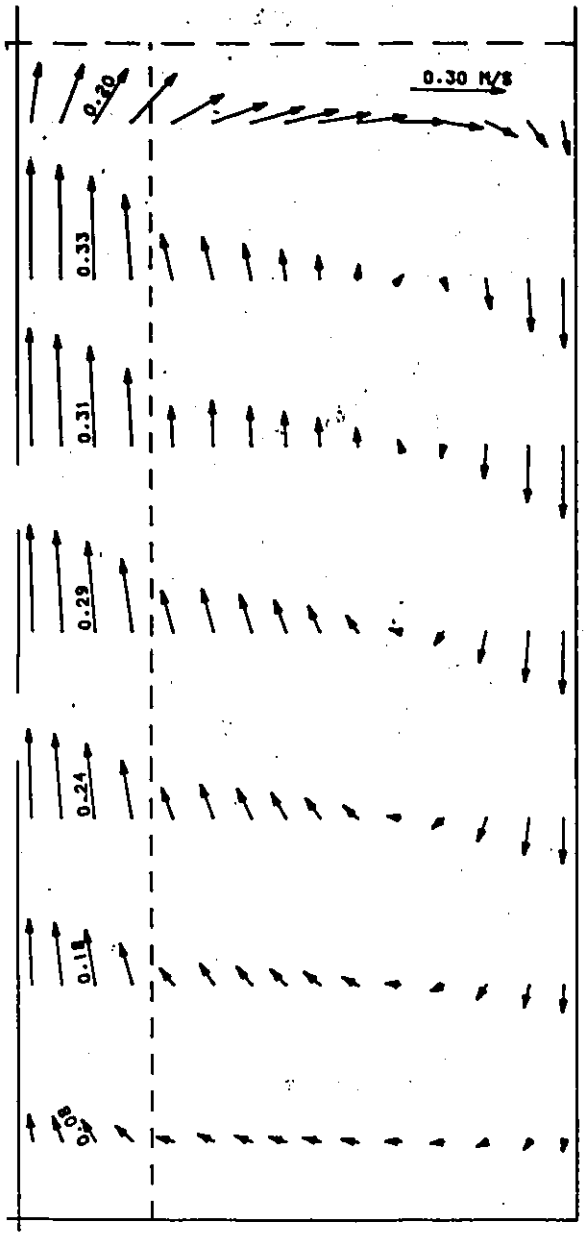

Fig. 3.7. Computed velocity field for a cylindrical jet with slip.

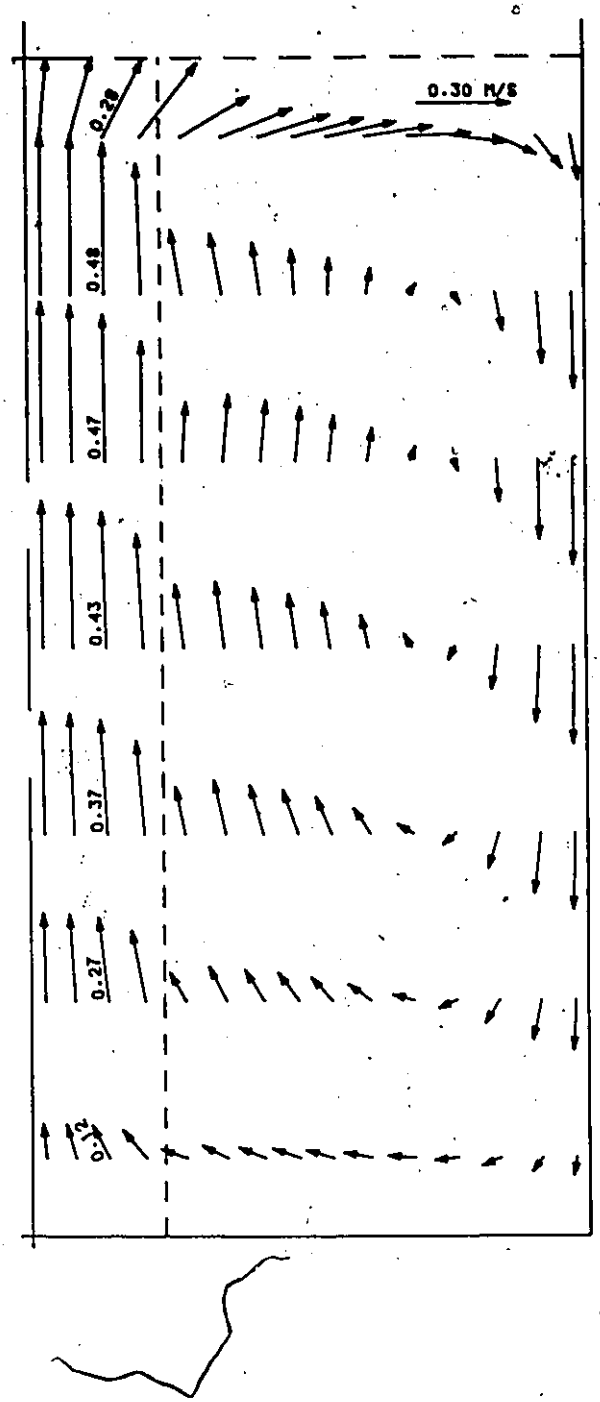

Fig. 3.8. Computed velocity field for a cylindrical jet with zero slip.

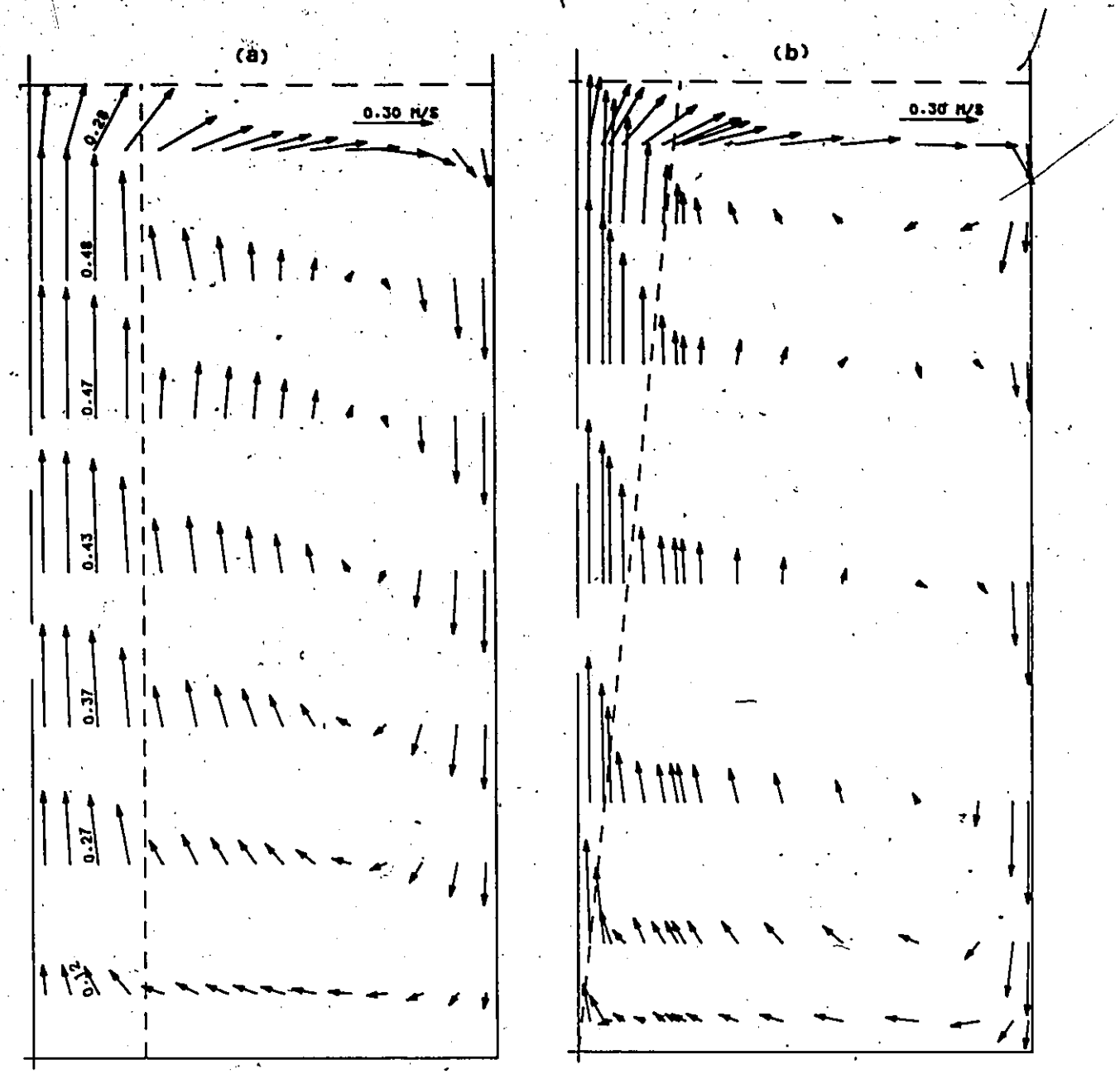

Fig. 3.9. Computed velocity fields for (a) Cylindrical jet with zero slip, (b) Conical jet with zero slip.

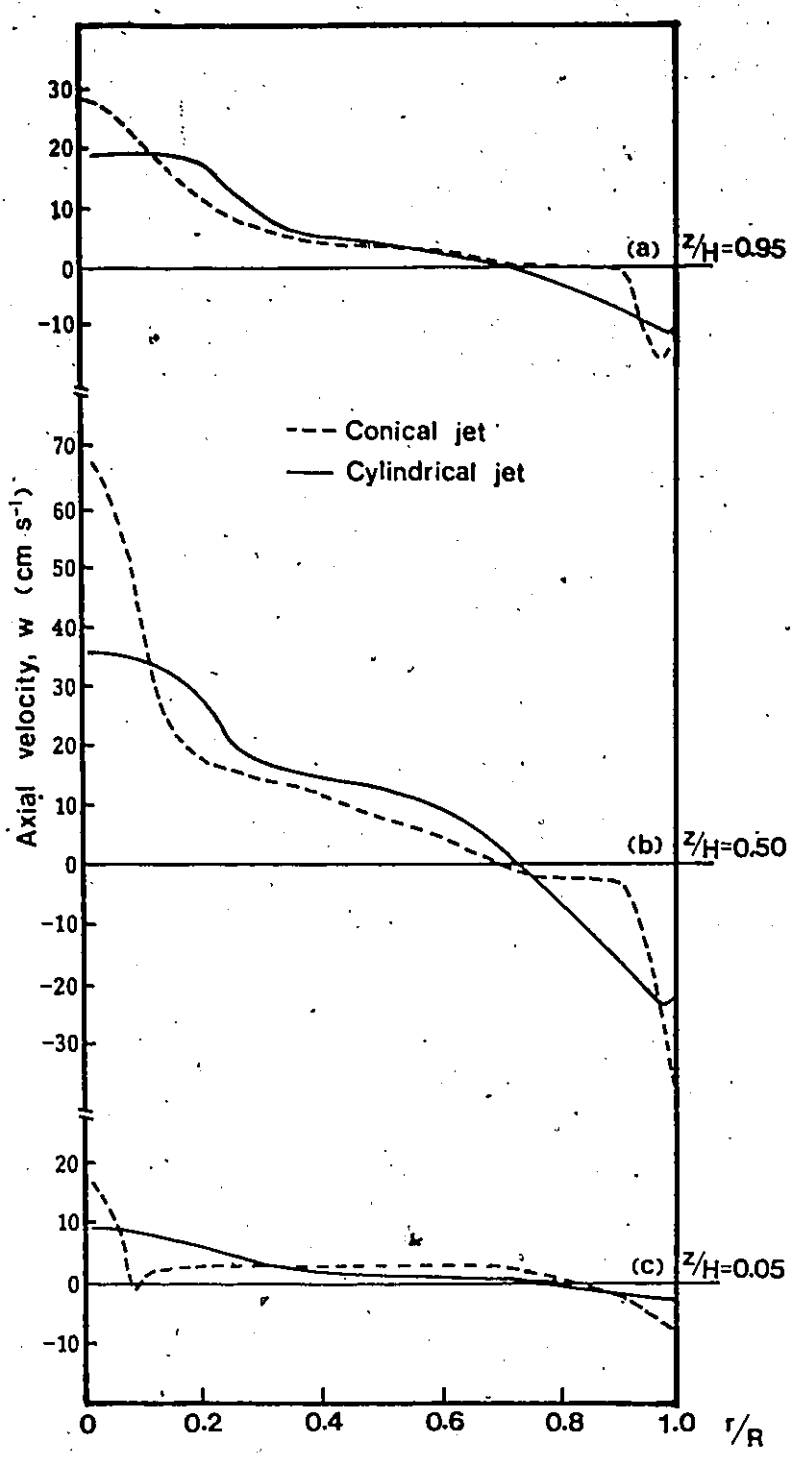

Fig. 3.10. Comparison of predicted axial velocity distribution between a cylindrical and a conical jet at different values of z/H.

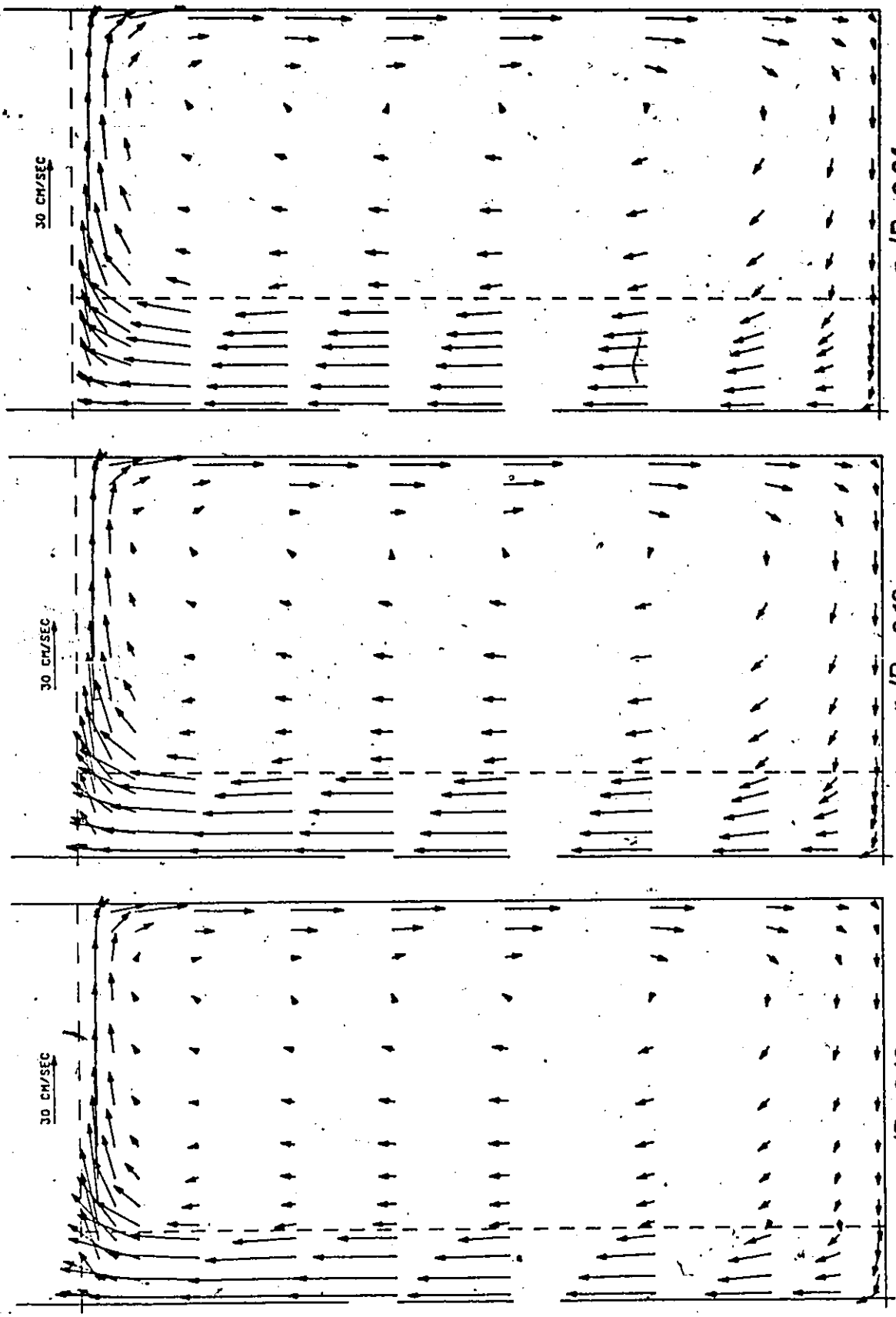

Fig. 3.11. Predicted velocity fields for different values of r_c/R at time = 10.0 sec. after jetting.

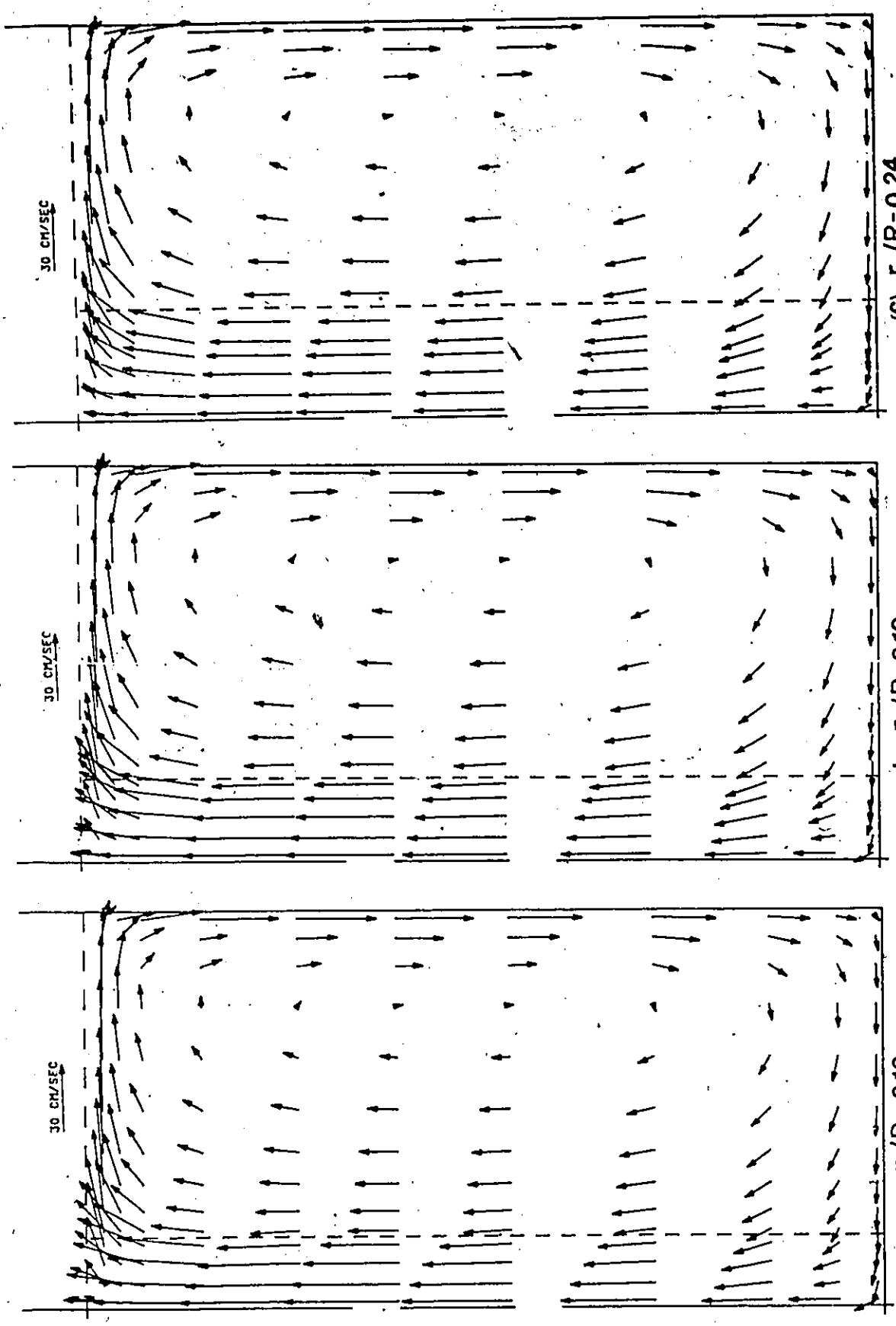

Fig. 3.12. Predicted velocity fields for different values of r_c/R at time = 40.0 sec. after jetting.

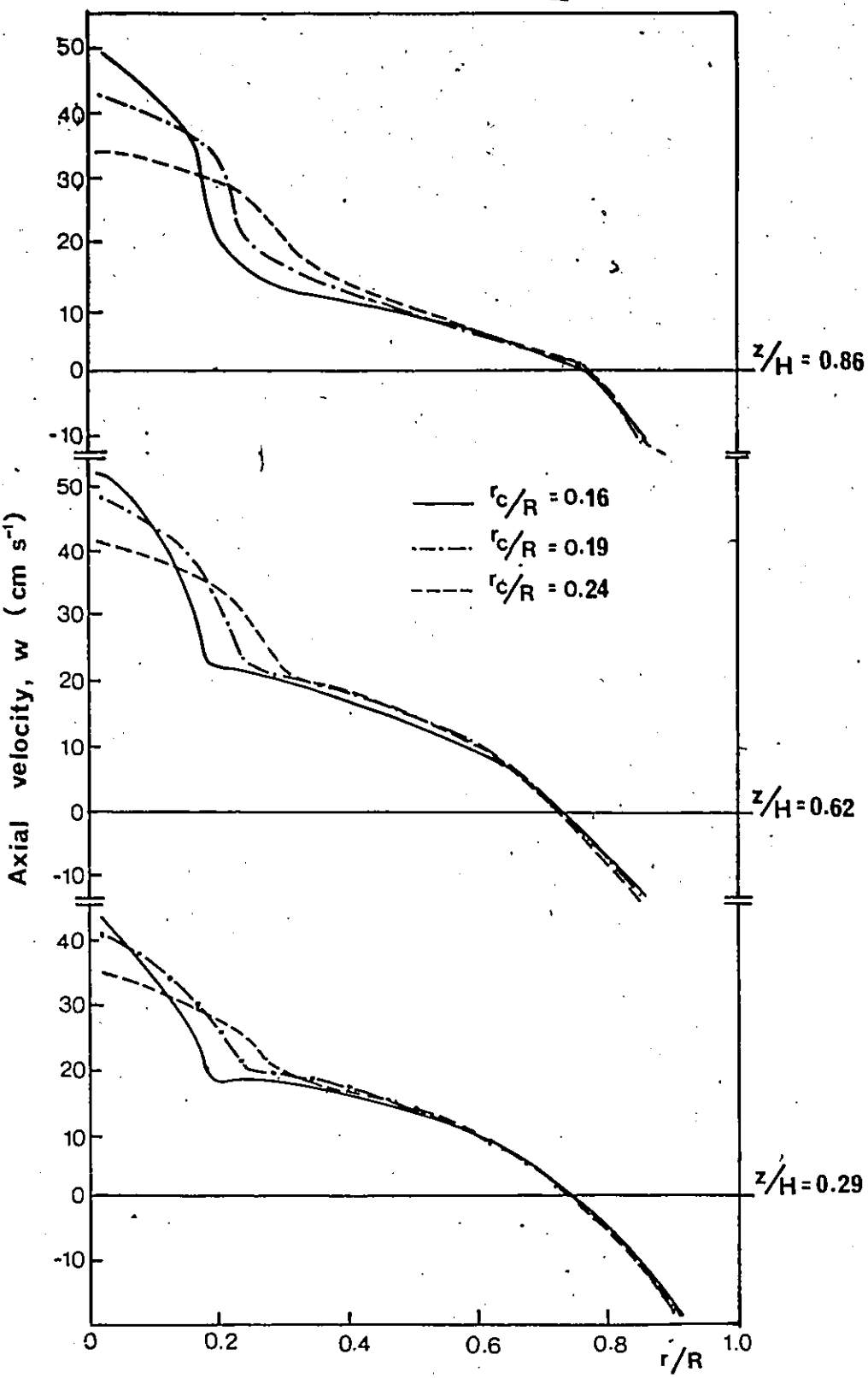

Fig. 3.13. Quantitative comparison of the predicted axial velocity distribution at different values of z/H.

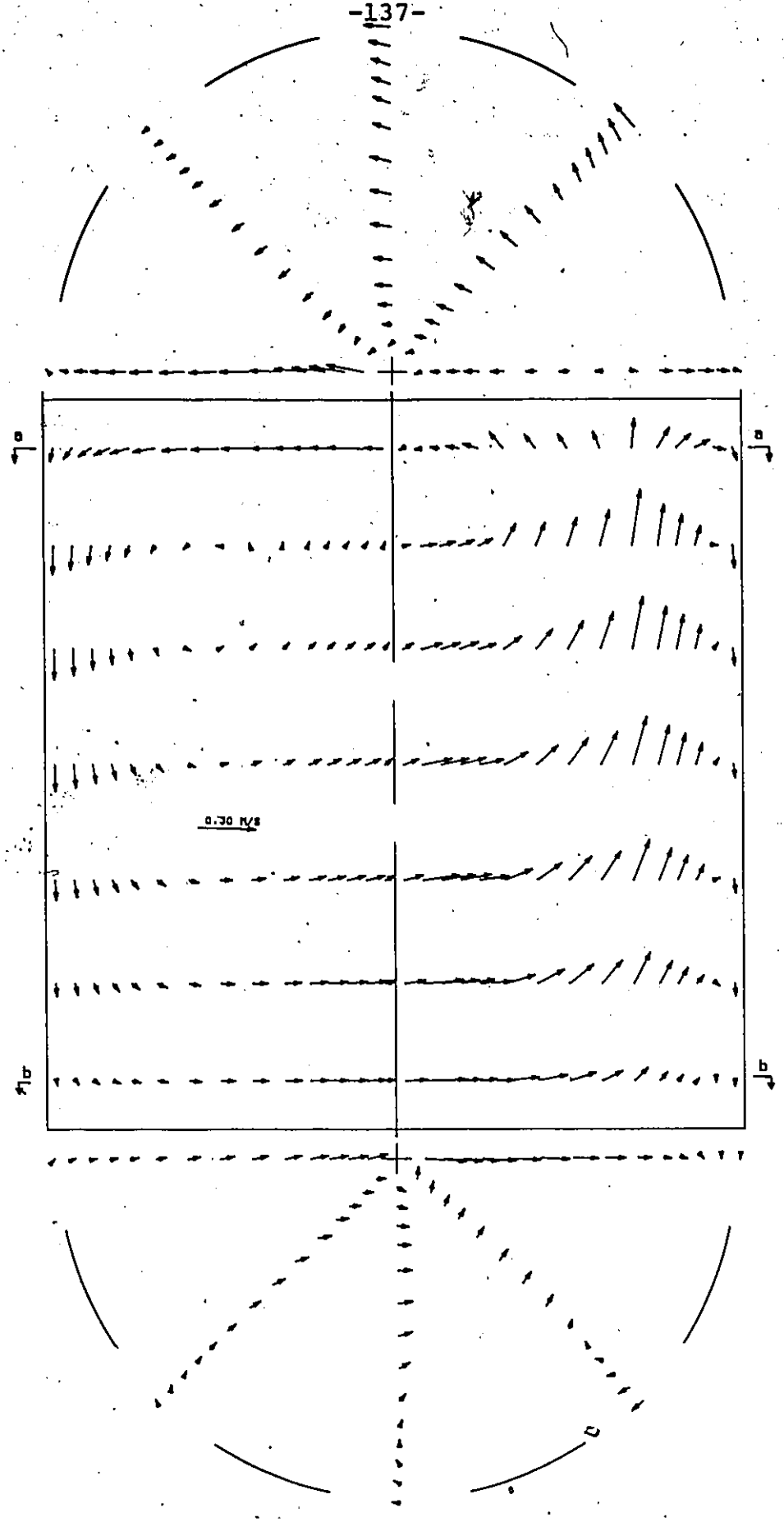

Fig. 3.14. Vertical and horizontal views of the velocity fields for a jet entering the vessel at 3/4-distance between the center and the wall.

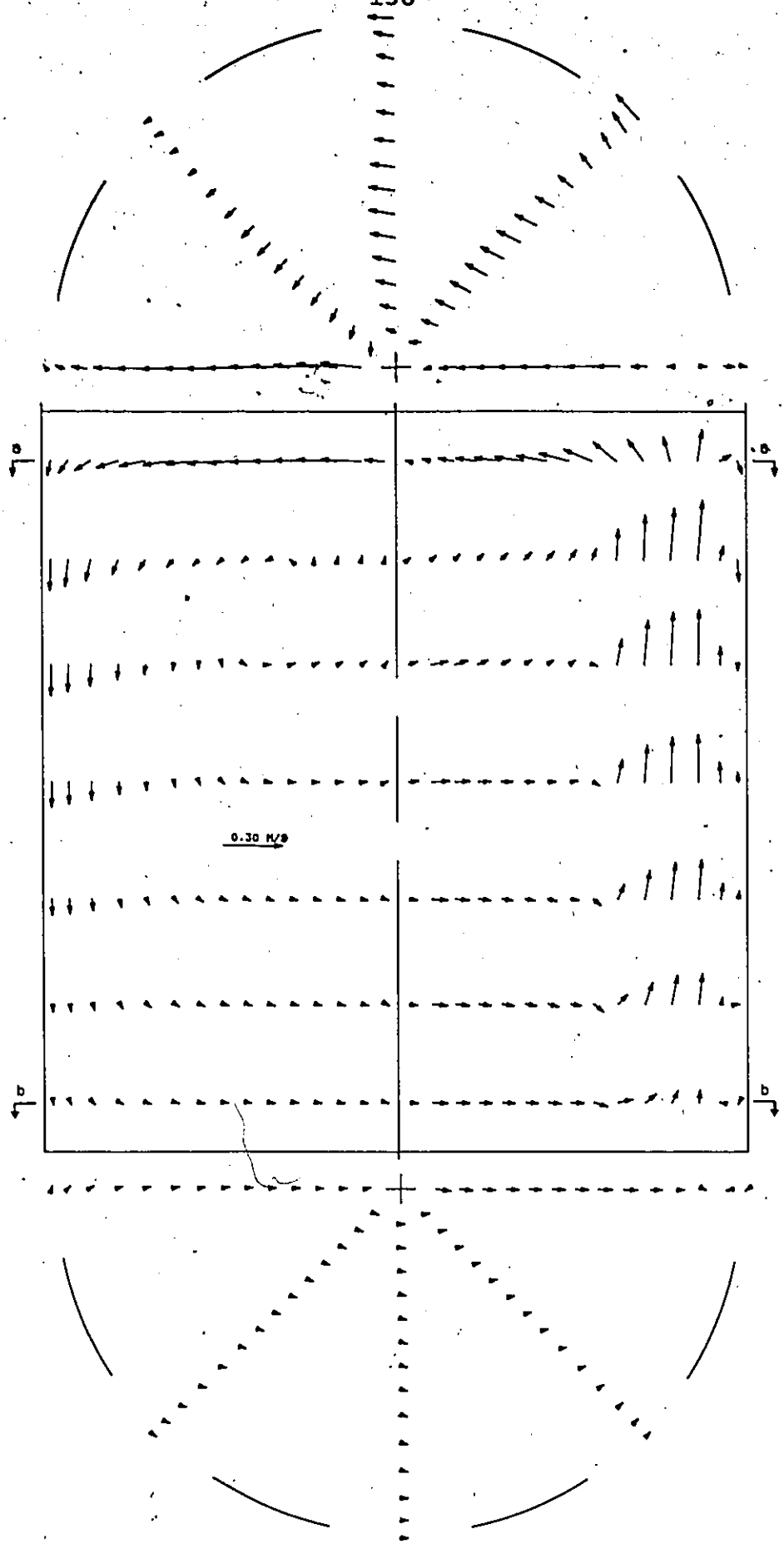

Fig. 3.15. Vertical and horizontal views of the velocity fields for a jet entering the vessel near the side wall.

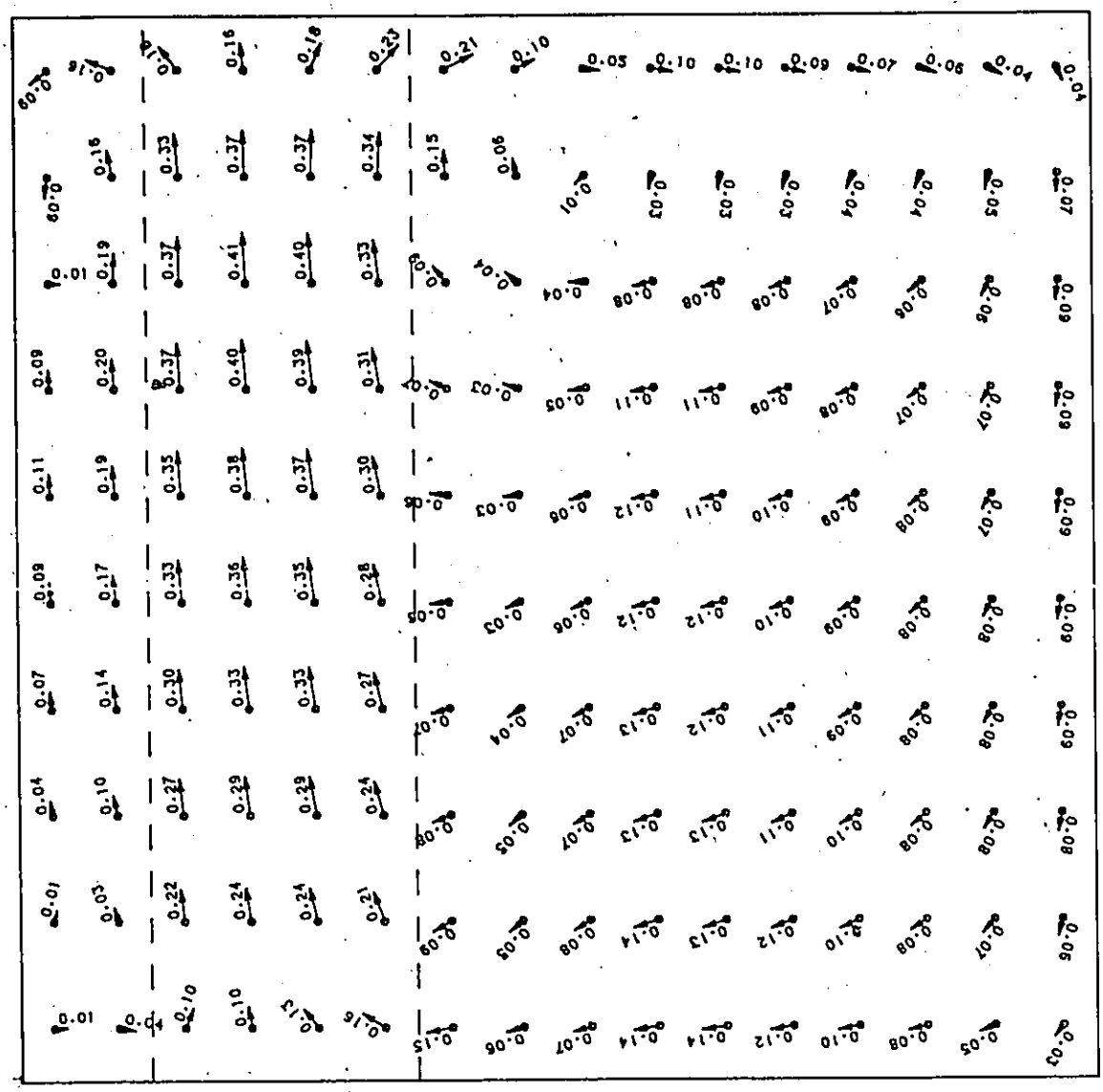

Fig. 3.16. Predicted velocity field for off-centered jet by Wong [69].

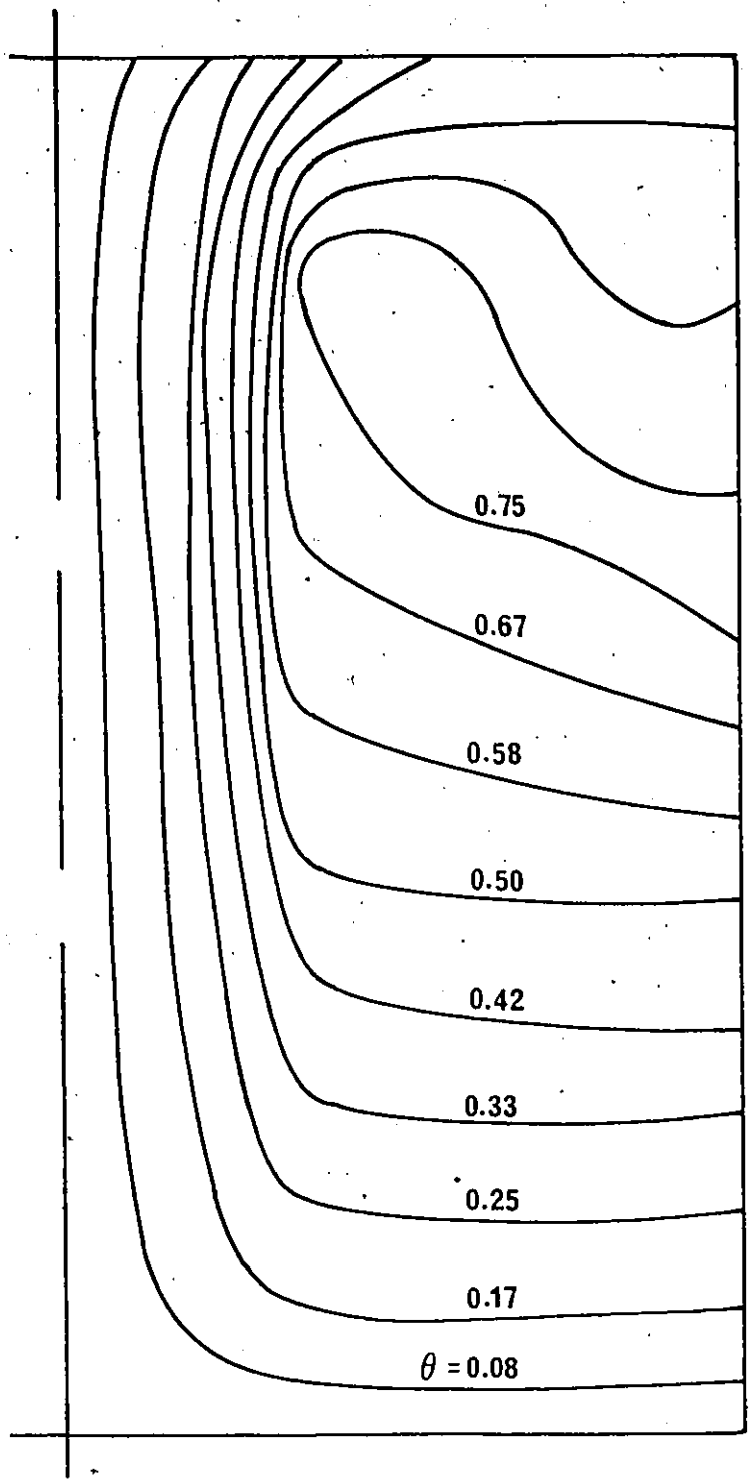

Fig. 3.17. Non-dimensional temperature distribution at time = 5.0 sec. after jetting.

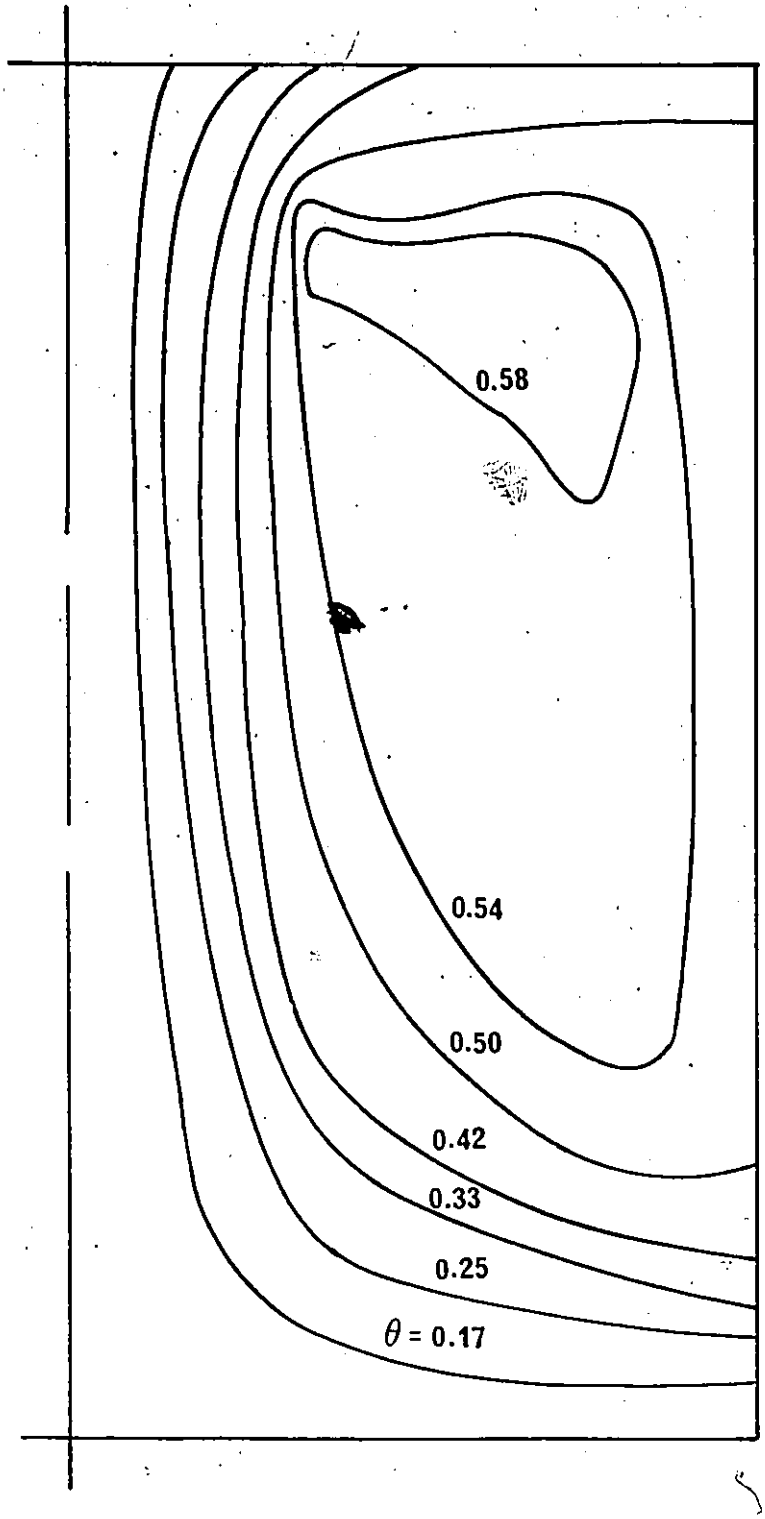

Fig. 3.18. Non-dimensional temperature distribution at time = 12.5 sec. after jetting.

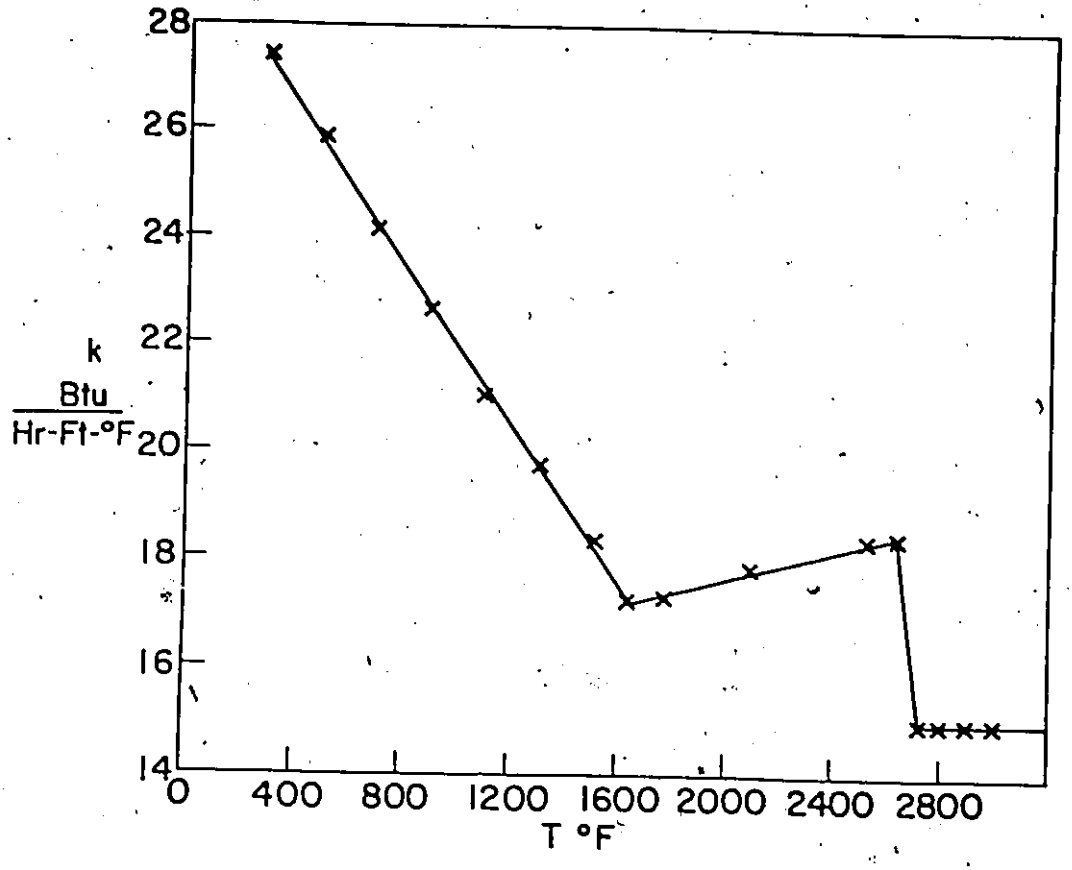

Fig. 4.1. Correlations for the thermal conductivity of Low-Carbon Steel [48].

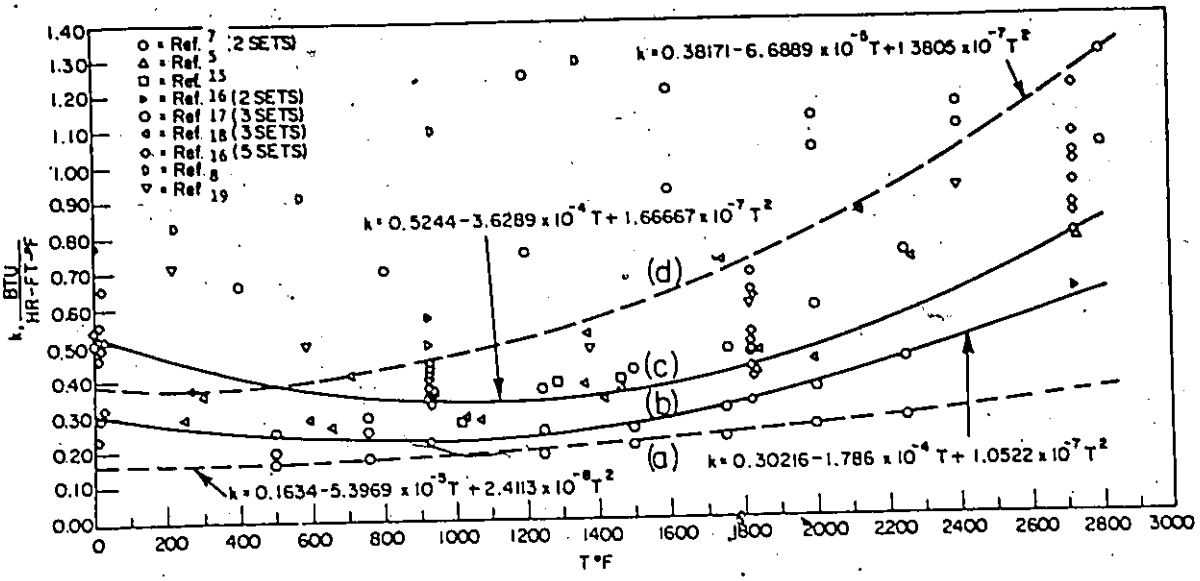

Fig. 4.2. Functional relationships for thermal conductivity of molding sand [48].

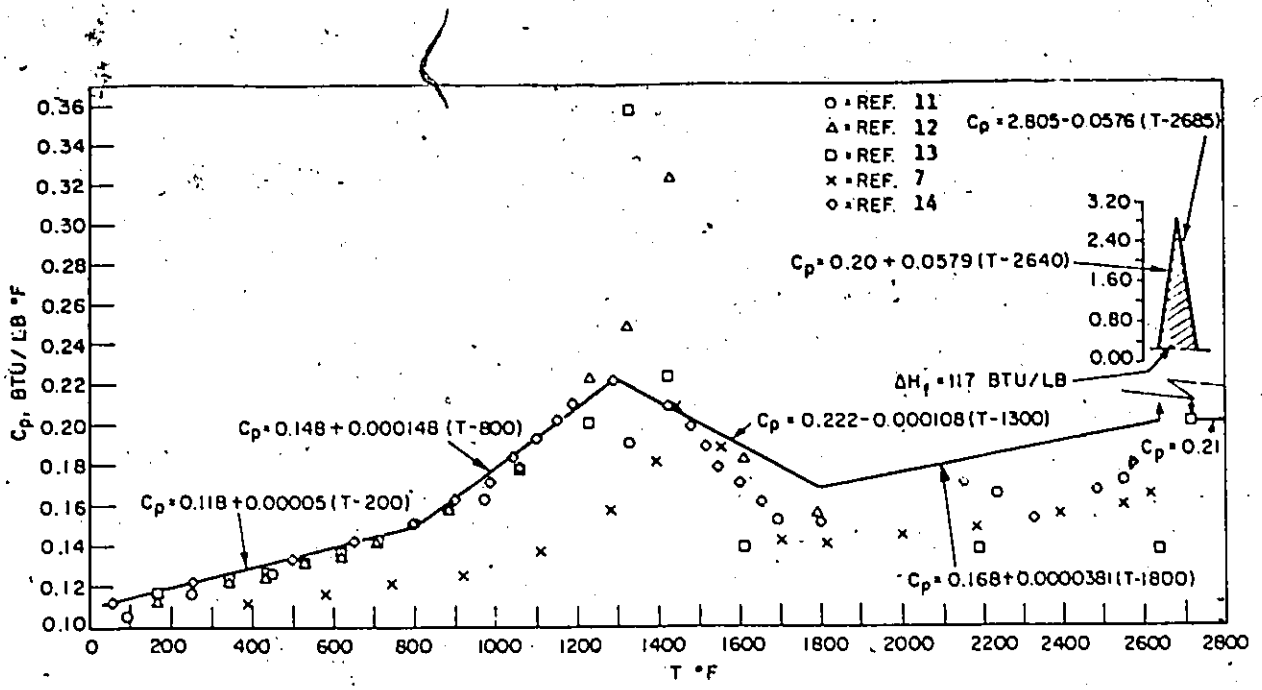

Fig. 4.3. Selected data and functional relationships for specific heat of Low Carbon Steel, including the latent heat approximation [48].

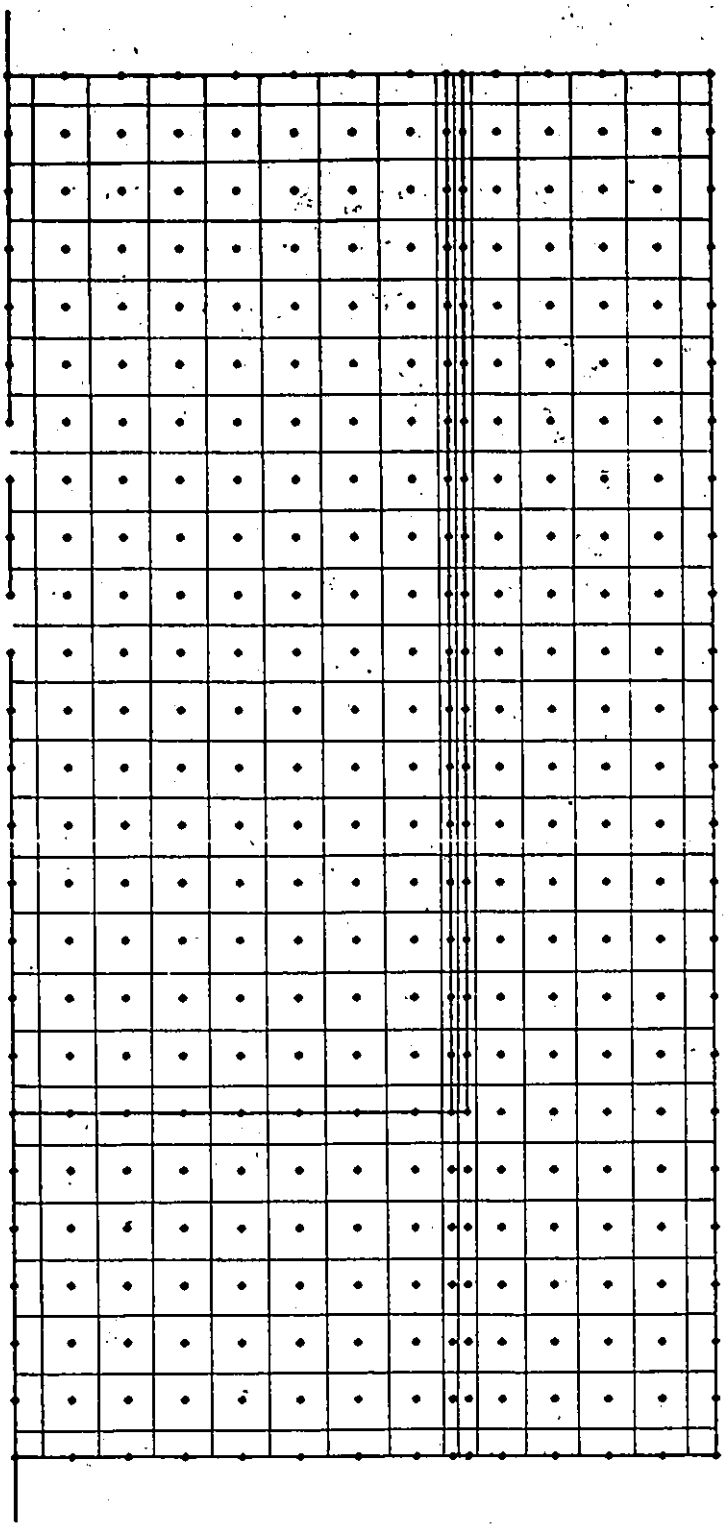

Fig. 4.4. Arrangement of grid points.

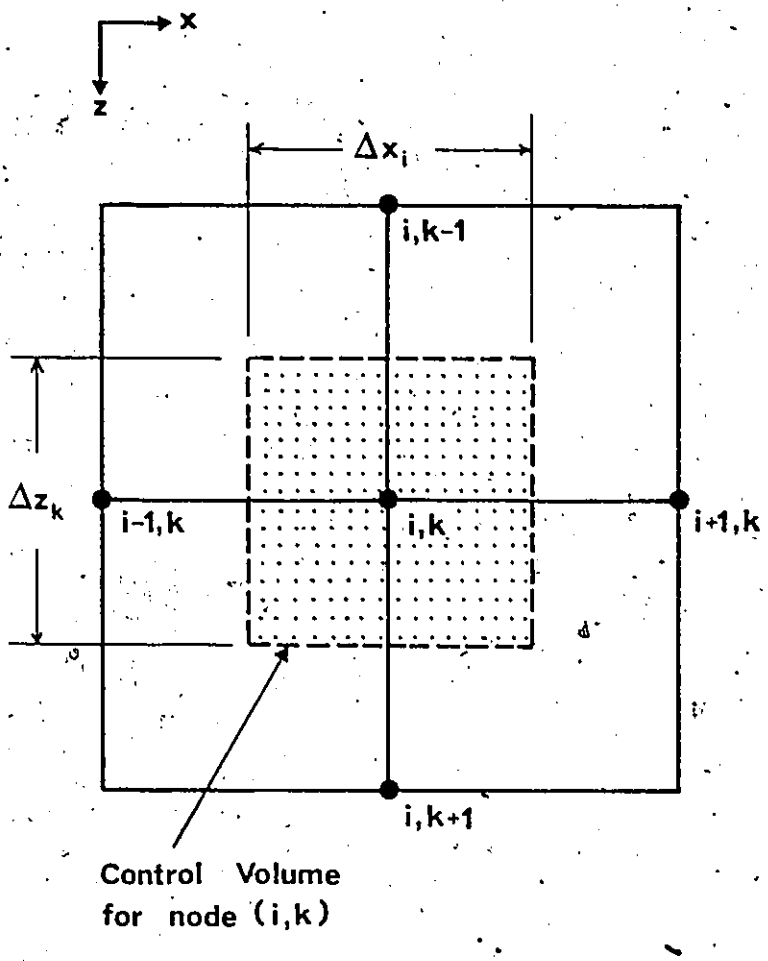

Fig. 4.5. Typical internal node for the two-dimensional situation.

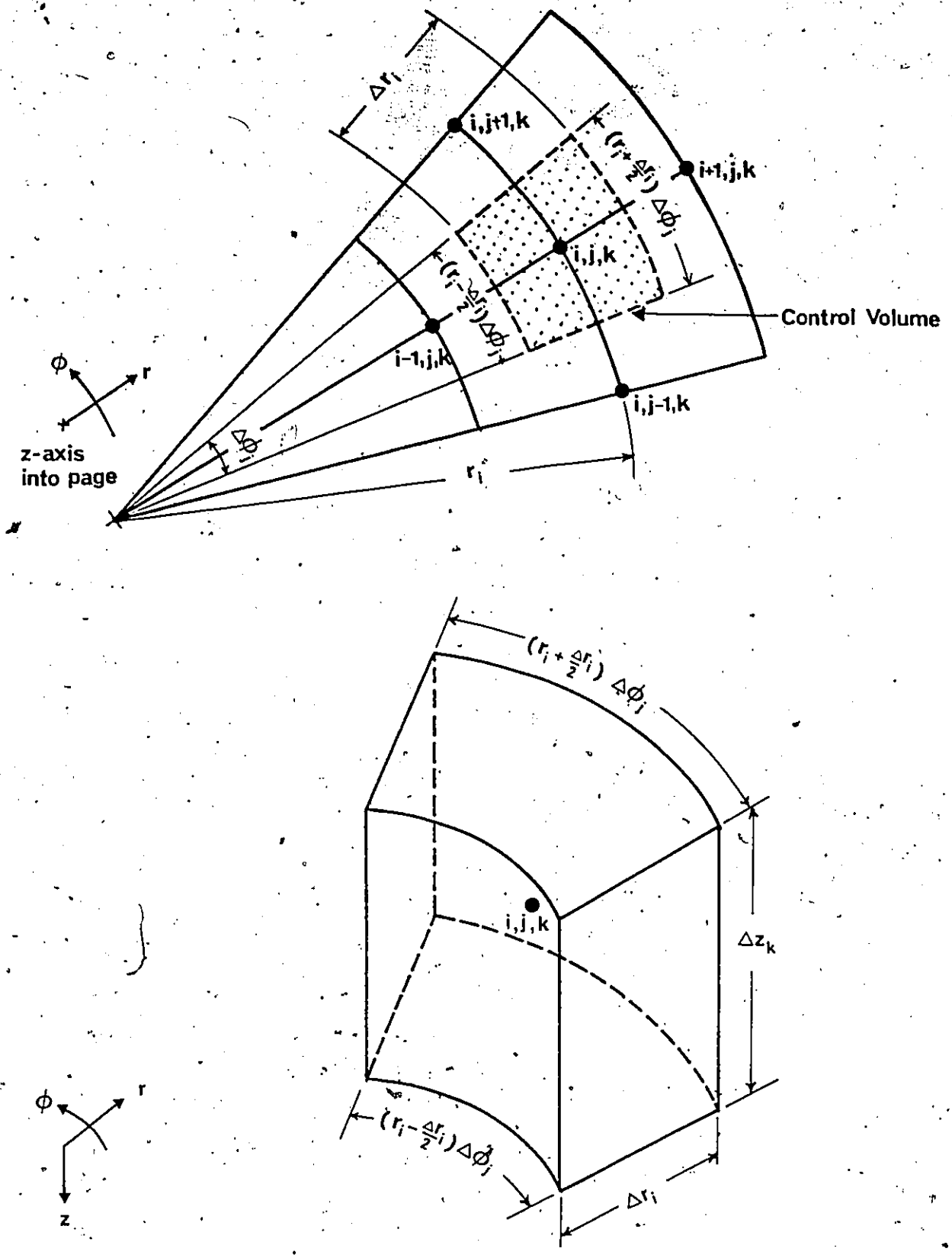

Fig. 4.6. Control volume of an internal node in cylindrical coordinates.

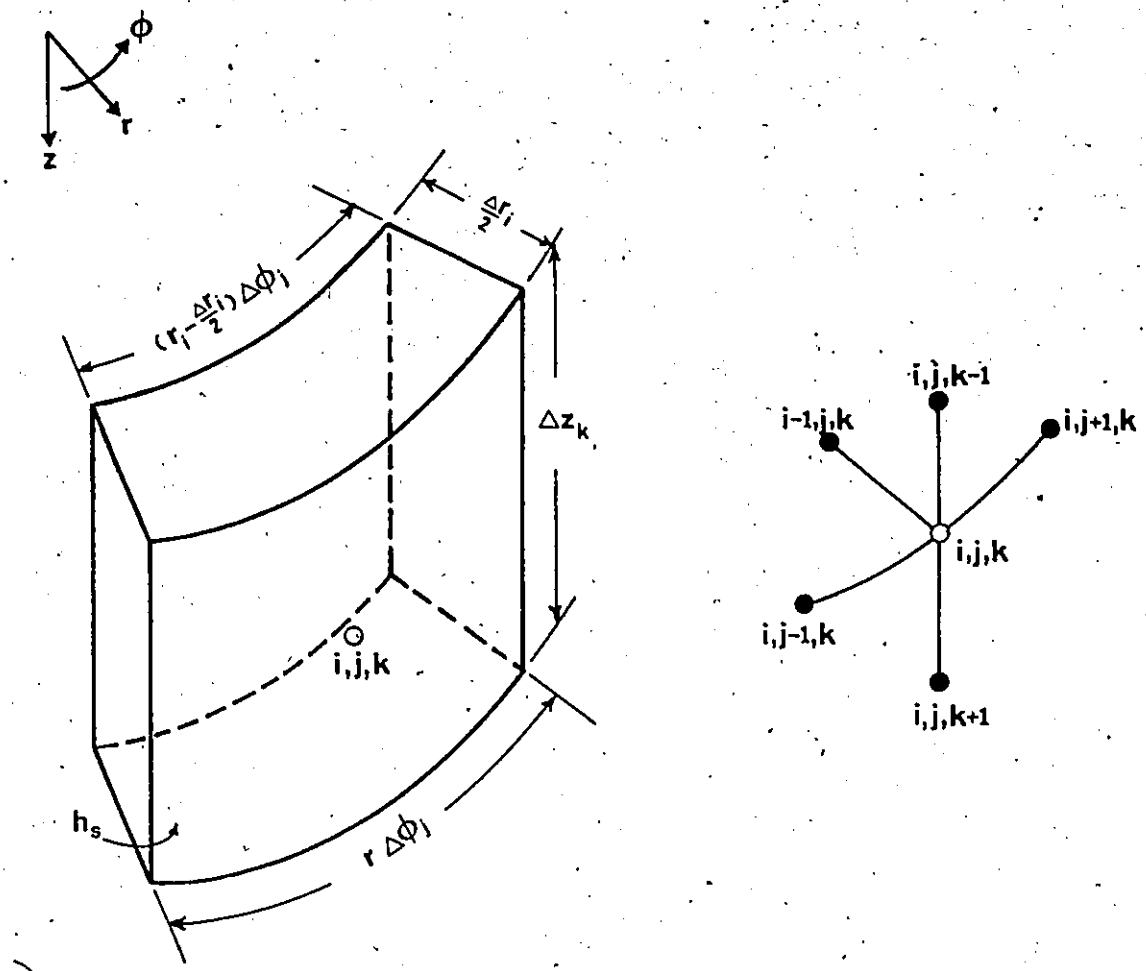

Fig. 4.7. Control volume for a typical side boundary node.

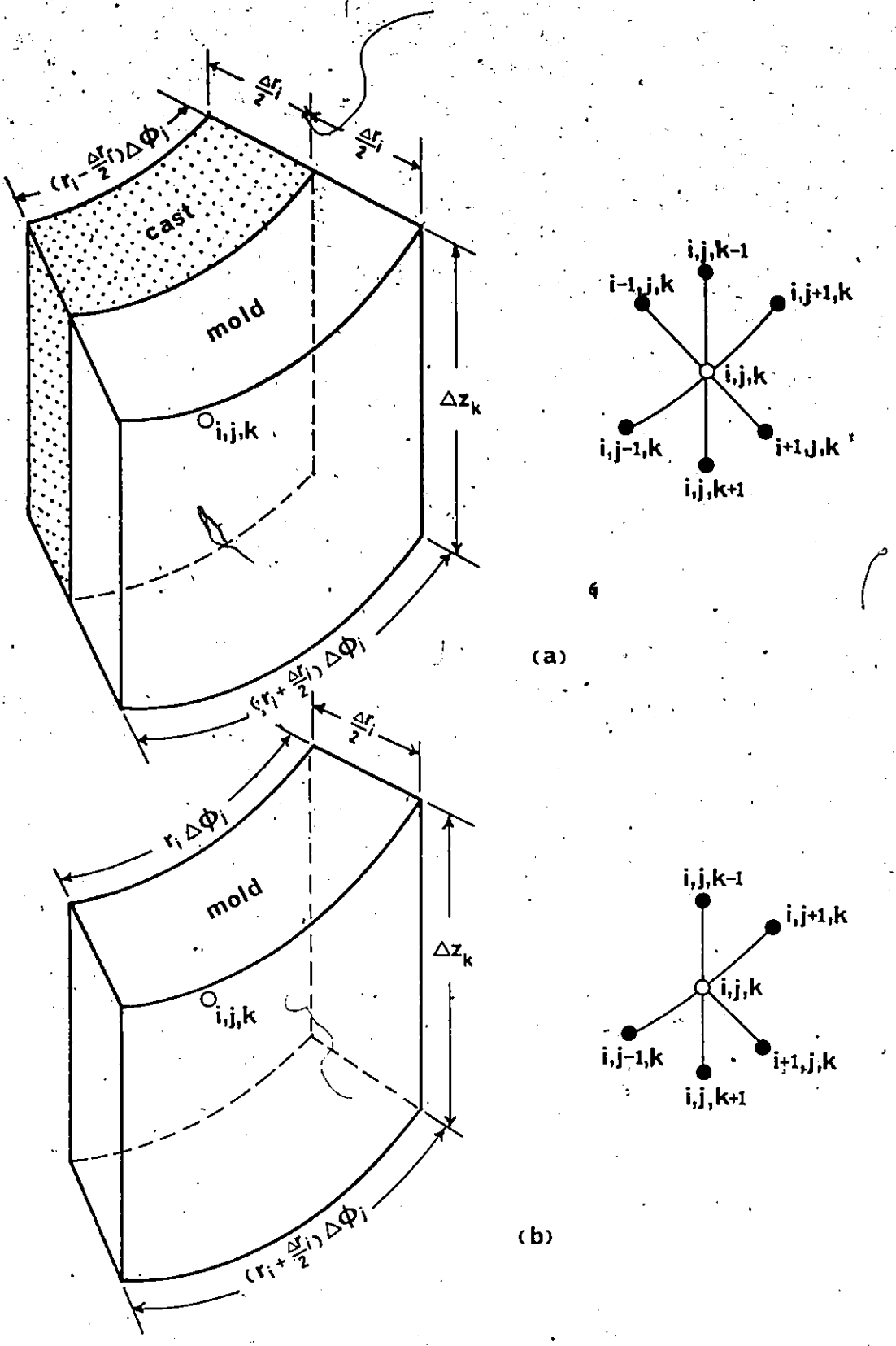

Fig. 4.8. Control volume for an interface node (a) before and (b) after the air-gap formation.

9	5	5	5	5	5	5	5	17	14	5	5	5	5	6
7	1	1	1	1	1	1	1	15	11	1	1	1	1	2
7	1	1	1	1	1	1	1	15	11	1	1	1	1	2
7	1	1	1	1	1	1	1	15	11	1	1	1	1	2
7	1	1	1	1	1	1	1	15	11	1	1	1	1	2
7	1	1	1	1	1	1	1	15	11	1	1	1	1	2
7	1	1	1	1	1	1	1	15	11	1	1	1	1	2
7	1	1	1	1	1	1	1	15	11	1	1	1	1	2
7	1	1	1	1	1	1	1	15	11	1	1	1	1	2
7	1	1	1	1	1	1	1	15	11	1	1	1	1	2
7	1	1	1	1	1	1	1	15	11	1	1	1	1	2
7	1	1	1	1	1	1	1	15	11	1	1	1	1	2
7	1	1	1	1	1	1	1	15	11	1	1	1	1	2
7	1	1	1	1	1	1	1	15	11	1	1	1	1	2
7	1	1	1	1	1	1	1	15	11	1	1	1	1	2
7	1	1	1	1	1	1	1	15	11	1	1	1	1	2
7	1	1	1	1	1	1	1	15	11	1	1	1	1	2
7	1	1	1	1	1	1	1	15	11	1	1	1	1	2
7	1	1	1	1	1	1	1	15	11	1	1	1	1	2
7	1	1	1	1	1	1	1	15	11	1	1	1	1	2
8	12	12	12	12	12	12	12	16	13	1	1	1	1	2
7	1	1	1	1	1	1	1	1	1	1	1	1	1	2
7	1	1	1	1	1	1	1	1	1	1	1	1	1	2
7	1	1	1	1	1	1	1	1	1	1	1	1	1	2
7	1	1	1	1	1	1	1	1	1	1	1	1	1	2
7	1	1	1	1	1	1	1	1	1	1	1	1	1	2
10	3	3	3	3	3	3	3	3	3	3	3	3	3	4

Fig. 4.9. Node numbers indicating the type of nodes in the grid arrangement.

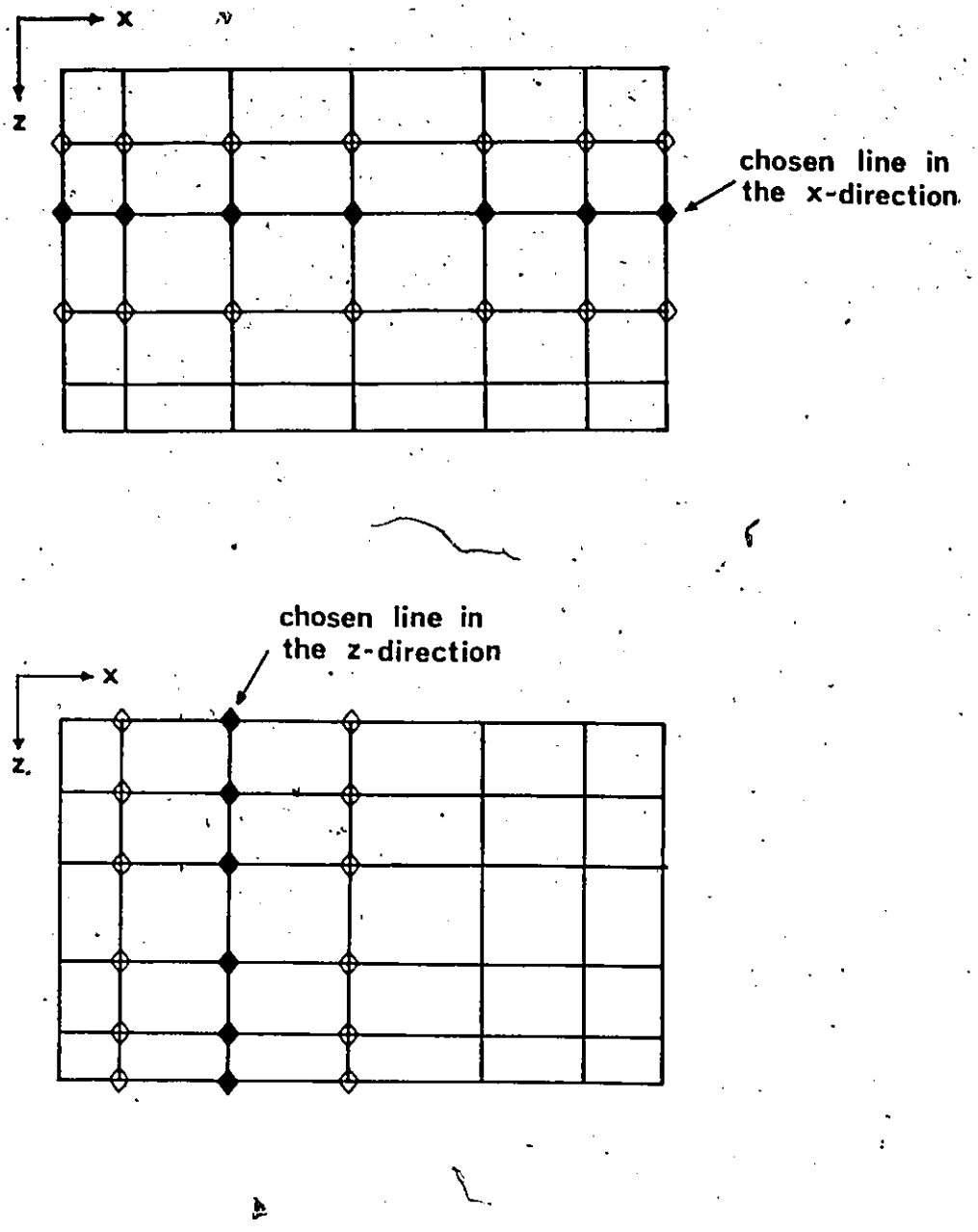

Fig. 4.10. Illustration of line-by-line iteration used in the ADI scheme.

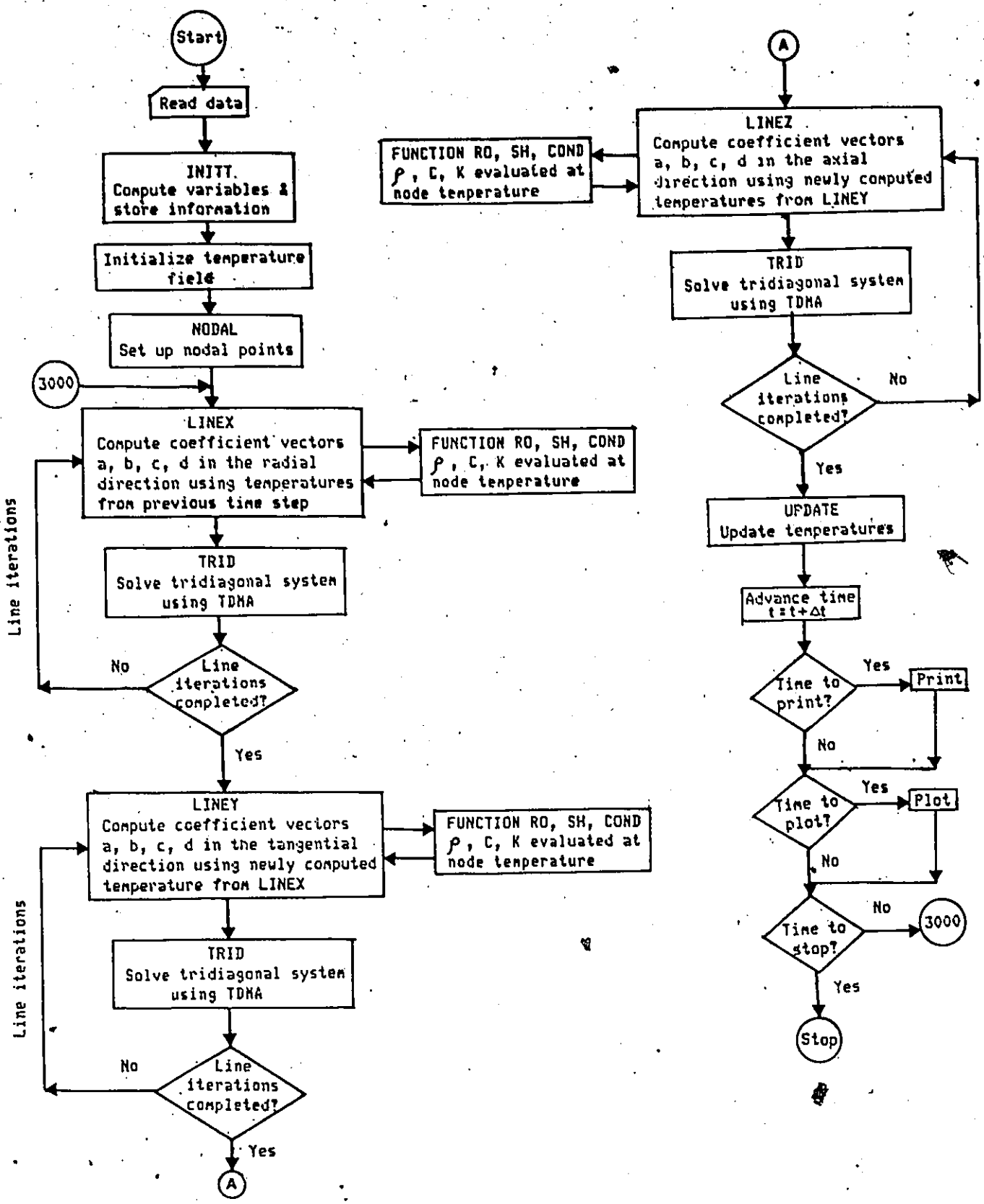

Fig. 4.11. Flow chart for solidification modelling.

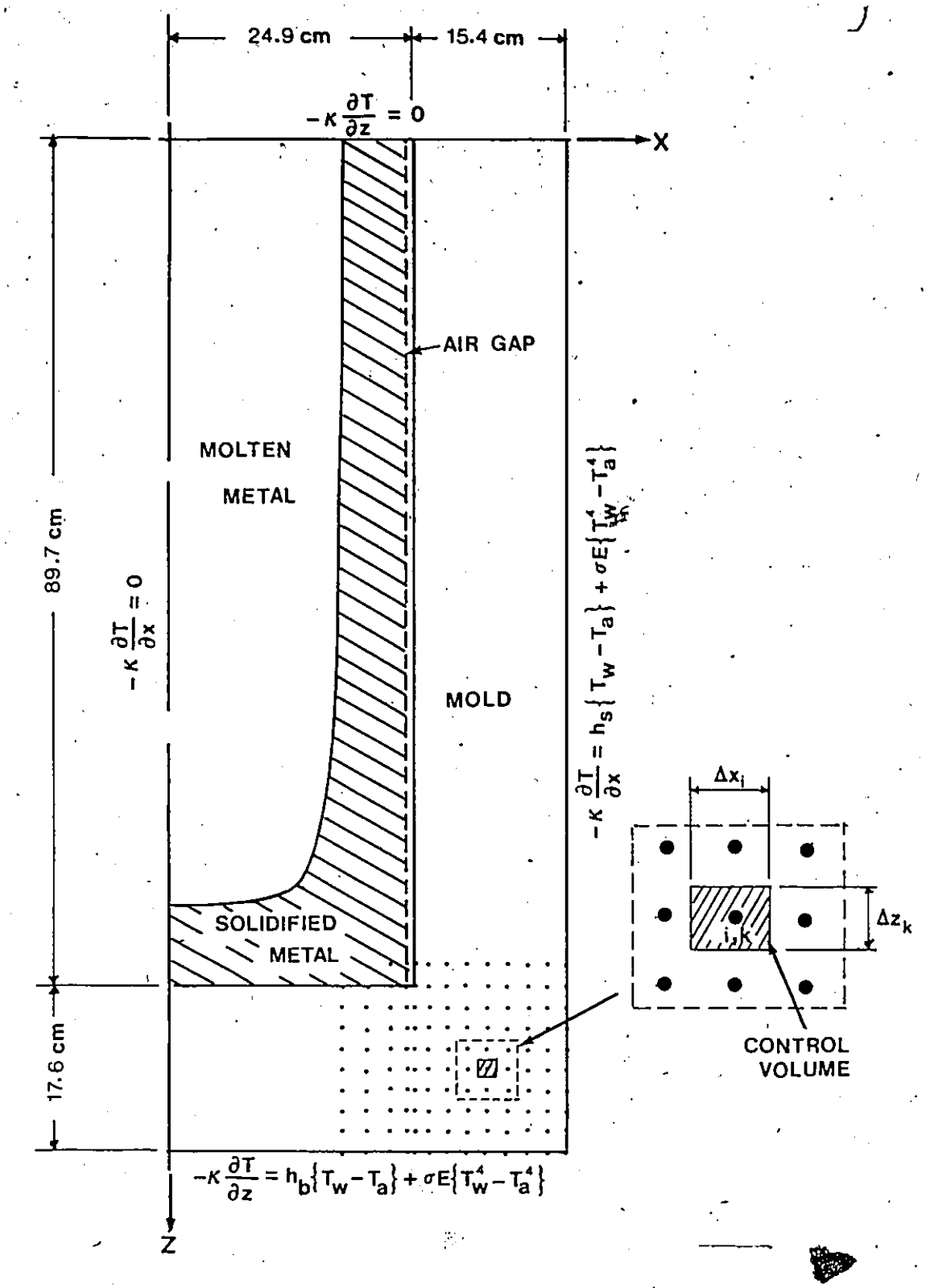

Fig. 4.12. Finite difference grid and boundary conditions.

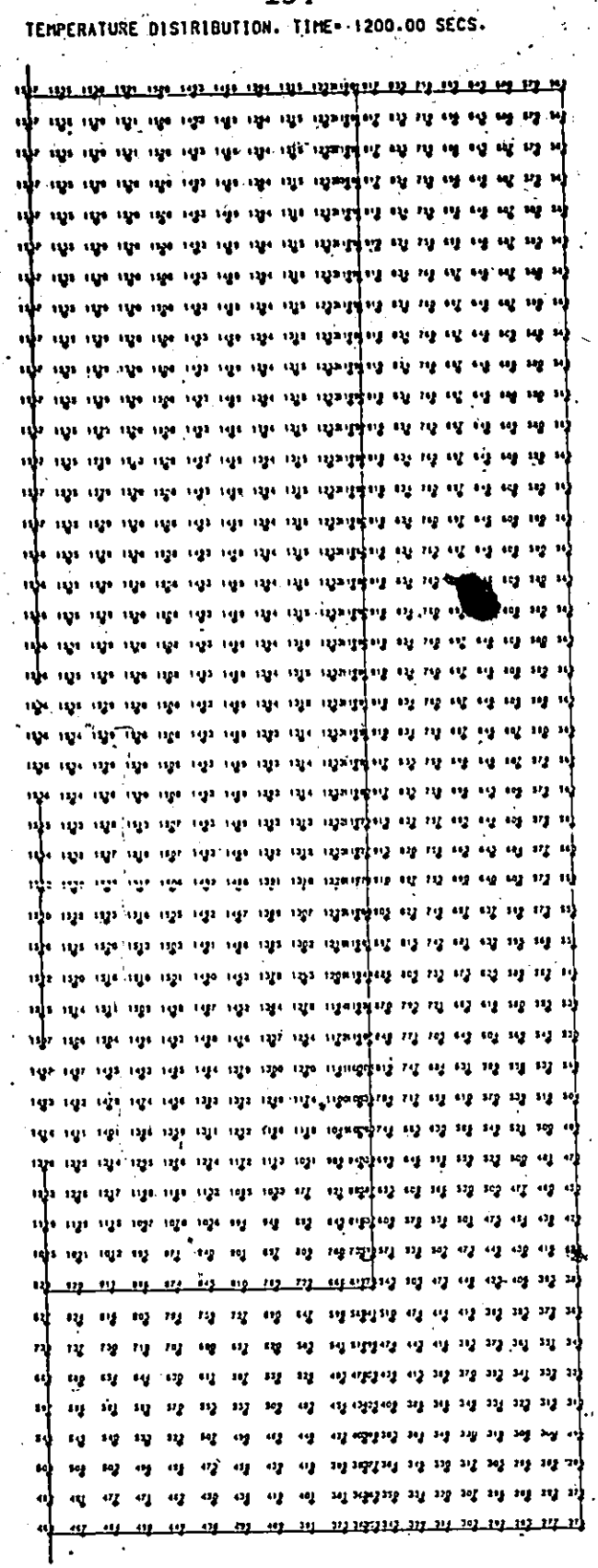

Fig. 4.13. Temperature distribution at time = 20 min.

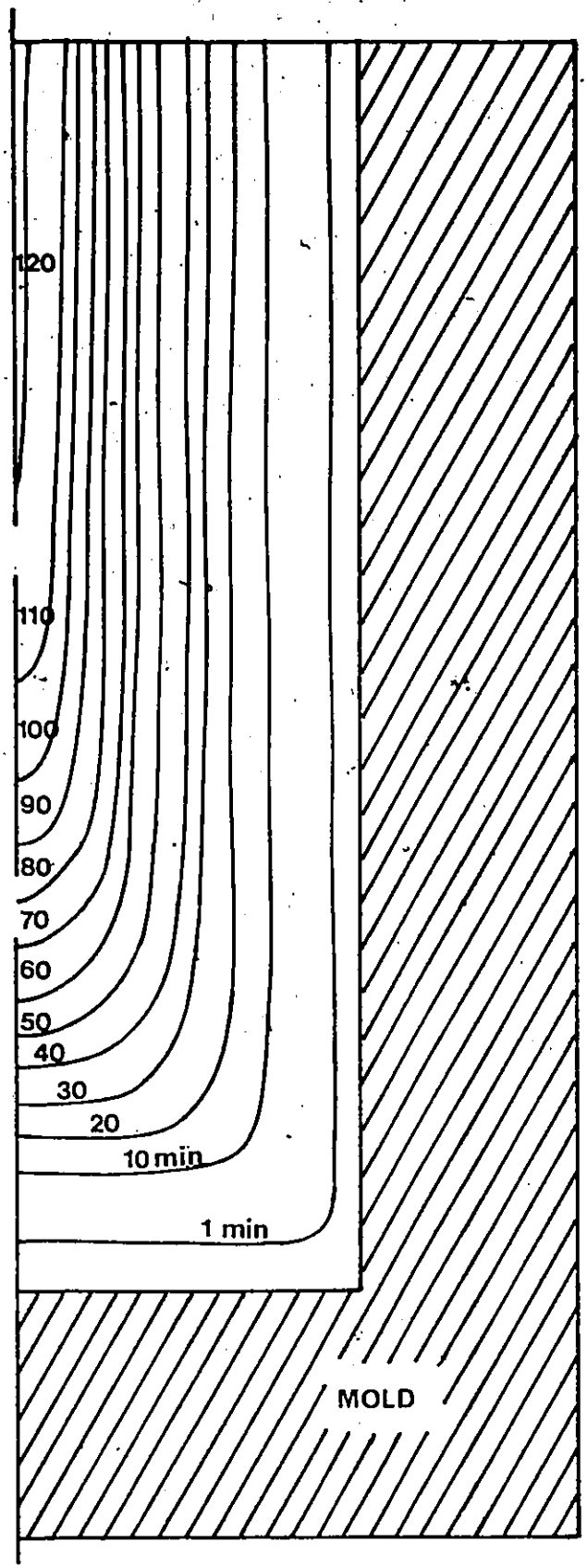

Fig. 4.14. Advancement of solidification front in a rectangular ingot.

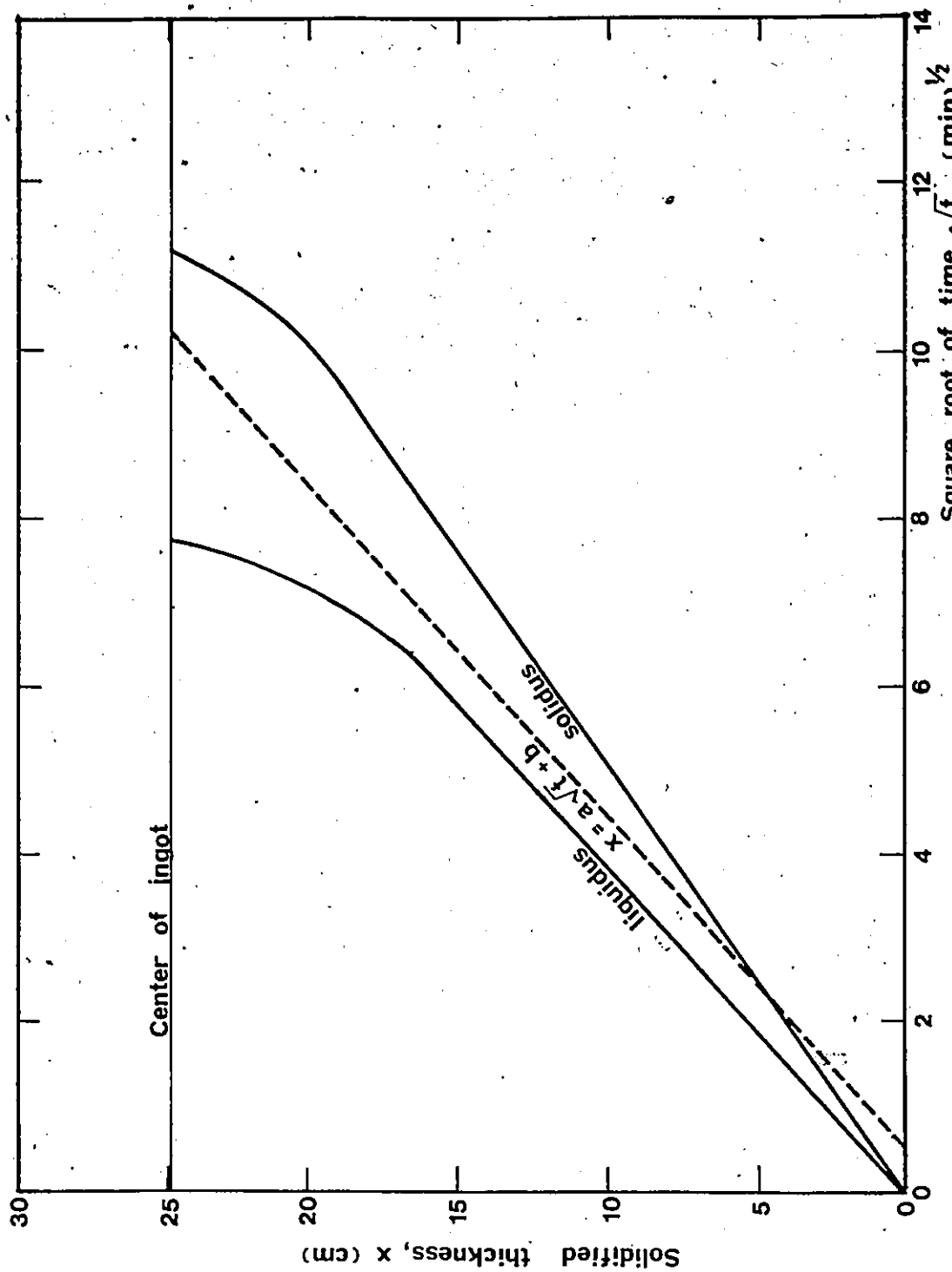

Fig. 4.15. Progress of liquidus and solidus isotherms with the square root of time for a rectangular ingot.

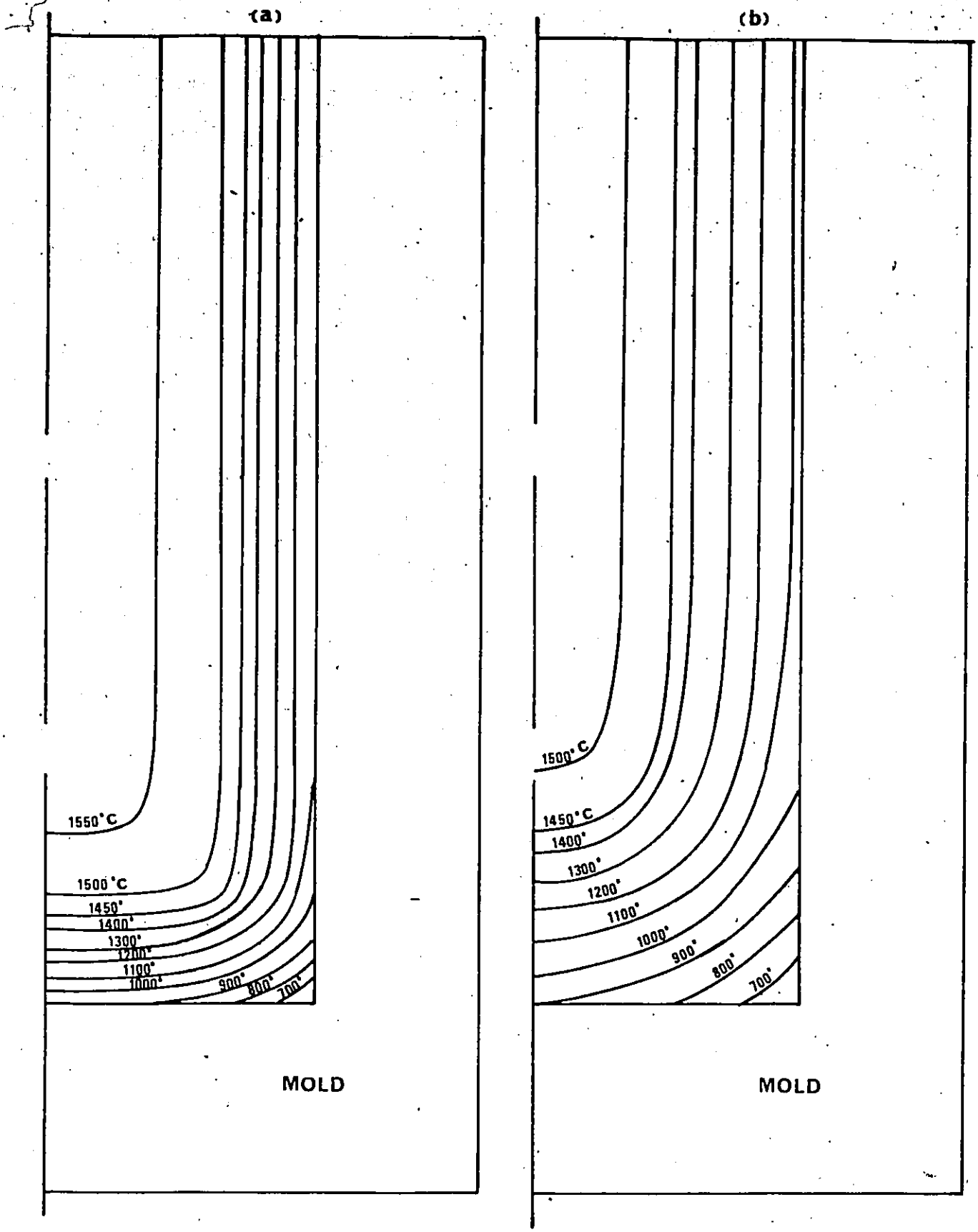

Fig. 4.16. Isotherms in the rectangular ingot at (a) time = 10.0 min. and (b) time = 40.0 min. after pouring.

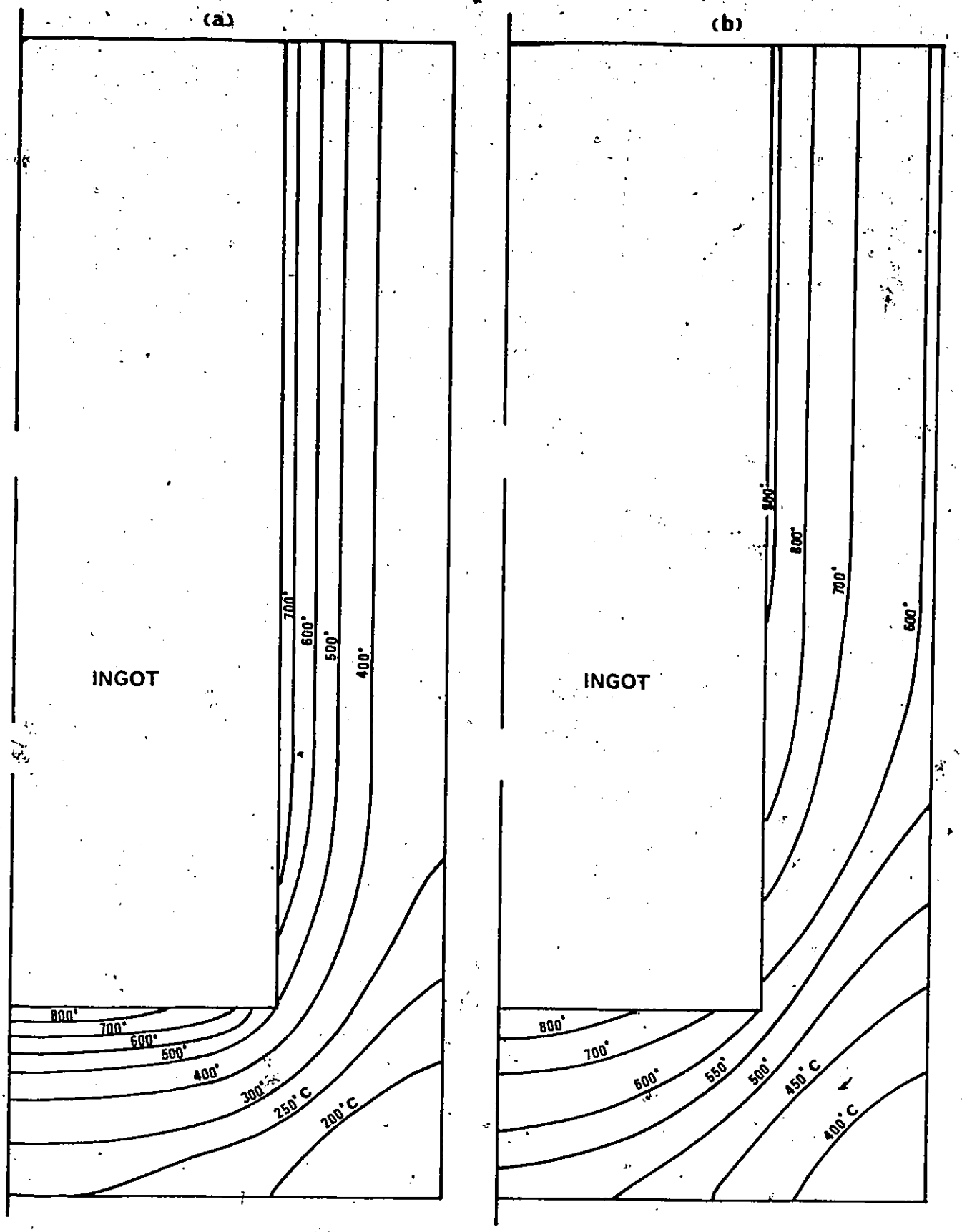

Fig. 4.17. Isotherms in the rectangular mold at (a) time = 10.0 min. and (b) time = 40.0 min. after pouring.

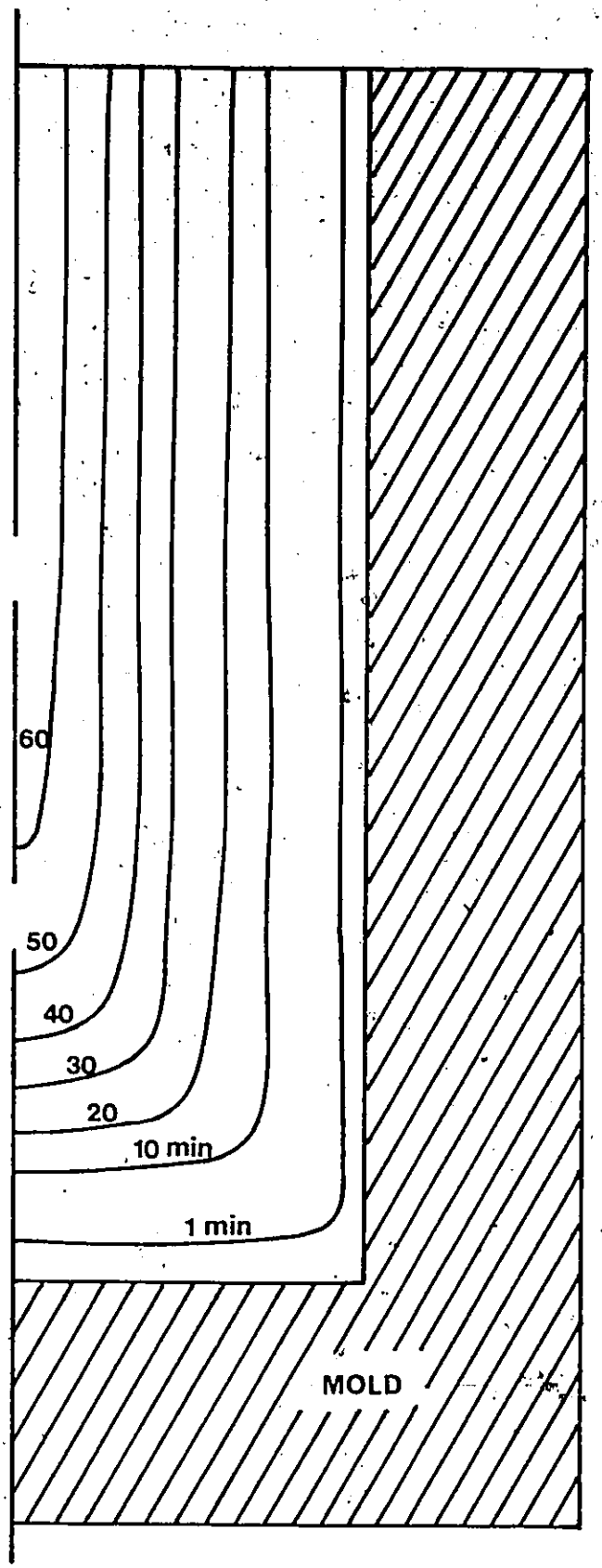

Fig. 4.18. Advancement of solidification front in a cylindrical ingot.

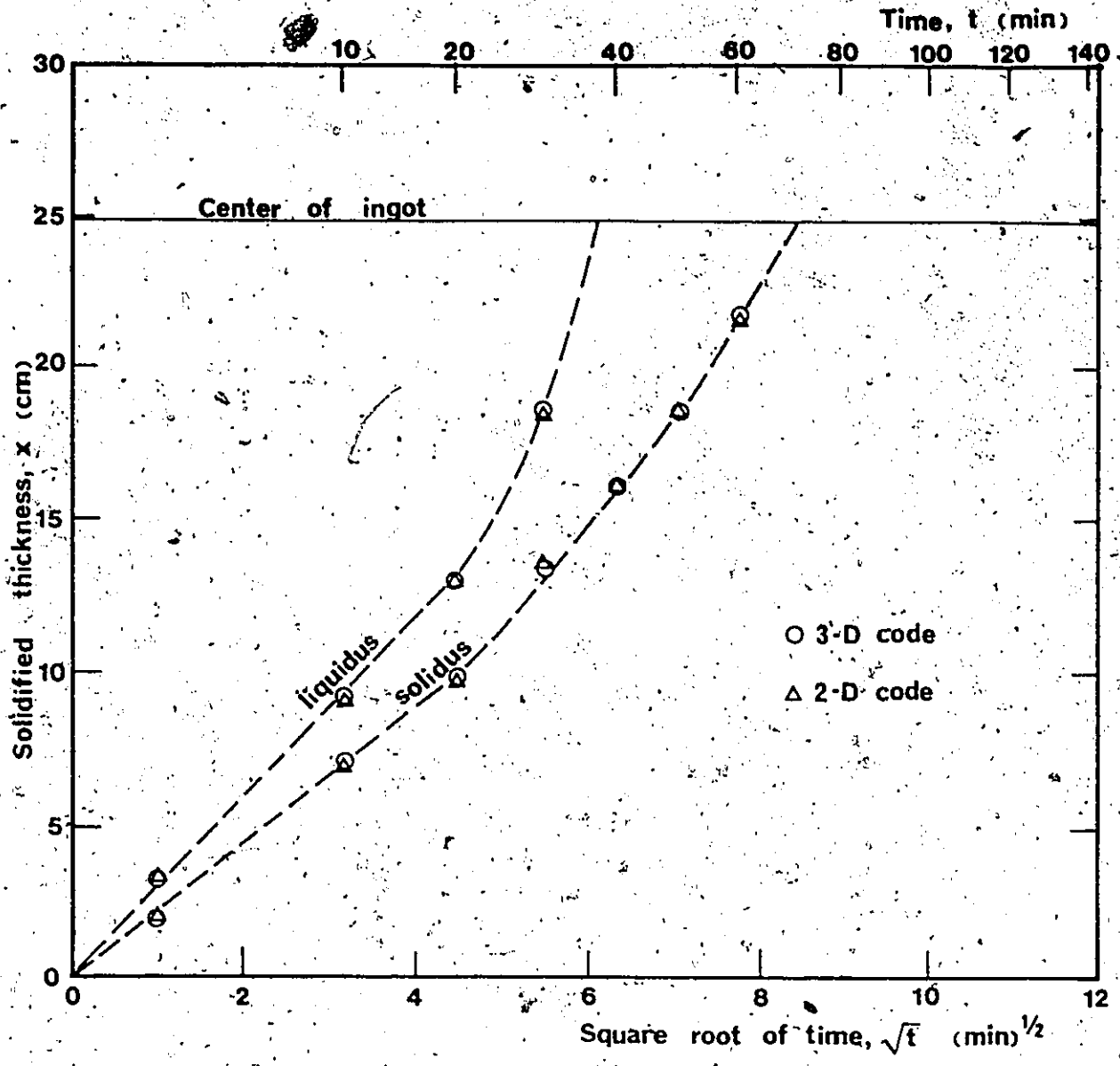

Fig. 4.19. Progress of liquidus and solidus isotherms with the square root of time for a cylindrical ingot.

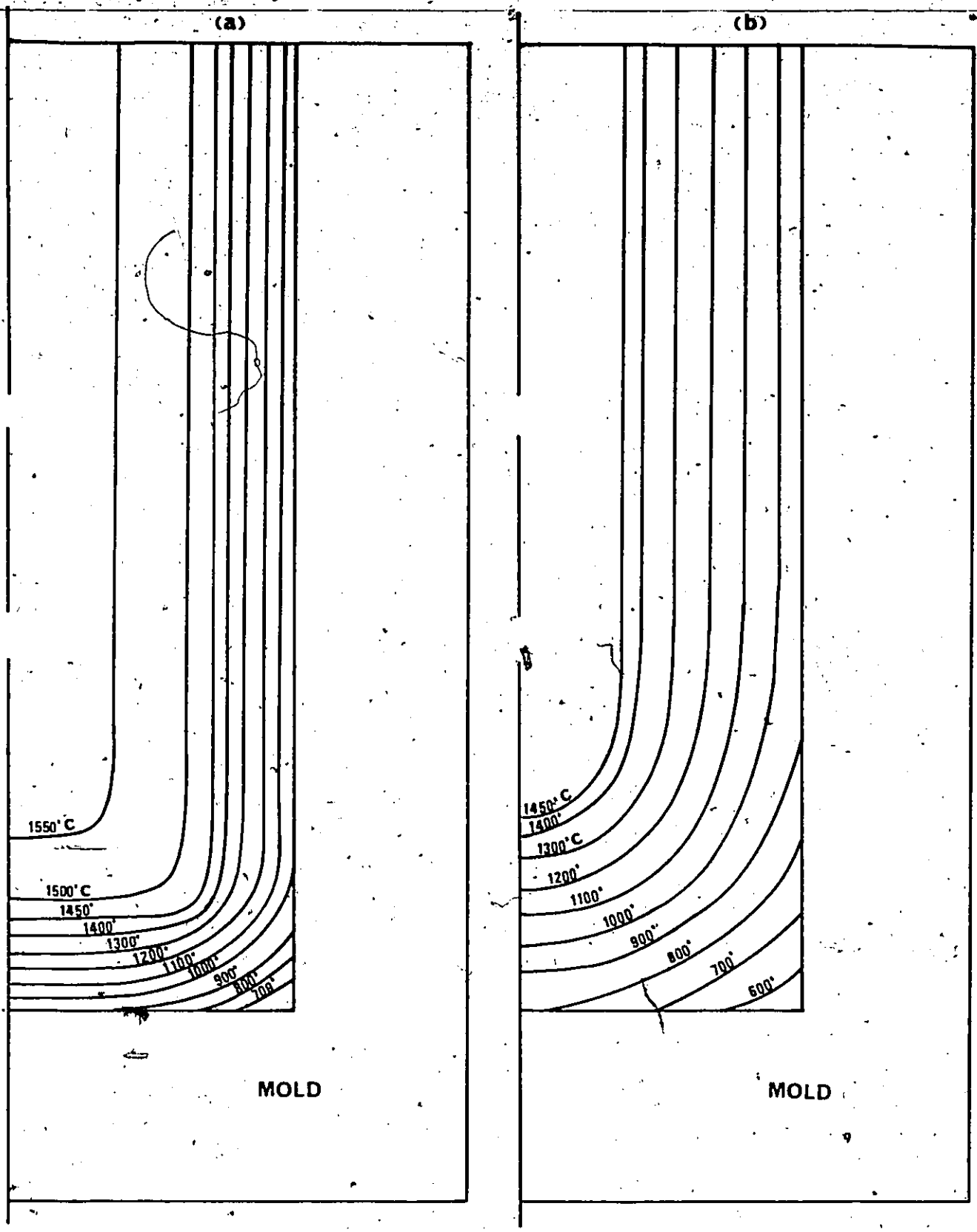

Fig. 4.20. Isotherms in the cylindrical ingot at (a) time = 10.0 min. and (b) time = 40.0 min. after pouring.

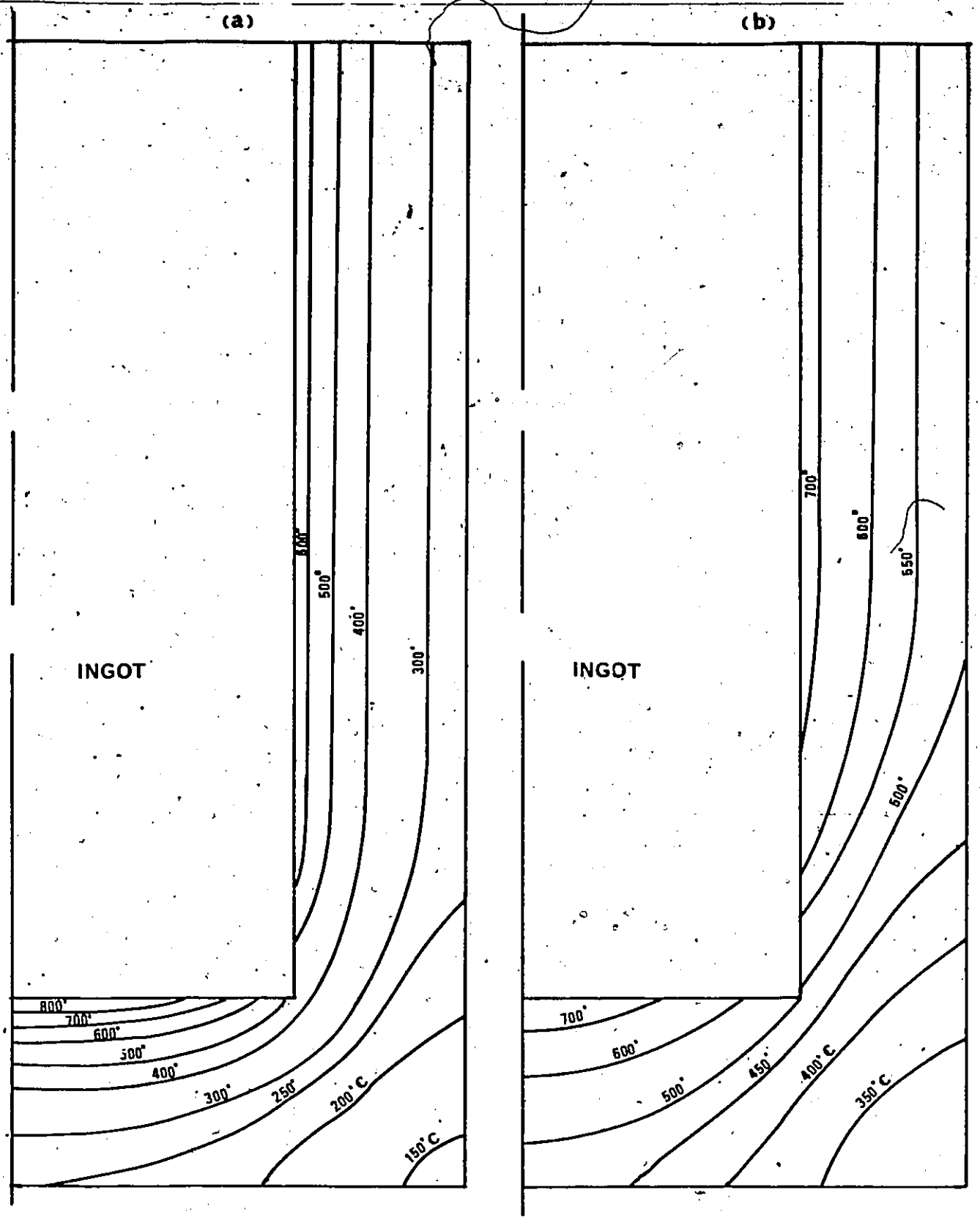

Fig. 4.21. Isotherms in the cylindrical mold at (a) time = 10.0 min. and (b) time = 40.0 min. after pouring.

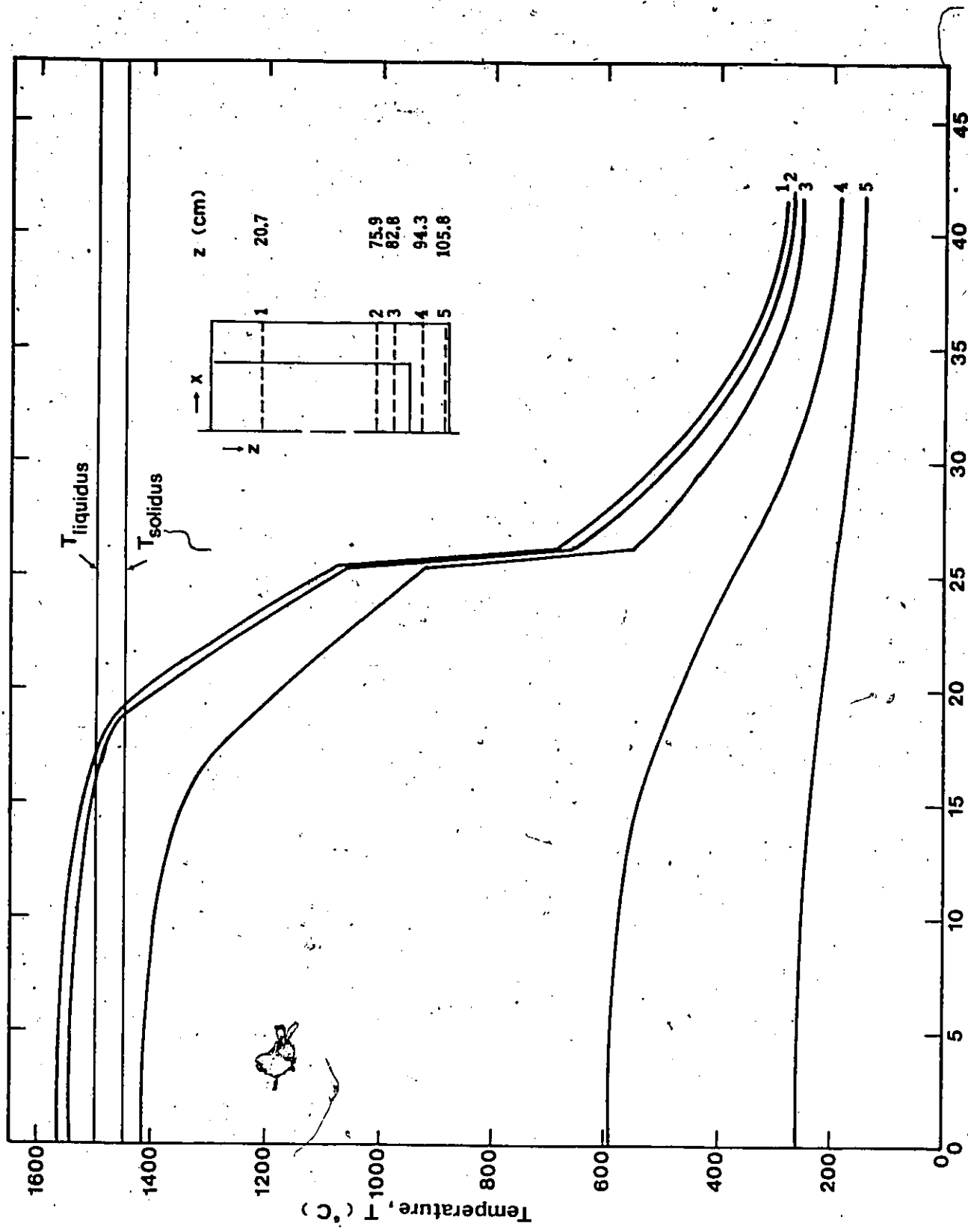

Fig. 4.22. Temperature gradients in the ingot and mold at time = 10.0 min. after pouring.

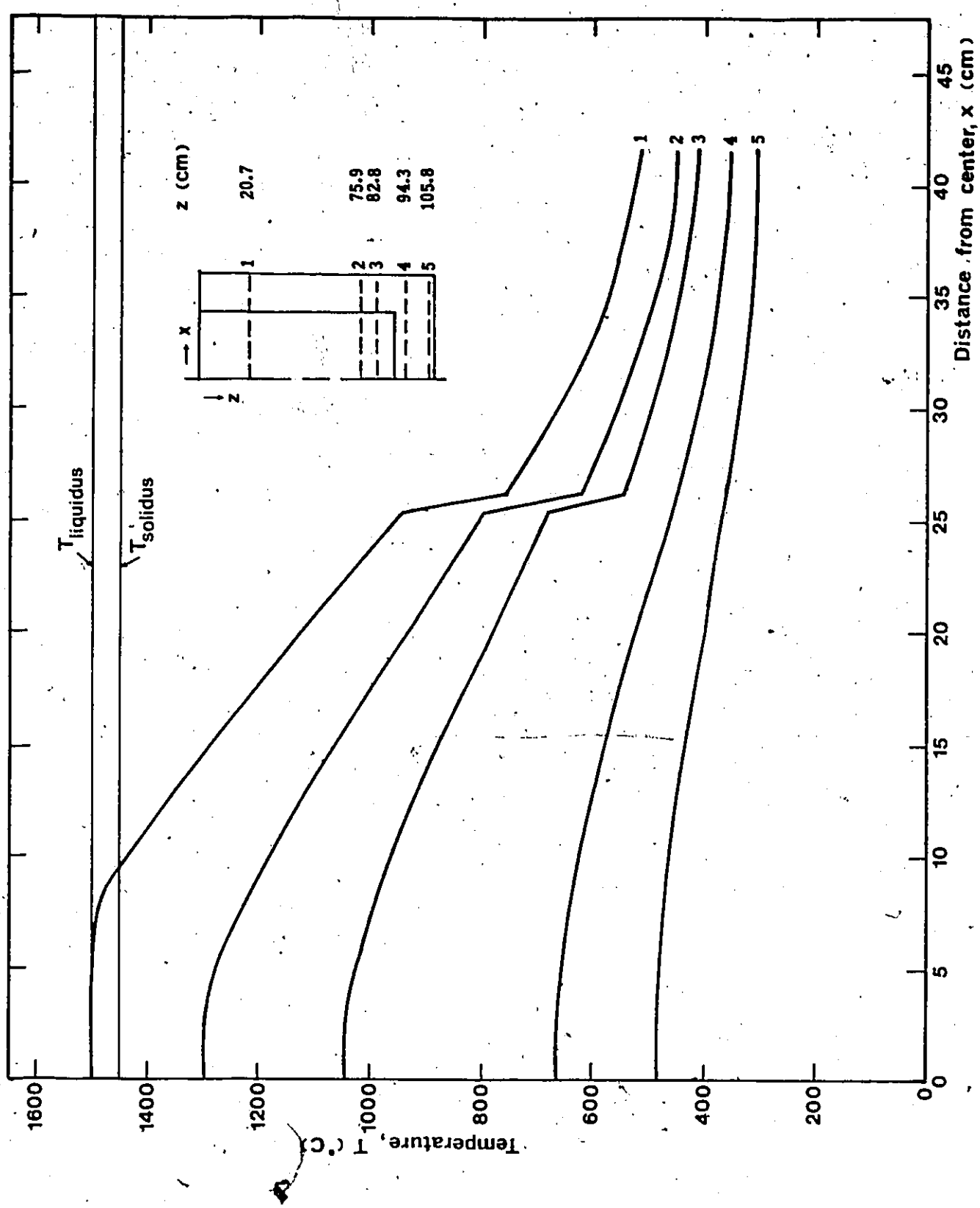

Fig. 4.23. Temperature gradients in the ingot and mold at time = 40.0 min. after pouring.

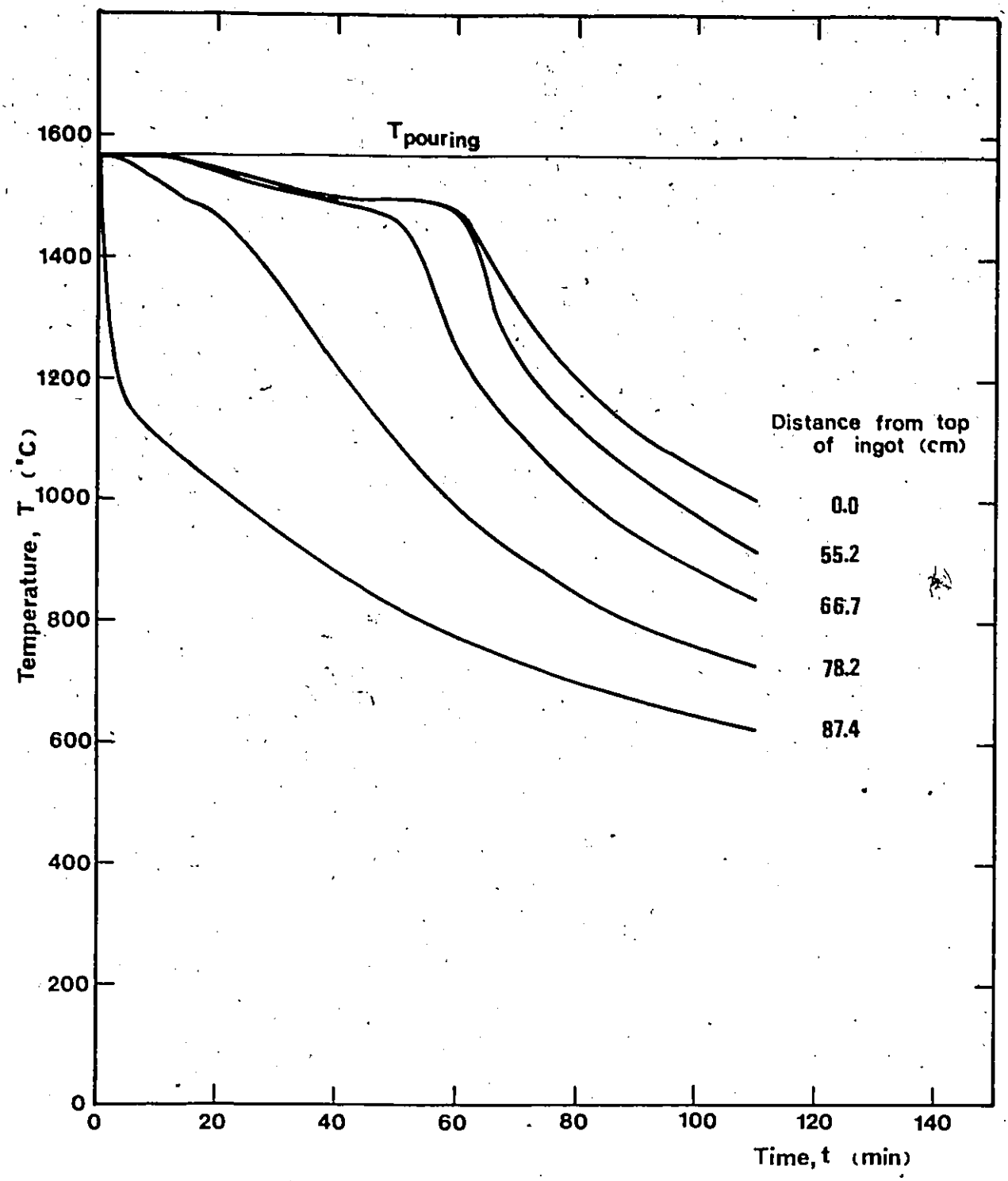

Fig. 4.24. Cooling curves at the center of ingot.

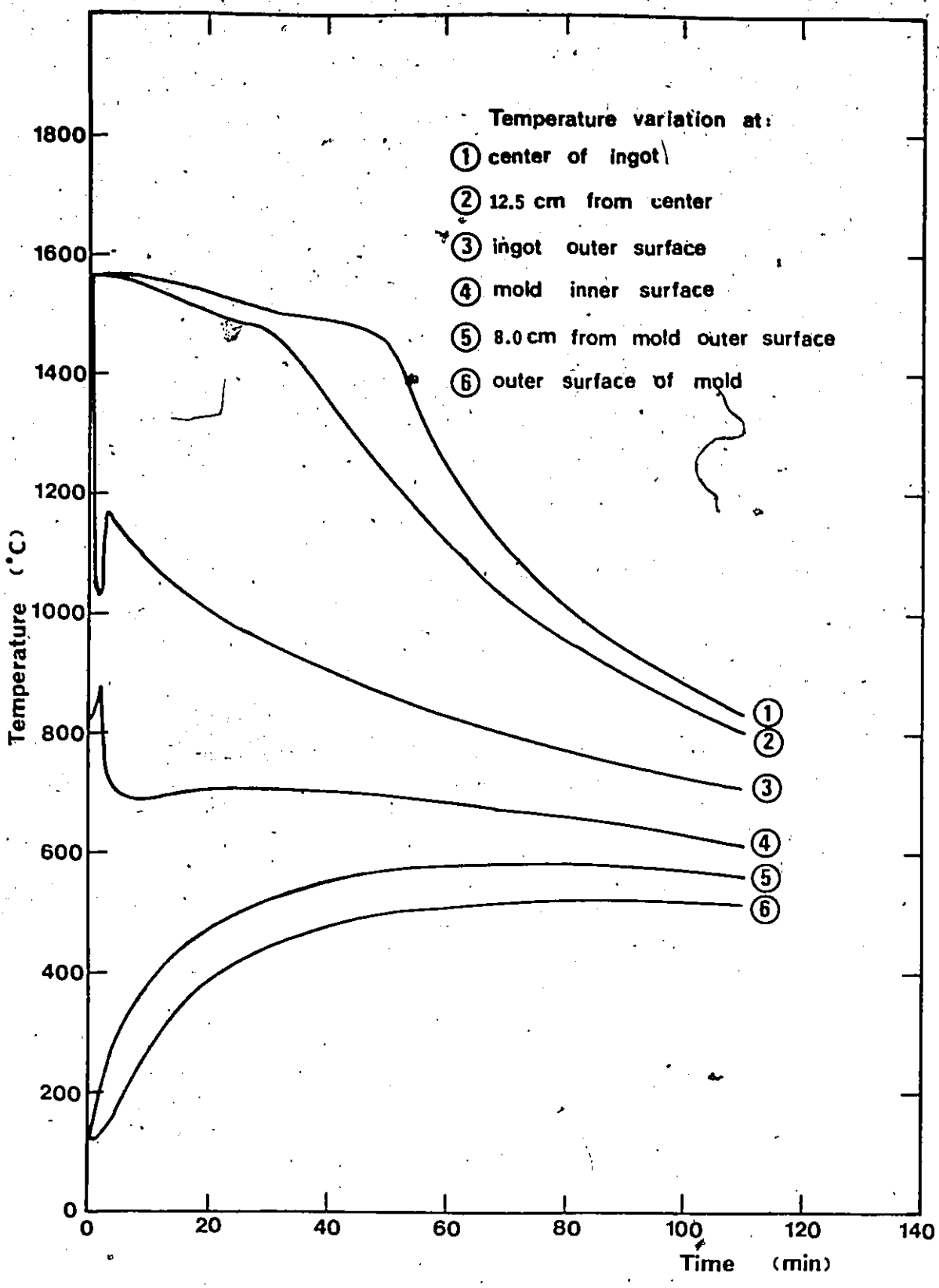

Fig. 4.25. Ingot and mold temperature-time variation at 66.7 cm from top of ingot.

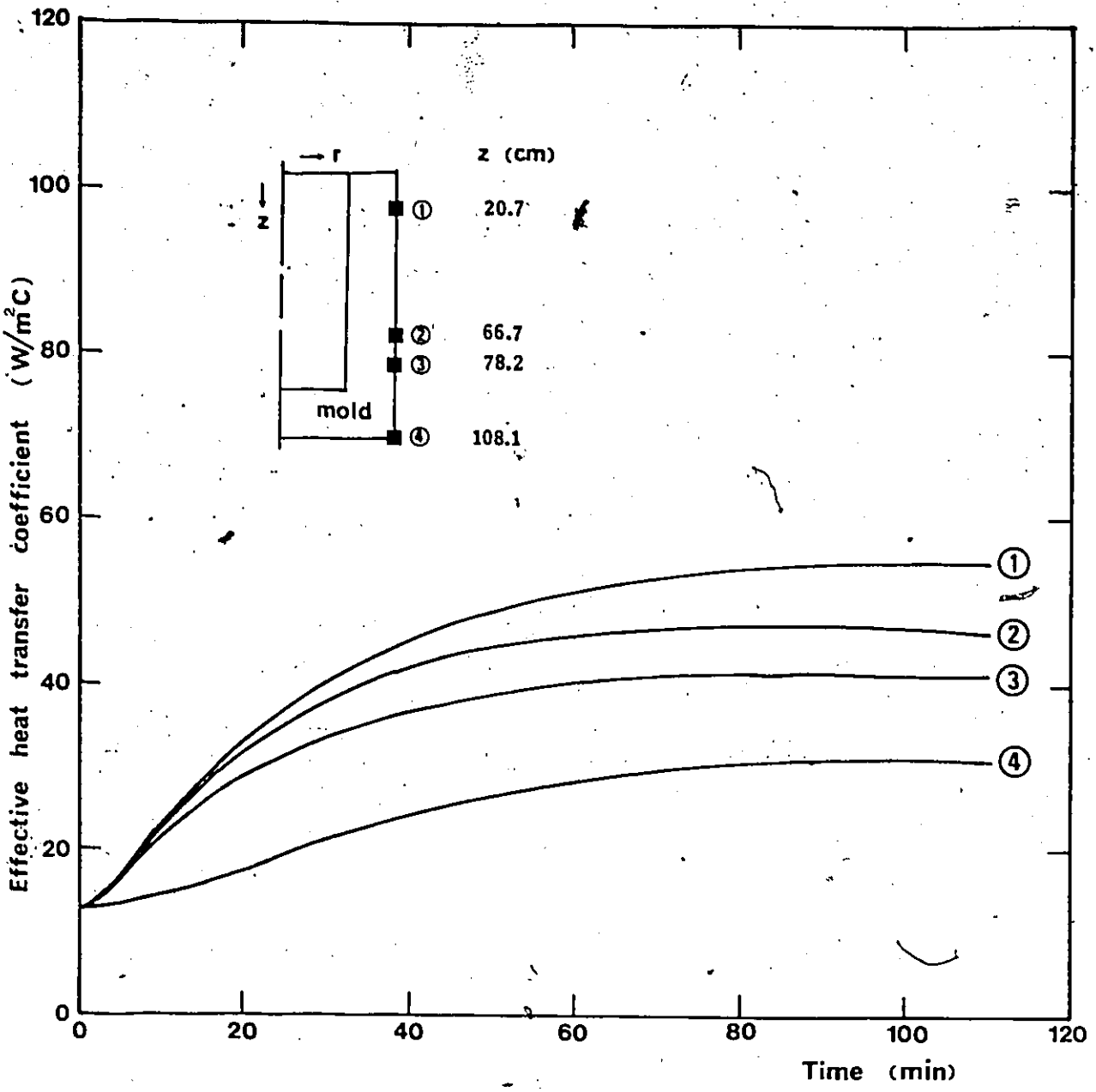

Fig. 4.26. Variation of effective heat transfer coefficient at side outer surface of mold.

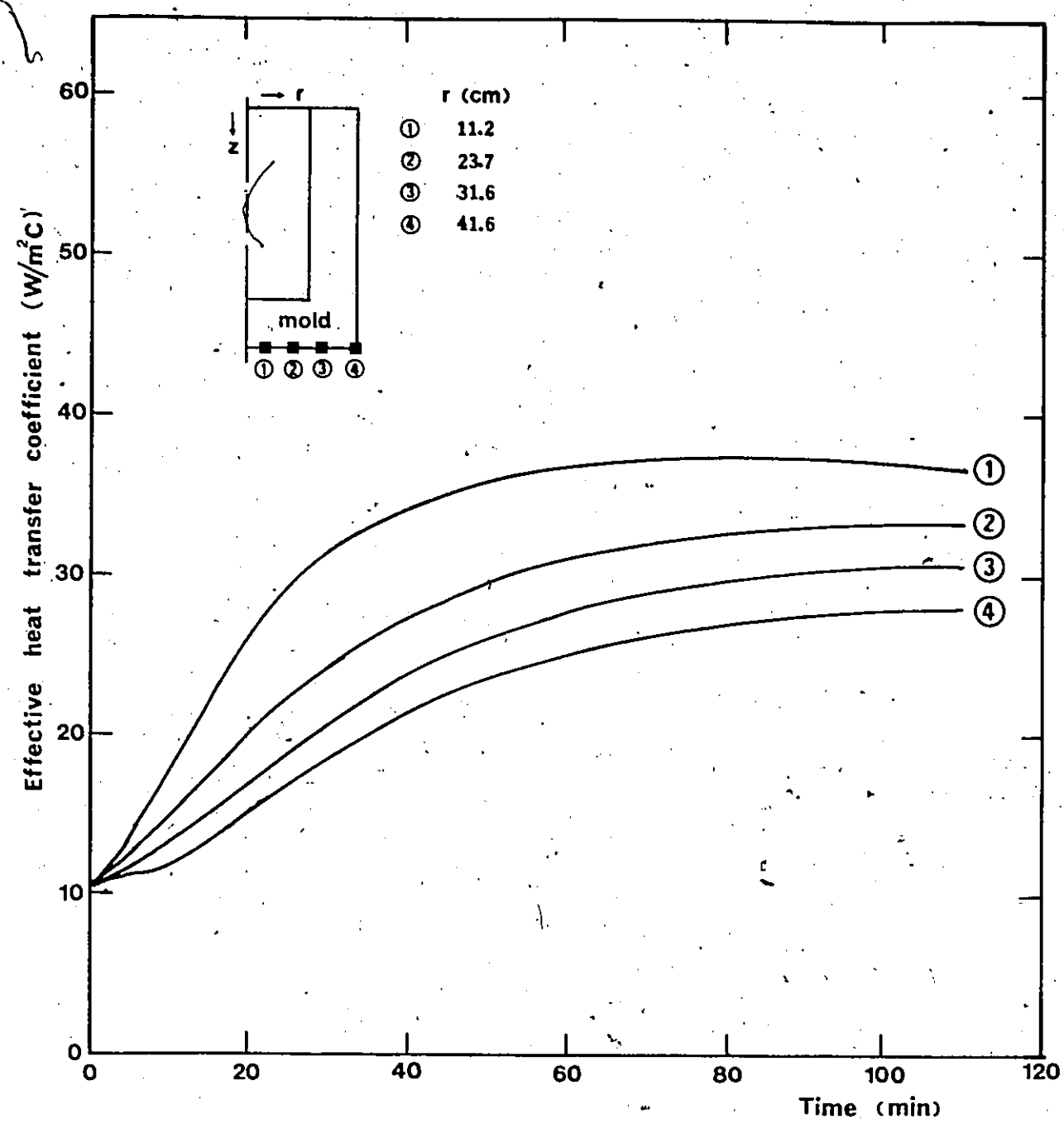

Fig. 4.27. Variation of effective heat transfer coefficient at bottom outer surface of mold.

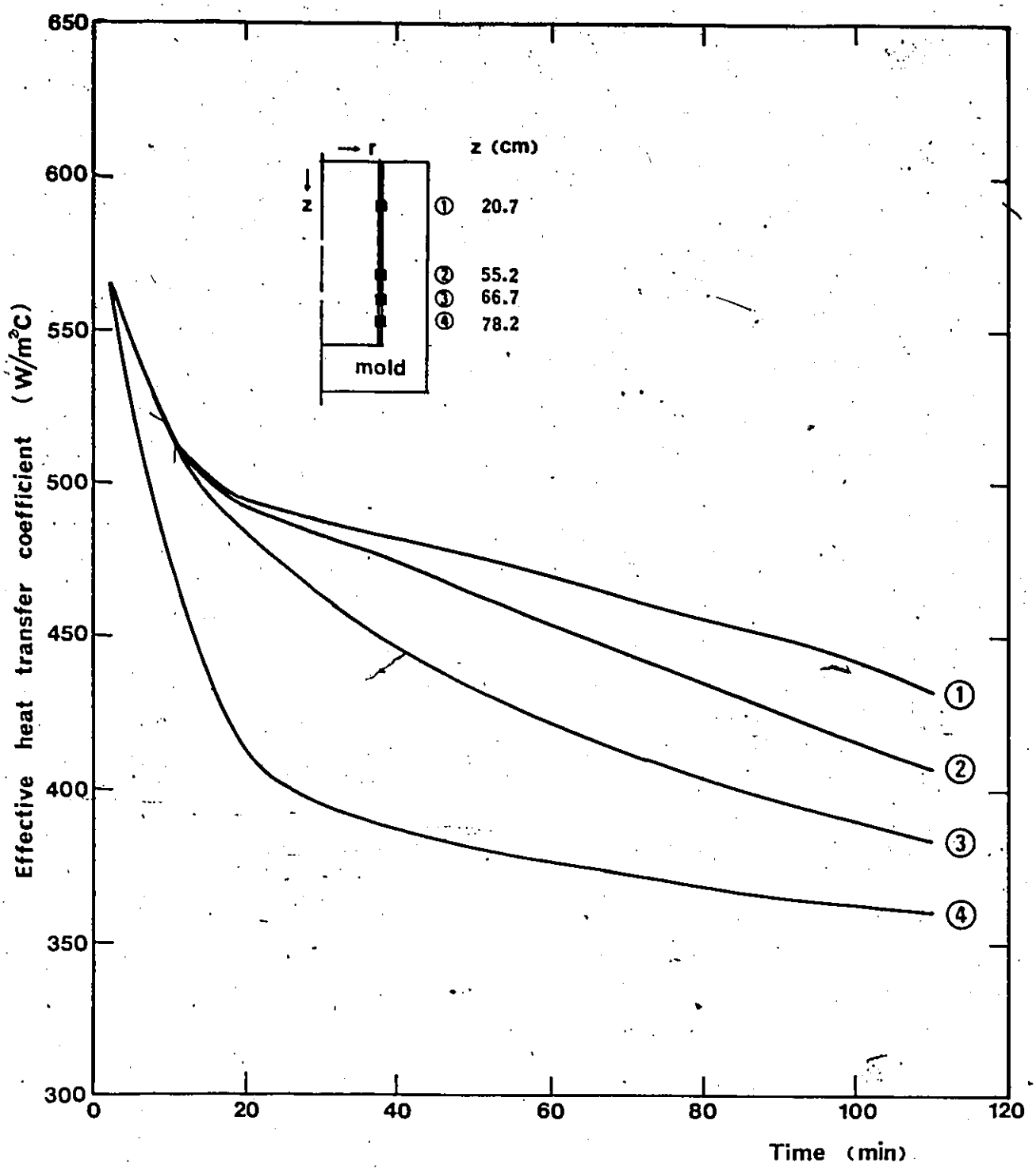

Fig. 4.28. Variation of the interface heat transfer coefficient.

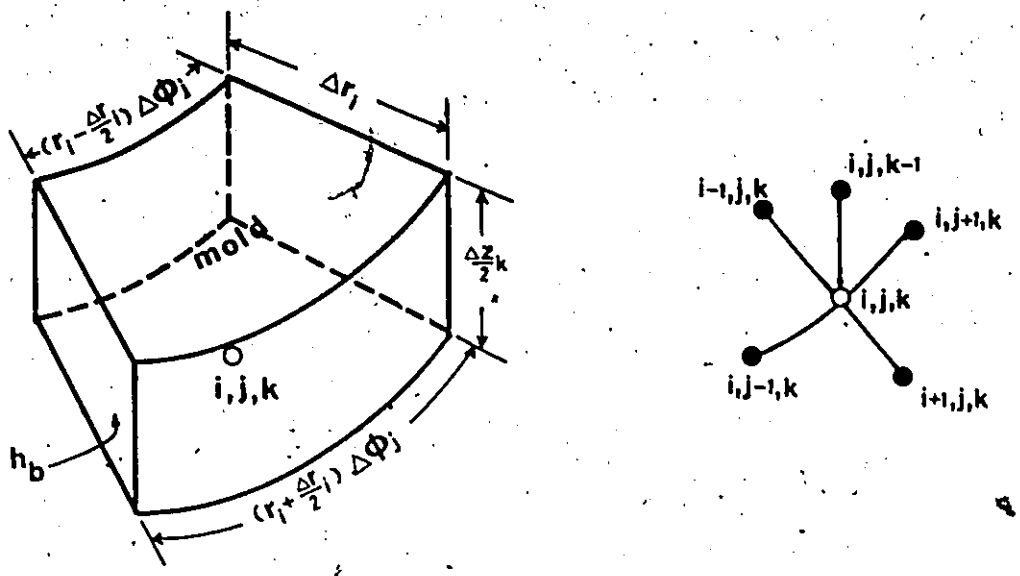

Fig. B.1. Control volume for a node located at the bottom of the mold.

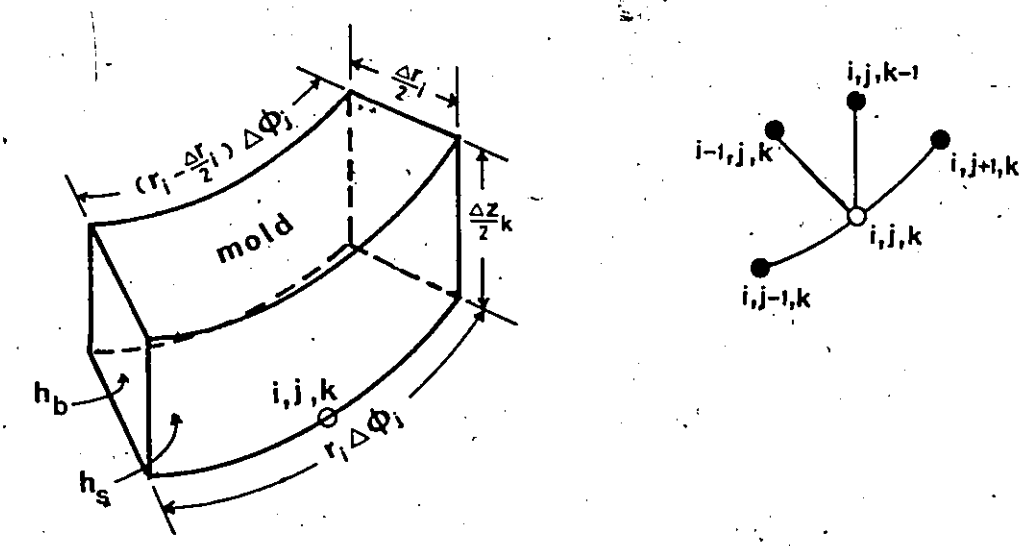

Fig. B.2. Control volume for a corner node located at the bottom of the mold.

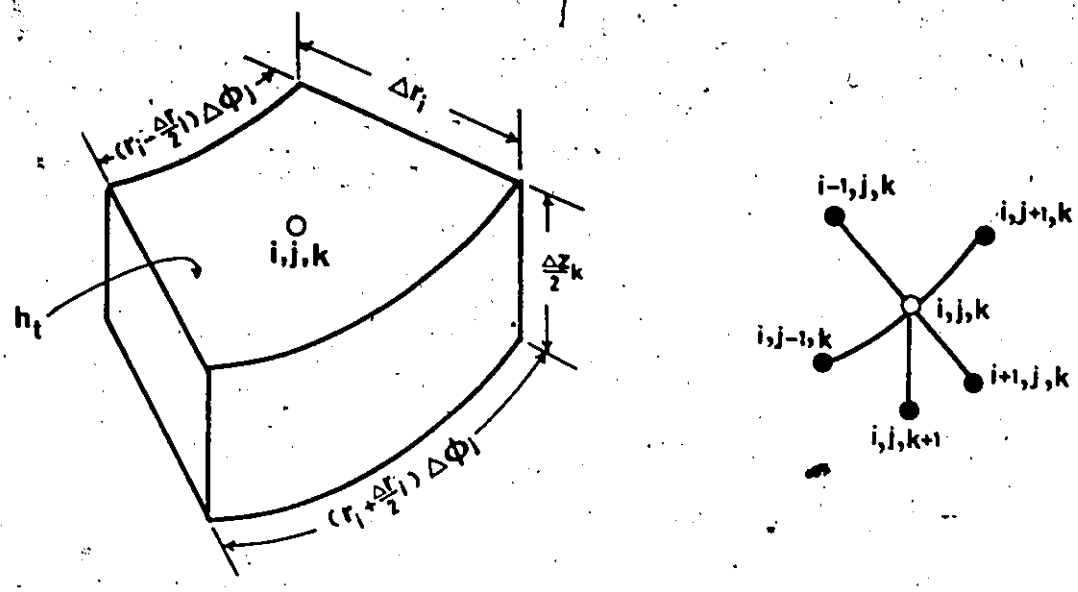

Fig. B.3. Control volume for a node located at the top boundary.

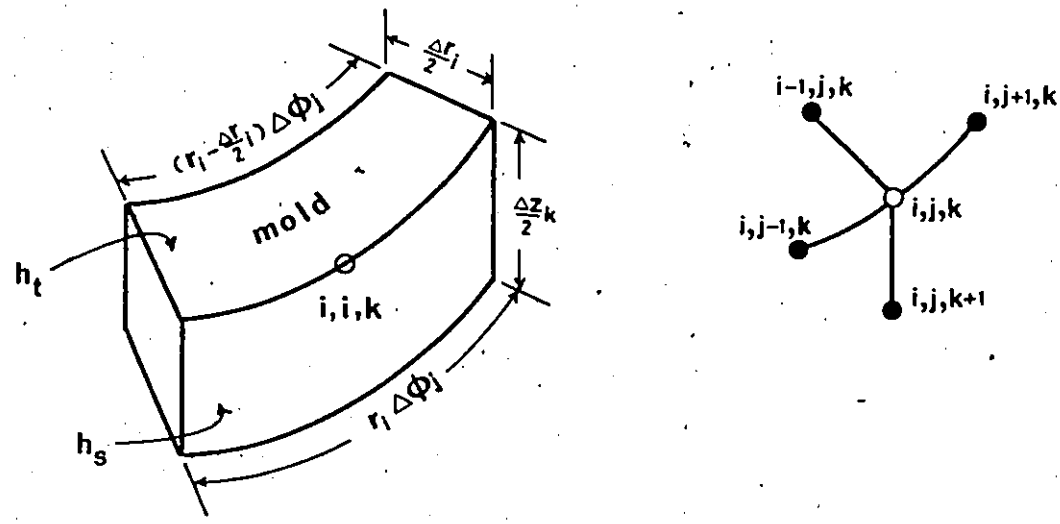

Fig. B.4. Control volume for a corner node located at the top of the mold.

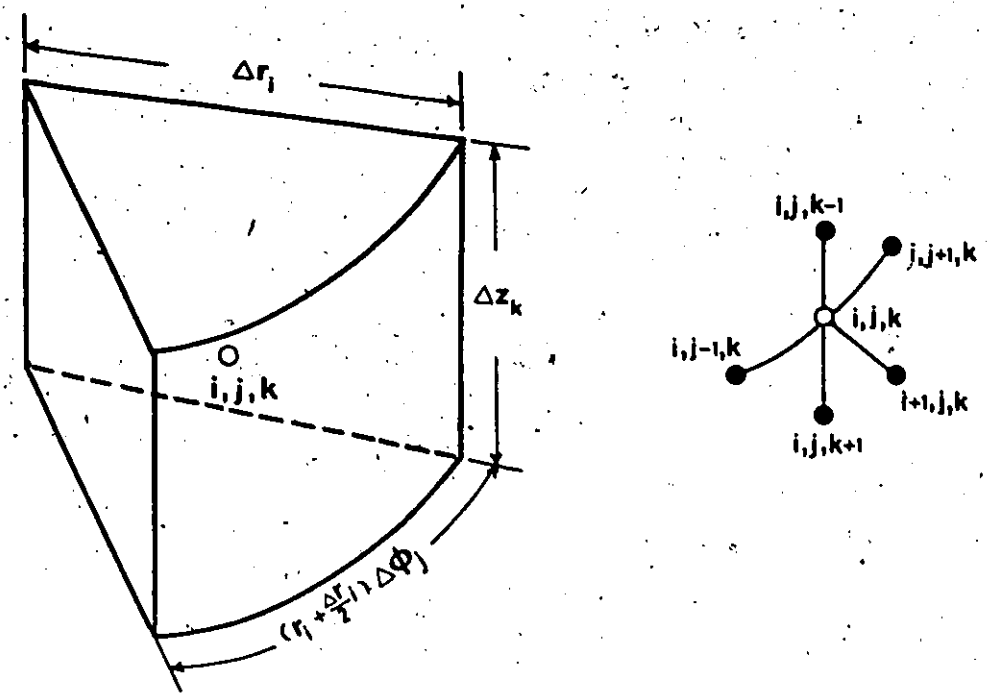

Fig. B.5. Control volume for a centreline node.

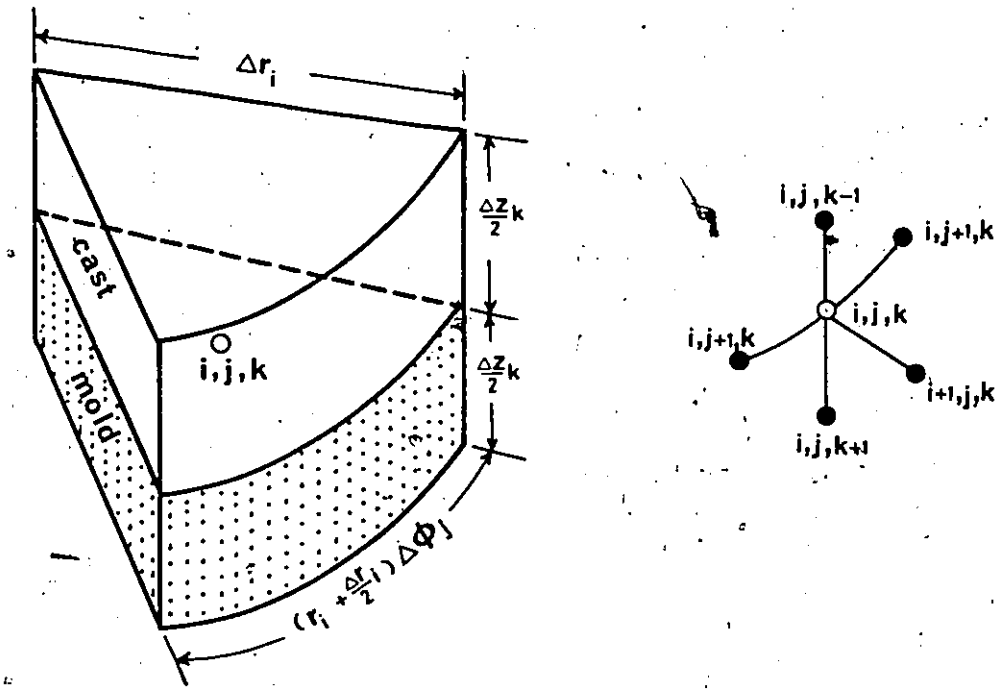

Fig. B.6. Control volume for a centreline node located at the cast/mold interface.

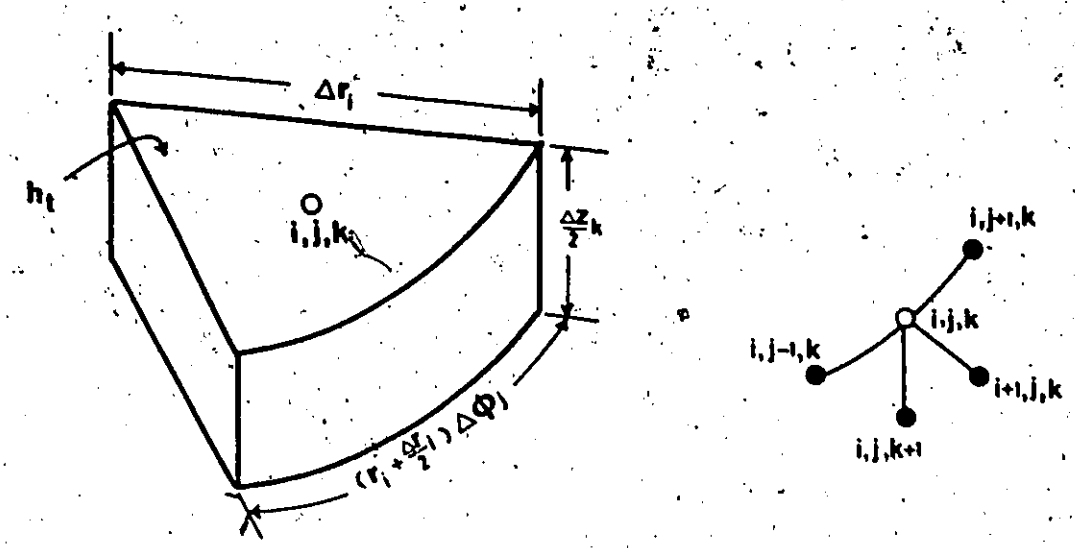

Fig. B.7. Control volume for a centreline node located at the top boundary.

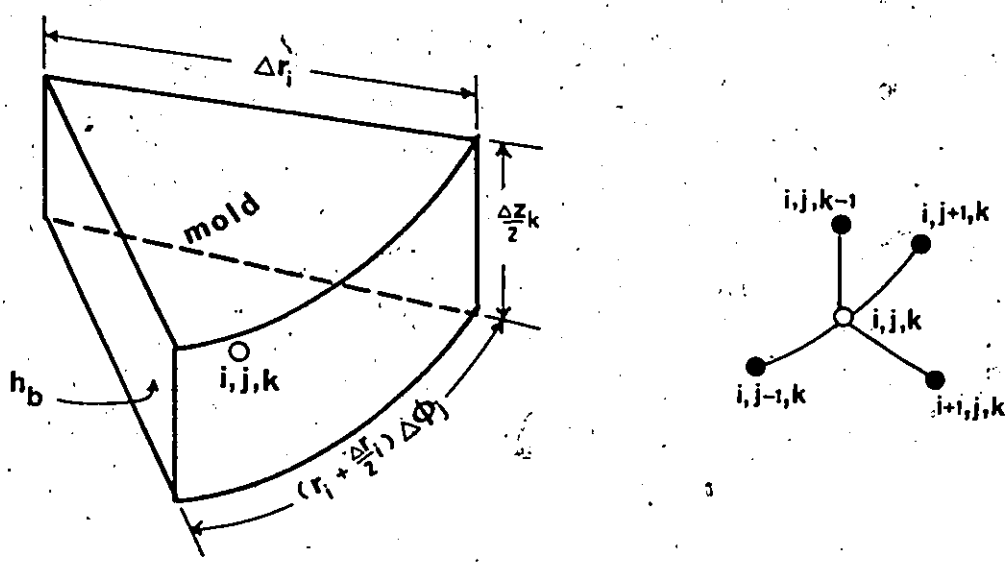

Fig. B.8. Control volume for a centreline node located at the bottom boundary.

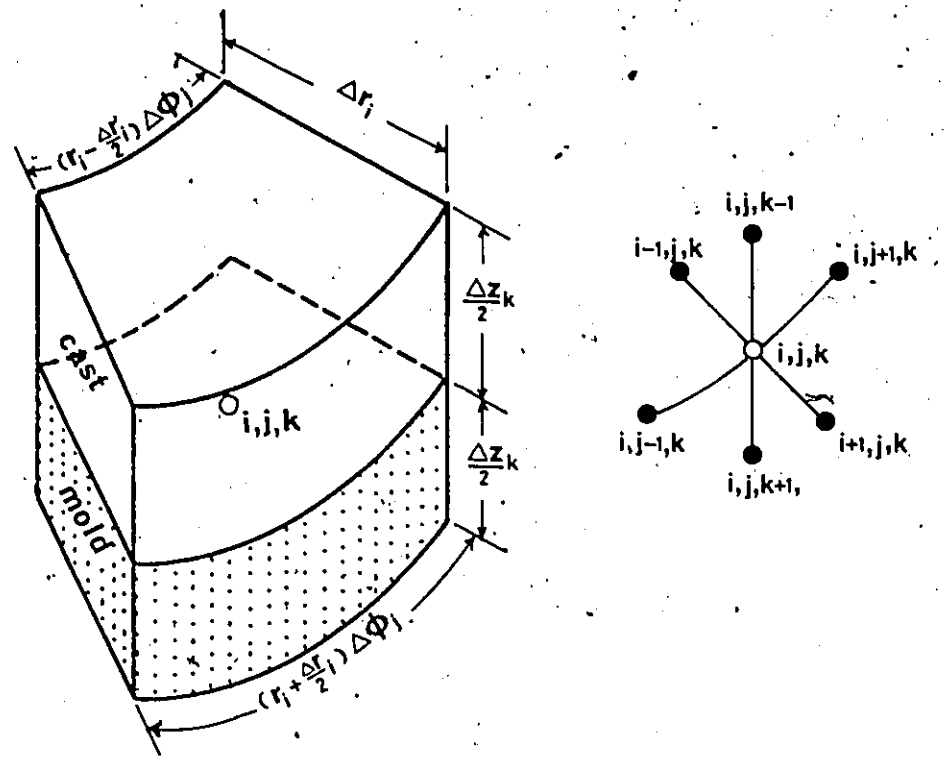

Fig. B.9. Control volume for an interface node located at the bottom of the casting.

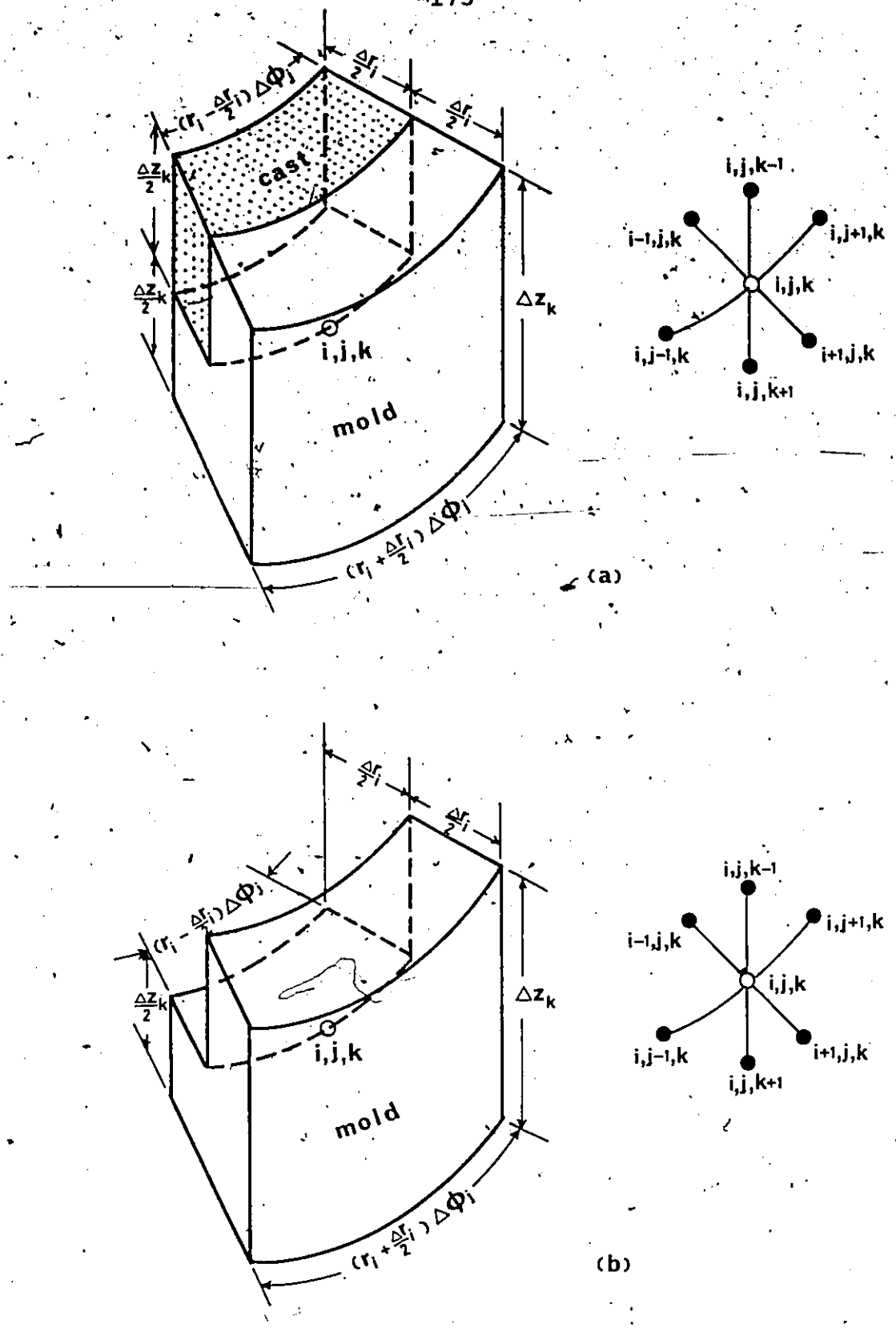

Fig. B.10. Control volume for a corner node located at the interface (a) before and (b) after gap formation.

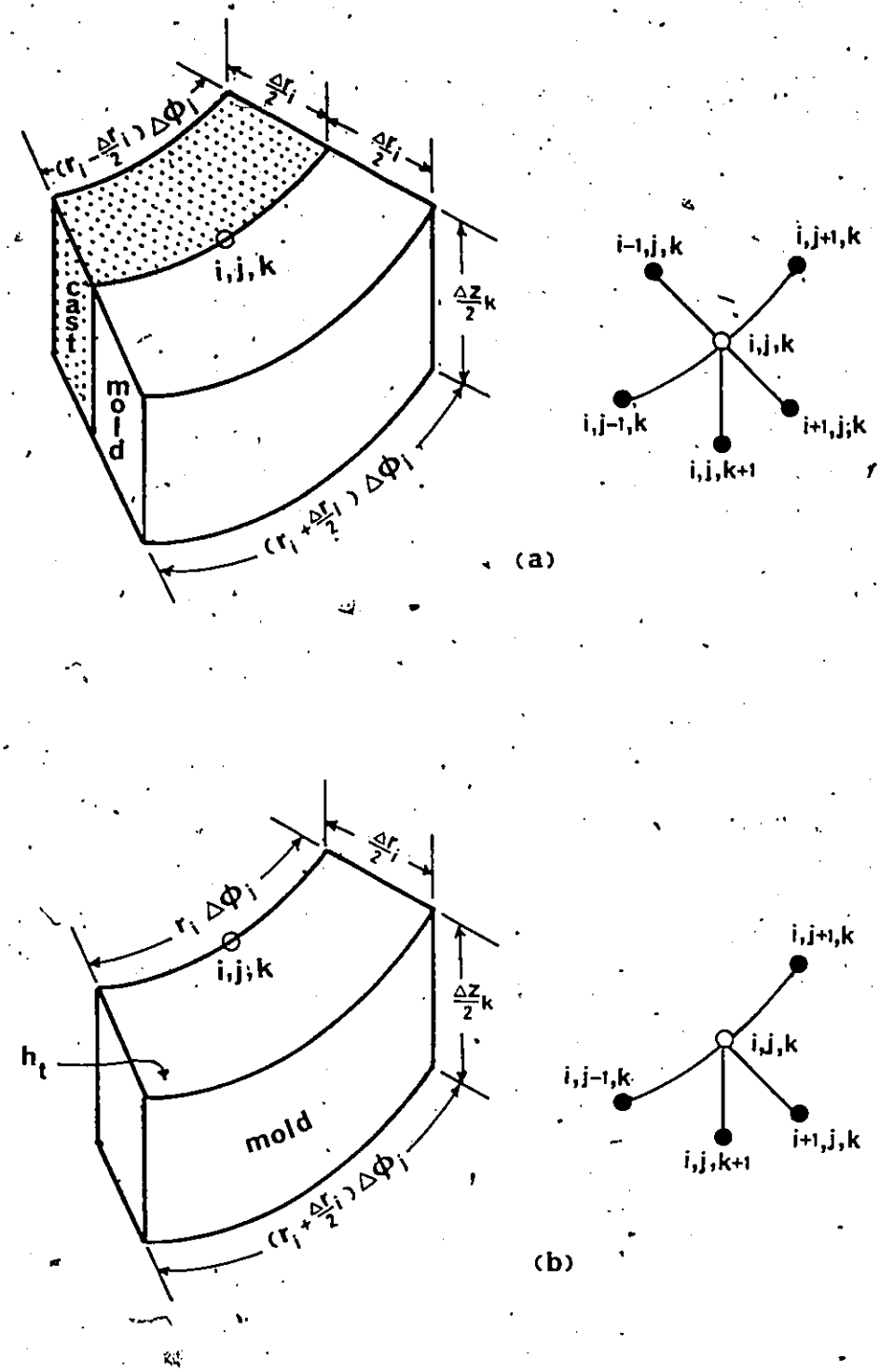

Fig. B.11. Control volume for an interface node located at the top boundary (a) before and (b) after gap formation.

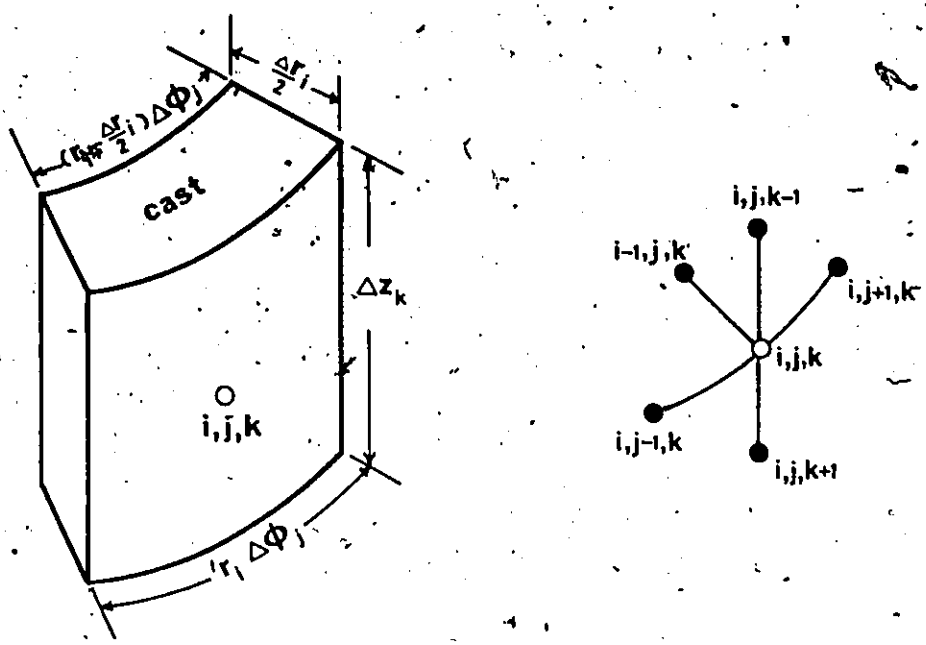

Fig. B.12. Control volume for a node on the outer surface of the cast after the air-gap is formed.

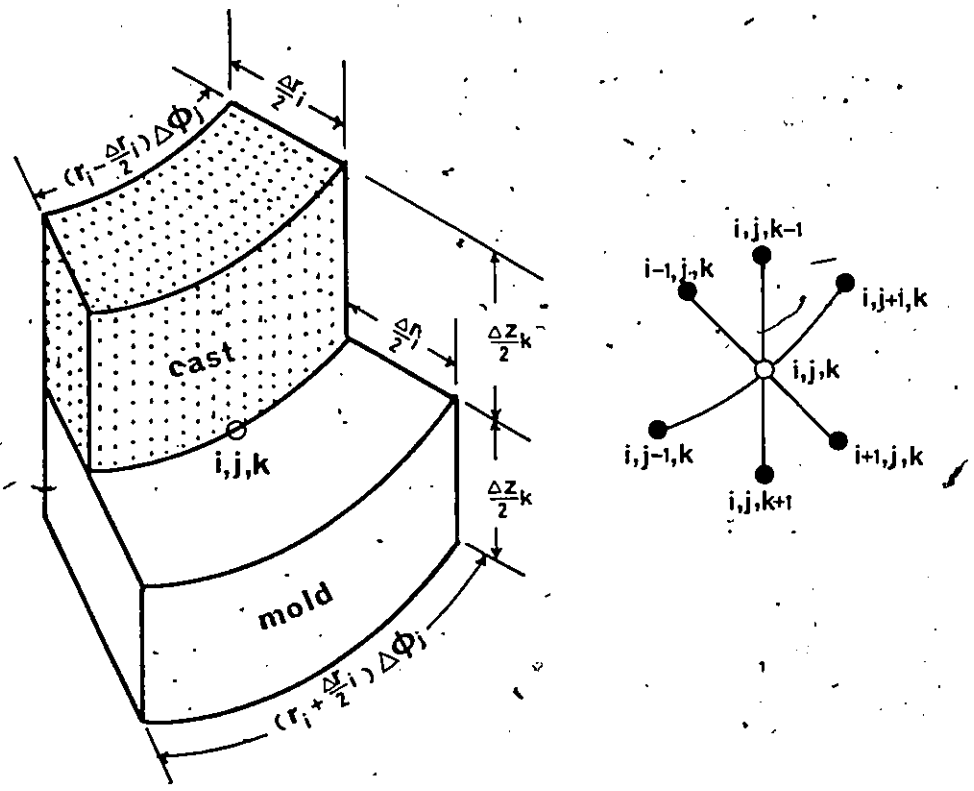

Fig. B.13. Control volume for an interface node located at the corner of the cast (after the air-gap is formed).

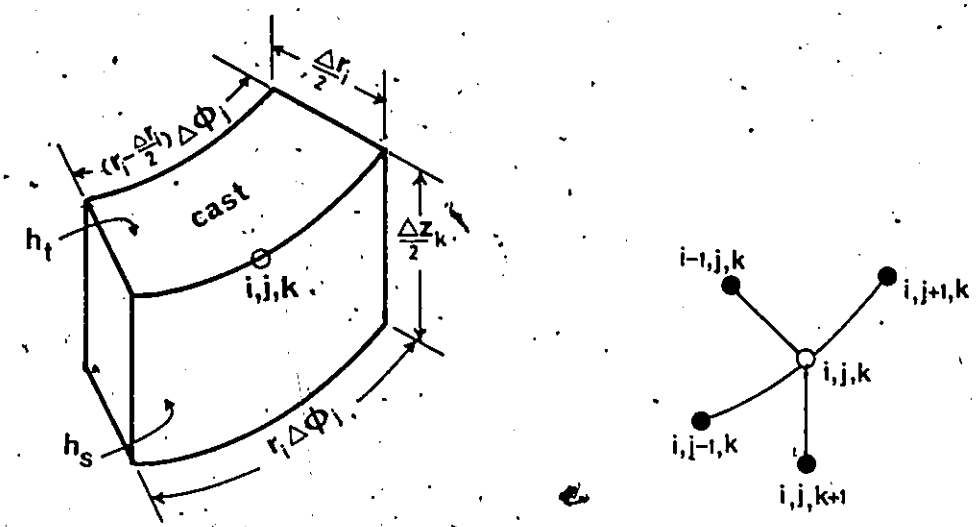

Fig. B.14. Control volume for a node on the outer surface of the cast located at the top boundary (after the air-gap is formed).

BIBLIOGRAPHY

1. Sokolov, N.A. and Kharchenko, V.D., "Improving Cast Steel Quality by Argon Injection", Steel in USSR, pp. 593, Oct. 1977.

2. Welch, J.E., Harlow, F.H., Shannon, J.P. and Daly, B.J., "The MAC Method", Los Alamos Scientific Laboratory Report, LA-3425, 1966.

3. Peaceman, D.W, and Rachford, H.H., "The Numerical Solution of Parabolic and Elliptic Differential Equations", J. Soc. Indust. Appl. Math., Vol. 3, pp. 28, 1955.

4. Roache, P.J., "Computational Fluid Dynamics", Hermosa Publishers, New Mexico, 1972.

5. Amsden, A.A., "The Particle-in-Cell Method for the Calculation of the Dynamics of Compressible Fluids", Los Alamos Scientific Laboratory Report LA-3466, 1966.

6. Amsden, A.A. and Harlow, F.H., "The SMAC Method: A Numerical Technique for Calculating Incompressible Fluid Flows", Los Alamos Scientific Laboratory Report LA-4370, 1970.

7. Rivard, W.C., Butler, T.D., Farmer, O.A. and O'Rourke, P.J., "A Method for Increased Accuracy in Eulerian Fluid Dynamics Calculations", Los Alamos Scientific Laboratory Report LA-5426-MS, 1973.

8. Amsden, A.A. and Hirt, C.W., "YAQUI: An Arbitrary Lagrangian-Eulerian Computer Program for Fluid Flow at All Speeds", Los Alamos Scientific Laboratory Report LA-5100, 1973.

9. Rivard, W.C., Farmer, O.A. and Butler, T.D., "RICE: A Computer Program for Multicomponent Chemically Reactive Flows at All Speeds", Los Alamos Scientific Laboratory Report LA-5812, 1974.

10. Amsden, A.A. and Harlow, F.H., "KACHINA: An Eulerian Computer Program for Multifield Fluid Flows", Los Alamos Scientific Laboratory Report LA-5680, 1974.

11. Hirt, C.W., Nichols, B.D. and Romero, N.C., "SOLA - A Numerical Solution Algorithm for Transient Fluid Flows", Los Alamos Scientific Laboratory Report LA-5852, 1975.

12. Harlow, F.H. and Welch, J.E., "Numerical Calculation of Time-Dependent Viscous Incompressible Flow of Fluid with Free Surface", Phys. Fluids, Vol. 8, No. 12, pp. 2182, 1965.

13. Viecelli, J.A., "A Method for Including Arbitrary External Boundaries in the MAC Incompressible Fluid Computing Technique", J. of Comp. Phys., Vol. 4, pp. 543, 1969.

14. Chan, R.K.C. and Street, R.L., "A Computer Study of Finite-Amplitude Water Waves", J. of Comp. Phys., Vol. 6, pp. 68, 1970.

15. Viecelli, J.A., "A Computing Method for Incompressible Flow Bounded by Moving Walls", J. of Comp. Phys., Vol. 8, pp. 119, 1971.

16. Harlow, F.H. and Amsden, A.A., "A Numerical Fluid Dynamics Calculation Method for All Flow Speeds", J. of Comp. Phys., Vol. 8, pp. 197, 1971.

17. Nichols, B.D. and Hirt, C.W., "Improved Free Surface Boundary Conditions for Numerical Incompressible Flow Calculations", J. of Comp. Phys., Vol. 8, pp. 434, 1971.

18. Hirt, C.W. and Cook, J.L., "Calculating Three-Dimensional Flows Around Structures and Over Rough Terrain", J. of Comp. Phys., Vol. 10, pp. 324, 1972.

19. Gosman, A.D., Pun, W.M., Runchal, A.K., Spalding, D.B. and Wolfshtein, M., "Heat and Mass Transfer in Recirculating Flows", Academic Press, New York, 1969.

20. Patankar, S.V. and Spalding, D.B., "A Calculation Procedure for Heat, Mass and Momentum Transfer in Three-Dimensional Parabolic Flows", Int. J. Heat and Mass Transfer, Vol. 15, pp. 1787, 1972.

21. Scaninject, Proc. Int. Conf. Injection Metallurgy, MEFOS, Lulea, Sweden, June 1977.

22. McMaster Symposium on Ladle Treatment of Carbon Steel, Hamilton, Canada, May 1979.

23. Szekely, J., Wang, H.J. and Kiser, K.M., "Flow Pattern Velocity and Turbulence Energy Measurements and Prediction in a Water Model of an Argon-Stirred Ladle", Met. Trans. B., Vol. 7B, pp. 287, June 1976.

24. Szekely, J., Dilawari, A.H. and Metz, R., Met. Trans. B., Vol. 10B, pp. 33, 1979.

25. Szekely, J., Lehner, T. and Chang, C.W., "Flow Phenomena, Mixing, and Mass Transfer in Argon-Stirred Ladles", Ironmaking and Steelmaking, No. 6, pp. 285, 1979.

26. El-Kaddah, N.H. and Szekely, J., "Mathematical Model for Desulphurization Kinetics in Argon-Stirred Ladles", Ironmaking and Steelmaking, No. 6, pp. 269, 1981.

27. Jones, W.P. and Launder, B.E., "The Prediction of Laminarization with Two-equation Model of Turbulence", Int. J. Heat and Mass Transfer, Vol. 15, pp. 301, 1972.

28. Chiang, H.T., Lehner, T. and Bjorn, K., "Fluid Flow in Ladles - Experimental Results", Scand. J. Metallurgy, 9, pp. 105, 1980.

29. Deb Roy, T., Majmudar, A.K. and Spalding, D.B., "Numerical Prediction of Recirculation Flows with Free Convection Encountered in Gas-agitated Reactors", Appl. Math. Modelling, Vol. 2, pp. 146, 1978.

30. Deb Roy, T. and Majumdar, A.K., "Predicting Fluid Flow in Gas-Stirred Systems", J. of Metals, pp. 42, 1981.

31. Szekely, J., El-Kaddah, N.H. and Grevet, J.H., "Flow Phenomena in Argon Stirred Ladles. Room Temperature Measurements and Analysis", Scaninject II Conference Preprint, Lulea, Sweden, pp. 5:1-32, 1980.

32. Pun, W.M. and Spalding, D.B., Rep. HTS 76/2 Heat Transfer Section, Imperial College, London, 1977.

33. Sahai, Y. and Guthrie, R.I.L., "Effective Viscosity Models for Gas-Stirred Ladles", Met. Trans. B., Vol. 13B, No. 1, 1982.

34. Lightfoot, N.M.H., J. Iron Steel Inst., Vol. 119, pp. 364, 1929.

35. Lightfoot, N.M.H., J. Iron Steel Inst., Vol. 2, pp. 162, 1932.

36. Adams, C.M., Proc. Seminar, Liquid Metals and Solidification, 39th National Metal Congress (America Society of Metals, Chicago), 1957.

37. Garcia, A. and Prates, M., "Mathematical Model for the Unidirectional Solidification of Metals: I. Cooled Molds", Met. Trans. B., Vol. 9B, pp. 449, 1978.

38. Garcia, A. and Prates, M., "Mathematical Model for the Unidirectional Solidification of Metals: II. Massive Molds", Met. Trans. B., Vol. 10B, pp. 85, 1979.

39. Paschkis, V., "Studies on Solidification of Castings - Heat Transfer Committee Report", Trans. American Foundrymen's Assoc., Vol. 53, pp. 90, 1945.

40. Paschkis, V., "Studies on the Solidification of Aluminum Castings", Trans. American Foundrymen's Society, Vol. 56, pp. 366, 1948.

41. Paschkis, V. and Rydar, F.L., Direct Analog Computers, John Wiley & Sons, New York, 1968.

42. Sarjant, R.J. and Slack, M.R., "Internal Temperature Distribution in the Cooling and Reheating of Steel Ingots", J. of Iron and Steel Inst., Vol. 177, pp. 428, 1954.

43. Dusinberre, G.M., Heat Transfer Calculations by Finite Differences, Int. Text Book Co., 1961.

44. Nishida, Y., Imai, T. and Matsubara, H., "Numerical Analysis of Solidification of Cast Iron in Metal Moulds", Trans. Iron Steel Inst. Japan, No. 13, pp. 304, 1977.

45. Srinivasan, M.N., "Analytical Studies on the Solidification of Hypereutectic Cast Iron in Metallic Molds", AFS Cast Metals Research Journal, pp. 91, 1975.

46. Lazaridis, Day and Zimmermann, "A Computer-Aided Solution of the Solidification Problem", AFS Cast Metal Research Journal, pp. 48, 1974.

47. Thamban, M.I. and Panchanathan, V., "Numerical Simulation of Solidification of Aluminum Alloys in Cast Iron Molds", AFS Transactions, pp. 167, 1980.

48. Marrone, R.E., Wilkes, J.O. and Pehlke, R.D., "Numerical Simulation, Part I: Low Carbon Steel Casting - T Shape", Cast Metals Research Journal, pp. 184, 1970.

49. Marrone, R.E., Wilkes, J.O. and Pehlke, R.D., "Numerical Simulation of Solidification, Part II: Low Carbon Steel Casting - L Shape", Cast Metals Research Journal, pp. 188, 1970.

50. Pehlke, R.D., Kirt, M.J., Marrone, R.E. and Cook, D.J., "Numerical Simulation of Casting Solidification", Cast Metals Research Journal, Vol. 9, pp. 49, 1973.

51. Raychaudhuri, B.C., Chatterjee, G., Yadav, K.G. and Majumder, J., "Thermal Aspect of Steel Ingot Solidification and Numerical Investigation of a Two-Dimensional Heat Flow Problem", Indian J. of Technology, Vol. 15, pp. 185, 1977.

52. Den Hartog, H.W., Rabenberg, J.M. and Willemse, J., "Application of a Mathematical Model in the Study of Ingot Solidification Process", Ironmaking and Steelmaking, No. 2, pp. 134, 1975.

53. Lazaridis, A., "A Numerical Solution of the Multidimensional Solidification (or Melting) Problem", Int. J. Heat Mass Transfer, Vol. 13, pp. 1459, 1970.

54. Spencer, S., Carless, P. and Magee, E., "Mathematical Model for Simulation of Solidification and Cooling of Cast Rolls", Ironmaking and Steelmaking, No. 3, 1981.

55. Szekely, J. and Jassal, A.S., "An Experimental and Analytical Study of the Solidification of a Binary Dendritic System", Met. Trans. B., Vol. 9B, pp. 389, 1978.

56. Ballantyne, A.S. and Mitchell, A., "Modelling of Ingot Thermal Fields in Consumable Electrode Remelting Processes", Ironmaking and Steelmaking, No. 4, pp. 222, 1977.

57. Brody, H.D. and Stoehr, R.A., "Computer Simulation of Heat Flow in Casting", J. of Metals, pp. 20, Sept. 1980.

58. Peel, D.A. and Pengelly, A.E., Mathematical Models in Metallurgical Process Development, pp. 186, The Iron and Steel Institute, London, 1970.

59. Heuser, J., "Finite Element Method for Thermal Analysis", NASA TND-7274, Nov. 1973.

60. Morgan, K., "A Numerical Analysis of Freezing and Melting with Convection", Computer Methods in Appl. Mechanics and Engineering, No. 28, pp. 275, 1981.

61. Wilson, E. and Nickell, R.E., "Application of the Finite Element Method to Heat Conduction Analysis", Nuclear Eng. and Design, Vol. 4, No. 3, pp. 276, 1966.

62. Weckman, D.C., Pick, R.J. and Niessen, P., "A Numerical Heat Transfer Model of the D.C. Continuous Casting Process", Z. Metallkele, No. 70, pp. 750, 1979.

63. Kushner, A.S. and Walston, W.H. Jr., "Conduction and Natural Convection Heat Transfer in a Phase Change Region", Comp. Techniques for Interface Problems, presented at the Winter Annual Meeting of ASME, San Francisco, Dec. 1978.

64. Wallis, G.B., One-Dimensional Two Phase Flow, McGraw-Hill, Chpt. 2, 1969.

65. Davenport, W.G., Richardson, F.D. and Bradshaw, A.V., J. Iron Steel Inst., pp. 1034, 1967.

66. Salcudean, M., Low, C.H., Hurda, A. and Guthrie, R.I.L., "Three-Dimensional Analysis of Recirculatory Flows in Gas-Agitated Reactors", IMACS Conference, Montreal, 1982.

67. Salcudean, M., Low, C.H., Hurda, A. and Guthrie, R.I.L., "Computation of Three-Dimensional Flow and Heat Transfer in Gas-Agitated Reactors", Chem. Eng. Communications, (in press), 1982.

68. Guthrie, R.I.L. and Sahai, Y., (Unpublished research), McGill University, Montreal, 1980.

69. Wong, R.C.L., M.A.Sc. thesis, Dept. of Mechanical Eng., U. of Ottawa, Ottawa, 1982.

70. Salcudean, M. and Guthrie, R.I.L., "Fluid Flow in Filling Ladles", Met. Trans. B, Vol. 9B, pp. 181, 1978.

71. Salcudean, M. and Guthrie, R.I.L., "Turbulent Flow in Filling Ladles", Met. Trans. B, Vol. 9B, pp. 673, 1978.

72. Tanaka, M., Ph.D. thesis, Dept. of Mining and Metallurgical Eng., McGill University, Montreal, 1979.

73. Patankar, S.V., Numerical Heat Transfer and Fluid Flow, McGraw-Hill Book Co., 1980.

74. Campagna, A., Sc.D. thesis, Dept. of Metallurgy and Material Science, M.I.T., Cambridge, Mass., 1970.

75. Flemings, M.C., Solidification Processing, McGraw-Hill, pp. 19, 1974.